2011

Numerical methods for the study of super-Eddington mass transfer in double white dwarf binaries

Dominic Carlo Marcello
Louisiana State University and Agricultural and Mechanical College, dmarcello4@gmail.com

NUMERICAL METHODS FOR THE STUDY OF SUPER-EDDINGTON MASS TRANSFER IN DOUBLE WHITE DWARF BINARIES

Submitted to the Graduate Faculty of the
Louisiana State University and
Agricultural and Mechanical College
in partial fulfillment of the
requirements for the degree of
Doctor of Philosophy

in

The Department of Physics and Astronomy

by
Dominic Carlo Marcello
B.S., Louisiana State University and Agricultural and Mechanical College, 2000
December, 2011

Dedication

This work is dedicated to my loving wife, Sarah.

Acknowledgements

First and foremost I would like to thank my major professor, Joel Tohline. Soon after I entered graduate school, I found myself in Joel's office looking at colored blobs floating over flat screen televisions. I pretended to understand what Joel was telling me about the blobs, and not long after that he hired me as his graduate assistant. Under Joel's guidance I have not only learned to understand those blobs, but have had the freedom and ability to study much more than what is presented in these pages. I will be ever grateful for the time spent as his student. I would also like to thank Joel for giving me the opportunity, on several occasions, to travel and meet other researchers at various conferences and workshops from Stanford to Princeton and points in between.

I thank Joel's research partner and my second advisor, Juhan Frank, for the immense amount of time he has spent studying and critiquing my research, and, perhaps more importantly, for all the questions he has asked me that I did not know the answer to.

In addition to Joel and Juhan, the members of my dissertation advisory committee were Robert Hynes, Hwang Lee, and Dorel Moldovan. Clive Woods sat on my general examination committee. I appreciate the time these gentlemen took away from their own research to examine mine.

I thank Shangli Ou and Patrick Motl. Joel's post-doctoral researchers at the time, Shangli and Patrick advised me for my first and second summer research projects. Patrick taught me everything he knew about numerical hydrodynamics before he left LSU, and he has continued to provide advice since then. His FLOW-ER code formed the basis for the first versions of the code presented in this dissertation.

I thank fellow graduate students Wes Even, Jay Call, and Zach Byerly, for the many things we have taught one another about astrophysics and high performance computing, and Vayujeet Gokhale, who taught me how to use the telescopes in the Landolt Observatory.

I thank Howard Cohl, a former student of Joel. Late one night in Oakland, California, Howie explained his own dissertation to me and recommended I seek out Joel as an advisor.

I thank our graduate student secretary, Arnell Dangerfield, for all her hard work.

I thank Andrea Edwards and Austin Ograh, for the recent opportunity to teach undergraduate students at Xavier University of Louisiana.

I thank Norbert Zacharias, Ted Rafferty, Sean Urban, and Trudy Tillman of the United States Naval Observatory, for the many sleepless star filled nights I spent as an observer for the USNO CCD Astrograph Catalog (UCAC) at USNO Flagstaff Station.

I thank all of the many wonderful educators I have had over the years. Without diminishing the efforts of others, I would in particular like to thank my middle school teacher, Linda Meyers, my middle school coach, Steve Laquor, and my high school physics teacher, George Bourke.

This work would not have been possible without the love and support of my wife, Sarah, parents, Gail and Vic, step-parents, Alfredo and Stephanie, siblings, Kate, Tom, and Liz, wife's family, Laura, Buddy, Michael, and Tommy, and my Aunt Kathy.

It is an exceptional privilege to be paid to think about astrophysics, and it would not be possible without the taxes paid by my fellow citizens. This research was supported by grants from the National Science Foundation, NSF/EPS-1006891 and NSF/AST-0708551, and through TeraGrid resources provided by NCSA and LONI under grants TG-AST090104 and TG-MCA09X003, and by a grant from the National Aeronautics and Space Administration, NASA/ATP-NNX10AC72G. This material is also based upon work supported by the Louisiana Optical Network Institute (LONI).

Table of Contents

List of Tables

List of Figures

Abstract

We present a numerical method for the study of double white dwarf (DWD) binary systems at the onset of super-Eddington mass transfer. We incorporate the physics of ideal inviscid hydrodynamical flow, Newtonian self-gravity, and radiation transport on a three-dimensional uniformly rotating cylindrical Eulerian grid. Our new method conserves total energy to a higher degree of accuracy than recent smoothed particle hydrodynamics methods and our previous Eulerian grid based method. We present the results of verification tests and we simulate the first 20+ orbits of a binary system of mass ratio $q = 0.7$ at the onset of dynamically unstable direct impact mass transfer. Although the mass transfer rate exceeds the critical Eddington limit by many orders of magnitude, it appears to have very little effect on the accretion flow. We also model over 20 orbits of a DWD of mass ratio $q = 0.4$. In these simulations, the accretion stream detaches from the accretor after 4 orbits and an asymmetric accretion torus forms. We submit these DWD models as the first self-consistent three dimensional simulations of mass transferring DWDs incorporating radiation transport.

When I heard the learn'd astronomer;
When the proofs, the figures, were ranged in columns before me;
When I was shown the charts and the diagrams, to add, divide, and measure them;
When I, sitting, heard the astronomer, where he lectured with much applause in the lecture-room,
How soon, unaccountable, I became tired and sick;
Till rising and gliding out, I wander'd off by myself,
In the mystical moist night-air, and from time to time,
Look'd up in perfect silence at the stars.

– Walt Whitman

1. Introduction

A white dwarf is the end stage of evolution for the overwhelming majority of stars. Although there are only a few thousand observationally confirmed white dwarfs in our own galaxy (McCook & Sion (1999), Kleinman et al. (2004)), theoretical evidence indicates there could be as many as a few billion (Napiwotzki (2009)). When a main sequence star nears the end of its supply of hydrogen fuel, if it is massive enough, temperatures and pressures rise high enough in the core to fuse helium into carbon and oxygen. Helium fusion produces more energy per unit time, and the star swells up under this increased luminosity, becoming a red giant. Because the star is many orders of magnitude larger, it is no longer bound as tightly by gravitation, and stellar winds can drive mass away from the system. When the helium supply is exhausted, if the star is massive enough, carbon and oxygen fuse into heavier elements. The process can continue, with fusion of progressively heavier elements, up until iron. The fusion of iron is endothermic and a star cannot derive any net additional energy from its fusion. When a star more massive than about $9M_{\odot}$ exhausts its supply of fuel, there is no longer sufficient thermal pressure to support the core against gravitational collapse, and a Supernova Type II results (Poelarends et al. (2008)). Most stars, however, never reach this violent end. They continue to lose mass via stellar wind, and in many cases, by interaction with a companion star. Eventually only the dense central core remains. This stellar remnant is a white dwarf. It no longer produces nuclear energy and cools by black body radiation over many billions of years. It is supported against gravity by electron degeneracy pressure. Depending on the mass of its progenitor main sequence star, the white dwarf is composed of elements lighter than iron, with the more massive main sequence stars leading to white dwarfs composed of heavier elements.

Binary star systems, consisting of two stars orbiting about their mutual center of mass, are quite common. Approximately half of the stars in the solar neighborhood are known to be binary systems, and approximately one-fifth of the stellar population consists of three or more gravitationally bound stars (Abt (1983), Tokovinin (1997)). The components of binary star systems are most likely formed at the same time out of the same cloud of gas (for a review of binary star formation see Tohline (2002)). A double white dwarf (DWD) is a binary system composed of two white dwarf stars. Although direct observation confirms the existence of only a few dozen DWDs in our galaxy (e.g. Marsh et al. (1995), Morales-Rueda et al. (2005), Nelemans et al. (2005), Parsons et al. (2011)), theoretical evidence suggests there are approximately 3×10^8 DWDs in the Galaxy, with birth rates of 5×10^{-2}/yr (Nelemans et al. (2001c)). Many of these observed DWDs are in close orbits, with orbital separations on the order of a solar radius and orbital periods on the order of a few hours. Two DWDs, SDSS 1436 and SDSS 1053, have periods

of about an hour and separations less than $0.5R_{\odot}$ (Mullally et al. (2009)).

Because the progenitor main sequence stars of DWDs are too large to fit in such a close orbit, there must be a mechanism for driving binary main sequence stars closer to one another as they evolve into white dwarfs. The consensus theory, reviewed by Postnov & Yungelson (2006), holds that main sequence progenitor stars are pushed closer to one another by "common envelope evolution". When one of the components evolves into a red giant, it can become larger than the orbit of the binary. Its dense core and its main sequence companion then share a common envelope of gas. The frictional force of the envelope against the binary components drives them closer together over time, converting the orbital energy of the binary into thermal energy in the common envelope. This thermal energy drives mass loss from the envelope, and eventually the envelope is ejected, leaving only the white dwarf remnant of the red giant and its main sequence companion. When the main sequence companion evolves to become a red giant, the process can be repeated, driving the components even closer together. The end result is a compact binary with an orbital separation orders of magnitude smaller than the progenitor main sequence binary.

Einstein's theory of general relativity predicts that a time varying quadrupole mass moment will produce gravitational radiation. This is analogous to the electromagnetic radiation produced by accelerating charged particles. Gravitational radiation is very weak and to date it has not been detected. Detectors such as the Laser Interferometer Gravitational-Wave Observatory (LIGO) and the Laser Interferometer Space Antenna (LISA) are designed to detect gravitational radiation from space. Close DWDs are in tight enough orbits that their time varying quadrupole moments can produce significant gravitational radiation. This gravitational radiation forms a low frequency background noise limiting the sensitivity of detectors such as LISA (Hils et al. (1990), Nelemans et al. (2001b), Farmer & Phinney (2002)). It also carries energy and angular momentum away from the DWD, driving the components closer together over time. If driven close enough, one of the white dwarfs can tidally strip mass off its companion, resulting in mass transfer. If the mass transfer causes the star's mass to exceed the Chandrasekhar mass limit, electron degeneracy pressure is no longer sufficient to support the white dwarf against gravity, and runaway nuclear detonation and a Supernovae Type Ia is a possible result (Webbink (1984), Iben & Tutukov (1984), Livio & Riess (2003), Di Stefano (2010)). It is also possible such a system could avoid nuclear detonation and collapse to form a more compact object (Nomoto & Iben (1985), Saio & Nomoto (1985), Mochkovitch & Livio (1990)). Less massive DWDs may merge to form hydrogen poor objects such as R Coronae Borealis variable stars, extreme helium stars, or sub-dwarf B and sub-dwarf O stars (Webbink (1984), Saio & Jeffery (2000), Han et al. (2002), Clayton et al. (2007)). Systems which survive the initial onset of mass transfer likely become AM Canum Vanaticorum (AM CVn) systems (Paczyński (1967), Faulkner et al. (1972), Nelemans et al. (2001a).

When a DWD system undergoes mass transfer, matter falls from one star, the "donor," to its companion, the "accretor." When it strikes the accretor's surface, the in-falling material is shocked and thermal energy is produced. Some of this thermal energy is converted into radiative luminosity. This radiative luminosity has the potential to affect the accretion flow by exerting a pressure force on the in-falling material. For a spherically accreting object, we refer to the radiative luminosity strong enough to counteract the local force of gravity as the "Eddington luminosity." When this limit is exceeded in spherical accretion—that is, when the accretion is "super Eddington"—the rate of accretion is restricted to that which is required to produce the Eddington luminosity. Determining the effect of exceeding this limit in non-spherical accretion flows is a non-trivial matter. In spherical accretion, radiation is required to pass through, and hence interact with, the entire length of the accretion flow in order to escape the system. This

is not true for non-spherical flows and the manner in which radiation affects the flow depends heavily on the particular geometry of the system. Radiation may still significantly interact with the accretion flow, as in the spherical case, or it may be able to escape with very little interaction. Although some progress has been made by analytic means in the study of DWDs experiencing super-Eddington mass transfer (e.g. Han & Webbink (1999), Gokhale et al. (2007)), to realistically model such a system demands three-dimensional numerical simulation.

In recent years there have been many advances in the three-dimensional numerical modeling of mass transferring DWDs. The two dominant paradigms for this purpose are the smoothed particle hydrodynamics (SPH) codes (e.g. Benz et al. (1990), Rasio & Shapiro (1995)) and the Eulerian grid based codes (e.g. Motl et al. (2002), D'Souza et al. (2006), Motl et al. (2007)). In both cases, the laws of fluid hydrodynamics and Newtonian gravity are applied in a three-dimensional space. Some of the more recent SPH codes also employ detailed equations of state and/or nuclear reaction networks (e.g. Segretain et al. (1997), Guerrero et al. (2004), Yoon et al. (2007), Dan et al. (2009)), and recently our group has produced an Eulerian code that incorporates a cold white dwarf equation of state (Even (2010)). None of the aforementioned codes simulate radiative transport. The goal of the research described in this dissertation is to model DWDs undergoing mass transfer at super-Eddington rates using a numerical method that includes the physics of radiation transport and interaction between radiation and matter.

In §2 we describe the basic analytic framework used to describe DWD accretion flows. Our code models radiation transport using the flux-limited diffusion (FLD) approximation, and in §3 we discuss this approximation. In §4 we develop the full set of partial differential equations that our computer code models. In §5 we describe the numerical method itself, and in §6 we present results of verification tests used to test the code. Finally, in §7 and §8, we discuss the results of two sets of simulations of DWDs at the onset of mass transfer produced using our new code.

2. Analytic Framework

The most basic analytic description of a binary system consists of two point masses bound to one another by Newtonian gravity in a coplanar circular orbit. The model is further developed by approximating the binary components as spherical polytropes. Although realistic modeling requires numerical simulation, it is possible to make several broad statements regarding the evolution of DWDs undergoing mass transfer using analytic methods. We can also determine some of the limiting behavior of DWDs undergoing super-Eddington accretion based on the analytic description of classical super-Eddington accretion.

2.1. Roche Lobe Geometry

In an inertial frame, the gravitational potential, Φ, of a point mass binary in a coplanar circular orbit will vary with time as the stars move through their orbits. It is therefore more convenient to express the equations of motion in a frame rotating with the binary orbital frequency, $\mathbf{\Omega}$, and along the same axis as the binary. The "Roche potential", depicted in Figure 2.1, is the appropriate potential in the co-rotating frame. It is given by the expression

$$\Phi_{\text{Roche}}\left(\mathbf{r}\right) = -\frac{GM_1}{|\mathbf{r}-\mathbf{r_1}|} - \frac{GM_2}{|\mathbf{r}-\mathbf{r_2}|} - \frac{1}{2}|\mathbf{\Omega}\times\mathbf{r}|^2, \tag{2-1}$$

where $\mathbf{r}$ is the position vector, M_1 and M_2 are the masses of the two stars, $\mathbf{r_1}$ and $\mathbf{r_2}$ are their respective coordinate locations, and G is Newton's gravitational constant. This potential is time-invariant as long as the point masses remain in the same orbit. The first term on the right hand side (RHS) is the gravitational potential of the first star, the second term is the gravitational potential of the second star, and the third term is the centrifugal potential due to the rotating frame of reference. The orbital frequency is constant in space and time and is given by Kepler's third law,

$$\mathbf{\Omega} = \sqrt{\frac{G\left(M_1+M_2\right)}{|\mathbf{a}|^3}}\hat{\mathbf{z}}, \tag{2-2}$$

where $\mathbf{a} := \mathbf{r_1} - \mathbf{r_2}$ is the constant orbital separation vector and $\hat{\mathbf{z}}$ is the unit vector in the direction perpendicular to the orbital plane.

For a particle moving along a ballistic trajectory, the time-invariant binding energy is

$$\epsilon_{\text{rot}} := \Phi_{\text{Roche}} + \frac{1}{2}u_{\text{rot}}^2, \tag{2-3}$$

where u_{rot} is the magnitude of the particle velocity in the rotating frame. The particle's momentum is governed by

$$\frac{d}{dt}\mathbf{u}_{\text{rot}} := -\nabla\Phi_{\text{Roche}} - 2\mathbf{u}_{\text{rot}}\times\mathbf{\Omega}, \tag{2-4}$$

where $\mathbf{u}_{\text{rot}}$ is the velocity vector in the rotating frame. The first term on the RHS is the force generated by the Roche potential. The second term is the Coriolis force. Because the Coriolis force is always perpendicular to the particle velocity, it does not contribute to the binding energy.

The mass ratio is defined as

$$q := \frac{M_2}{M_1}. \tag{2-5}$$

Figure 2.1 shows contours of the Roche potential for a binary of mass ratio $q = 0.4$. The three saddle points, referred to as L1, L2, and L3, and the two maxima, referred to as L4 and L5,

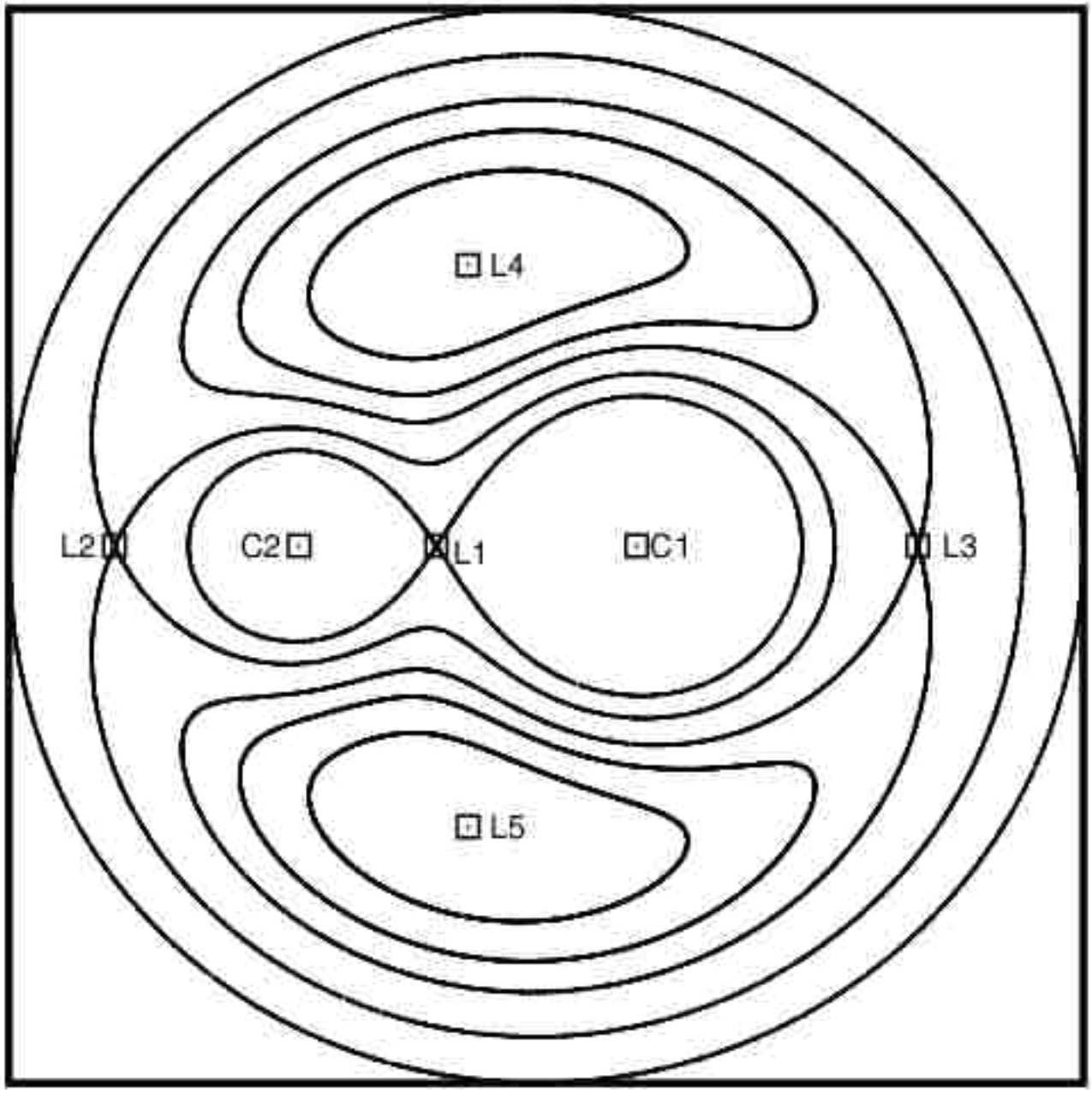

Fig. 2.1.— Contours of the Roche potential for a binary of mass ratio $q = 0.4$. L1, L2, and L3 are saddle points. L4 and L5 are local maxima. C1 and C2 are local minima and correspond to the location of the center of mass of each star. The Roche potential at the outermost contour is the same as the Roche potential at L1.

are called the "Langrangian points". The L1 point is the "inner Lagrangian point." The "Roche lobe" of each star is defined as the area around the star in which the force generated by the Roche potential, $-\nabla\Phi_{\rm Roche}$, points towards the star. In order for a ballistic particle within a star's Roche lobe to escape the from the Roche lobe, its total energy must satisfy $\epsilon_{\rm rot} > \Phi_{\rm L1}$, where $\Phi_{\rm L1}$ is the Roche potential at the L1 point.

2.2. Roche Lobe Overflow

Under the assumption that the stars are spherically symmetric, the Roche potential is correct for all points outside the stars' boundaries. We can approximate a spherical star using the polytropic equation of state,

$$P_{\text{poly}} := K\rho^{1+\frac{1}{n}}, \tag{2-6}$$

where P_{poly} is the pressure, K is the polytropic constant, ρ is the mass per unit volume, and n is the polytropic index. Equation (2-6) and the equation of hydrostatic balance,

$$\nabla P_{\text{poly}} + \nabla\Phi_{\text{Roch}} = 0, \tag{2-7}$$

leads to

$$\frac{d}{dr}\left[(n+1)\,K\rho^{\frac{1}{n}} + \Phi\right] = 0, \tag{2-8}$$

where r is the distance from the center of the polytrope. Stellar models of this kind obey the mass-radius relationship

$$R \propto M^{\frac{1-n}{3-n}}, \tag{2-9}$$

where R is radius of the polytrope and M is its mass (Padmanabhan (2000)). Chandrasekhar (1939) shows that using equation (2-8) with $n = \frac{3}{2}$ is a good approximation for low mass white dwarfs. For this n, $R \propto M^{-\frac{1}{3}}$ and mass varies inversely with radius.

When one star is larger than its Roche lobe, matter falls under gravity from the L1 point towards its companion star. This is known as Roche lobe overflow (RLOF). Although the Roche lobe is not spherical, we may construct a rough model by treating the donor star as a polytrope with a radius equal to the "effective radius" of the Roche lobe. The effective radius of the Roche Lobe is the radius of the sphere which has the same volume as the Roche lobe. Kopal (1959) gives an approximation for the radius of a Roche lobe filling $n = \frac{3}{2}$ polytrope,

$$\frac{R_2}{a} \approx \frac{2}{3^{\frac{3}{4}}}\left(\frac{M_1}{M_1+M_2}\right)^{\frac{1}{3}}, \tag{2-10}$$

where M_2 is the mass of the donor, M_1 is the mass of the accretor, R_2 is the radius of the donor, and a is the orbital separation.

The in-falling matter stream possesses the specific angular momentum of matter at the L1 point and hence the stream will not flow in a straight line between donor and accretor. If the radius of the accretor is not large enough, the in-falling matter will miss the accretor on its first pass and instead orbit the accretor. As matter from the donor accumulates around the accretor, a disc is formed. The "circularization radius,"

$$\frac{R_{\text{circ}}}{a} := (1+q)\,(0.500 - 0.227\log q)^4\,, \tag{2-11}$$

(see Frank et al. (2002)), is approximately the smallest distance the in-falling matter will pass by the accretor. Assuming both stars have the same polytropic constant, K, and using equations (2-9), (2-10), and (2-11), we can derive the relation

$$\frac{2}{3^{\frac{3}{4}}}\left(\frac{q^2}{1+q}\right)^{\frac{1}{3}} = (1+q)\,(0.5 - 0.227\log q)^4\,. \tag{2-12}$$

This equation has a single real root at $q \approx 0.35$. Under this simplified analytic approach, the accretion stream directly impacts the accretor if $q \gtrsim 0.35$. If the accretor cannot absorb the accreted mass quickly enough, however, a torus of material builds up along the accretor's equator. This torus can deflect the accretion stream, causing it to detach from the surface of the accretor. Guillochon et al. (2010) found this to occur in a three-dimensional SPH simulation of a DWD with $q = 0.5$. The $q = 0.4$ runs described in §8 also exhibit this effect.

The dynamical time of a star with radius R and mass M, as given by Binney & Tremaine (1987), is

$$t_{\rm d} := \sqrt{\frac{R^3}{4GM}}. \tag{2-13}$$

This is the time required for a point mass to drop from the surface of a sphere of uniform density to its center under gravity. Disturbances from equilibrium propagate over the star approximately on this time scale. Using equations (2-2), (2-10), and (2-13), we can derive a relationship for the ratio of the orbital period to the dynamical time scale of a Roche lobe filling donor with polytropic index $n = \frac{3}{2}$,

$$\frac{t_p}{t_d} \approx 20\sqrt{1 + q^{-1}}. \tag{2-14}$$

At a minimum, therefore, there are 20 dynamical timescales per orbit. As discussed in §6.7, this means a numerical simulation must be able to accurately evolve over many hundreds of dynamical time scales for models that evolve for dozens of orbits.

2.3. Stability of Mass Transfer

For an $n = \frac{3}{2}$ polytrope, as the donor loses mass to the accretor, the donor becomes larger due to its inverse mass-radius relationship. The Roche geometry will also change. If the size of the donor Roche lobe relative to the donor grows smaller with time, the donor reaches deeper contact and the mass transfer rate increases. Conversely, if it grows larger with time, the mass transfer rate will decrease. In the former case, if the Roche lobe continues to shrink, the mass transfer is unstable. In the latter case, the mass transfer is stable and can continue for long periods.

The orbital momentum of the binary, given by equation (4.13) of Frank et al. (2002), is

$$J_{\rm orb} := M_1 M_2 \sqrt{\frac{Ga}{M_1 + M_2}}. \tag{2-15}$$

Using equations (2-9), (2-10), and (2-15), we can derive the relation

$$\frac{\dot{M}_2}{M_2} := \frac{\dot{J}_{\rm orb}/J_{\rm orb}}{\frac{2}{3} - q\beta - \frac{1}{3}\frac{q}{q+1}(1-\beta)}, \tag{2-16}$$

where β is defined such that

$$\dot{M}_1 := -\beta \dot{M}_2. \tag{2-17}$$

If the mass transfer is driven by gravitational radiation, $J_{\rm orb}$ will be negative. Since mass transfer from M_2 to M_1 implies $\dot{M}_2 < 0$, the denominator of equation (2-16) must be positive and, therefore, the condition

$$q\beta + \frac{1}{3}\frac{q}{q+1}(1-\beta) < \frac{2}{3}, \tag{2-18}$$

must be satisfied for stable mass transfer. The highest value of q which satisfies equation (2-18) is referred to as the critical mass ratio, $q_{\rm crit}$. For conservative mass transfer, where $\beta = 1$, equation (2-18) reduces to $q < \frac{2}{3}$ and $q_{\rm crit} = \frac{2}{3}$. Note that this analysis assumes that the binary is synchronously rotating. The mass transfered from donor to accretor carries angular momentum with it and spins up the accretor. As discussed by Marsh et al. (2004) and Gokhale et al. (2007), if the tidal interaction between donor and accretor is not sufficiently efficient at returning angular momentum to the orbit, for conservative mass transfer, $q_{\rm crit}$, can in fact be lower than $\frac{2}{3}$. This value is therefore only an upper-bound, $q_{\rm crit} \leq \frac{2}{3}$. When $\beta < 1$,

$$q_{\rm crit} = \frac{\sqrt{4\beta^2 - 4\beta + 25} + 1 - 2\beta}{6\beta}. \tag{2-19}$$

For $\beta \geq 0$, the critical mass ratio, $q_{\rm crit}$, increases with a decrease in β. Therefore, under the assumption that mass lost from the system does not significantly interact with the binary as it escapes, mass loss has a stabilizing effect on the mass transfer.

2.4. The Eddington Limit

At the onset of DWD mass transfer, the accretion luminosity very likely will exceed the classical Eddington luminosity limit (Webbink (1984), Iben (1988)). This luminosity is

$$L_{\rm Edd} = \frac{4\pi c G M_1 m_p}{\sigma_T}, \tag{2-20}$$

(see Frank et al. (2002)) where σ_T is the Thomson cross section for electron scattering, m_p is the mass of a proton, and c is the speed of light. For spherically symmetric accretion onto a spherical body, the Eddington luminosity is the luminosity which is sufficient to balance the force of gravity. Because both the radiative luminosity and the force of gravity drop as r^{-2} under spherical symmetry, $L_{\rm Edd}$ is constant in space.

The rate at which energy is lost from the donor by mass transfer is accretion luminosity

$$L_{\rm acc} := -\dot{M}_2 \left(\Phi_{\rm L1} - \Phi_*\right), \tag{2-21}$$

where $\Phi_{\rm L1}$ and Φ_* are the Roche potentials at the L1 point and the surface of the accretor, respectively. When the mass transfer rate onto the accretor exceeds the critical value,

$$\dot{M}_{\rm crit} = \frac{4\pi c G M_1}{\sigma_T \left(\Phi_{\rm L1} - \Phi_*\right)}, \tag{2-22}$$

the accretion luminosity exceeds the Eddington luminosity. The force of radiation then exceeds the force of gravity, and mass can be driven away. If we assume that the mass lost from the system is driven from the surface of the accretor to infinity with just enough energy to escape, the energy loss rate due to mass loss is

$$L_{\rm loss} := (1 - \beta)\dot{M}_2 \Phi_*. \tag{2-23}$$

Energy conservation requires $L_{\rm acc} = L_{\rm Edd} + L_{\rm loss}$. Using this fact and equations (2-21) and (2-23), we arrive at equation (21) from Han & Webbink (1999),

$$-\dot{M}_2 \left(\Phi_{\rm L1} - \Phi_*\right) = (1 - \beta)\, \dot{M}_2 \Phi_* + L_{\rm Edd}. \tag{2-24}$$

Note that when the accretion is highly super-Eddington and $L_{\rm acc} \gg L_{\rm Edd}$, $\beta \approx \Phi_{\rm L1}/\Phi_*$.

For a realistic interacting DWD the accretion flow is far from spherical and the radiation from accretion may be able to escape the flow before significantly interacting with it. In this case the rate of accretion onto the accretor exceeds $-\beta\dot{M}_2$. The simplistic assumption that all mass lost from the system is driven from the surface of the accretor to infinity is also unrealistic. Lost mass may have energy in excess of what is required for escape to infinity. Conversely, a significant fraction of the mass removed from the accretion flow by radiative forces may not have enough energy to escape the system and remain in a common envelope. The frictional forces present in the common envelope serve to drive the binary closer together. To account for the effects of radiative transport in the complex geometry of DWD accretion, potentially in the presence of a common envelope, requires numerical simulations that can couple radiation to hydrodynamic flows.

3. Approximations to the Equation of Radiation Transport

The derivation of the equation of radiative transfer is similar to the derivation of the equations for fluid dynamics in that the radiation is assumed to approximate a continuum for the spatial scales involved. That is, it is assumed that the fluid is made up of a sufficient density of particles that it is possible to form a volume large enough to contain enough particles that statistical deviations are insignificant, but at the same time, small enough that the mathematics of continuous variables can be applied. Such a volume is a referred to as a "fluid element". In the fluid approximation for matter, it is assumed that for any given fluid element the momentum of the particles in the element consists of a component which is stochastic in its distribution (i.e. the pressure) plus a component consisting of a momentum in only one direction (i.e. the bulk momentum). This assumption is reasonable because with a sufficient number of particles per fluid element, any non-thermal momentum distribution, other than the bulk motion of the fluid element, will quickly thermalize. The particles in a photon gas, however, do not react with one another, and therefore any arbitrary distribution of momenta is possible for a given fluid element. Much of the following is found in reference works on radiation hydrodynamics such as Castor (2004) and Mihalas & Mihalas (1984).

3.1. The Radiative Transport Equation

The radiative intensity, $I_\nu = I_\nu(\mathbf{x}, \boldsymbol{\omega}, \nu, t)$, is defined as the energy flow per unit time per unit frequency per unit surface angle in a direction defined by the unit vector $\boldsymbol{\omega}$, at a frequency ν, position in space $\mathbf{x}$, and time t. The integrated flow rate out of a fluid element contained by the surface S enclosing a volume is $\int_S c\boldsymbol{\omega} I_\nu \cdot d\mathbf{a}$, where $d\mathbf{a}$ is the differential area vector perpendicular to the surface S. Using Green's theorem this may be rewritten as $\int_V \nabla \cdot c\boldsymbol{\omega} I_\nu dV$. The total time rate of change of I_ν for a fluid element will include the flow of radiation through the surface of the element as well as any sources or sinks of radiation within the element. The equation of radiative transfer can thus be written as

$$\frac{1}{c}\frac{\partial}{\partial t} I_\nu + \boldsymbol{\omega} \cdot \nabla I_\nu = j_\nu - k_\nu I_\nu, \tag{3-1}$$

where j_ν and k_ν are the emissivity and absorption coefficient. Note that the direction vector, $\boldsymbol{\omega}$, can go inside or outside of the ∇, since $\boldsymbol{\omega}$ does not depend on $\mathbf{x}$. The opacity, k_ν, is in units of cross section per unit volume.

Unlike the four-dimensional fluid equations, the equation for radiative transfer is seven-dimensional. Like the fluid equations, there are three spatial dimensions, $\mathbf{x}$, and one temporal dimension, t. There are an additional three dimensions in the momentum vector, $h\nu\boldsymbol{\omega}/c$, where h is Planck's constant. This vector can be thought of as consisting of two directional components and one photon frequency component.

The moments of the radiative intensity are defined as integrals over all angles of the intensity multiplied by a power of the angular direction vector $\boldsymbol{\omega}$. The first three moments are the radiation energy density

$$E_\nu = \frac{1}{c}\int_\Omega I_\nu d\Omega, \tag{3-2}$$

the radiative flux

$$\mathbf{F}_\nu = \int_\Omega I_\nu \boldsymbol{\omega} d\Omega, \tag{3-3}$$

and the radiative stress tensor

$$\mathbf{P}_\nu = \frac{1}{c}\int_\Omega I_\nu \boldsymbol{\omega}\boldsymbol{\omega} d\Omega. \tag{3-4}$$

Note that the bold faced terms are vectors with the exception of $\mathbf{P}_\nu$, which is a is a 2^{nd} rank tensor. Higher order moments can be similarly defined. The 0^{th} moment has one independent component, the 1^{st} has three independent components, the 2^{nd} has five, and the n^{th} moment has $2n+1$ independent components.

Equation (3-1) can be similarly integrated. The 0^{th} and 1^{st} moment equations are

$$\frac{\partial}{\partial t}E_\nu + \nabla\cdot\mathbf{F}_\nu = \int_\Omega (j_\nu - k_\nu I_\nu) d\Omega, \tag{3-5}$$

$$\frac{1}{c}\frac{\partial}{\partial t}\mathbf{F}_\nu + c\nabla\cdot\mathbf{P}_\nu = \int_\Omega (j_\nu - k_\nu I_\nu)\boldsymbol{\omega} d\Omega. \tag{3-6}$$

In general, j_ν and k_ν are functions of $\boldsymbol{\omega}$. By choosing the proper frame of reference, however, it is possible to make j_ν and k_ν independent of $\boldsymbol{\omega}$. For this special case we can use equations (3-2) and (3-3) to write equations (3-5) and (3-6) as

$$\frac{\partial}{\partial t}E_\nu + \nabla\cdot\mathbf{F}_\nu = 4\pi j_\nu - c k_\nu E_\nu, \tag{3-7}$$

$$\frac{1}{c}\frac{\partial}{\partial t}\mathbf{F}_\nu + c\nabla\cdot\mathbf{P}_\nu = -k_\nu \mathbf{F}_\nu. \tag{3-8}$$

Note that since j_ν is not a function of $\boldsymbol{\omega}$ in this case, for odd multiples of $\boldsymbol{\omega}$, j_ν integrates to zero.

Higher moment equations can be derived, but the set cannot be closed without an infinite number of moment equations. This is because the n^{th} moment equation contains terms with the $n+1^{\text{th}}$ moment. If the set can be closed by making approximating assumptions about one of the moments, it is possible to derive a set of equations which do not depend on $\boldsymbol{\omega}$. This eliminates the two dimensions contained in $\boldsymbol{\omega}$, reducing the single seven-dimensional equation (3-1) to a set of five-dimensional moment equations.

3.2. Interaction Between Radiation and Gas

The conventional names "emissivity coefficient" for j_ν and "absorption coefficient" for k_ν are misnomers as each may represent a combination of sources and sinks. More accurately, j_ν represents all sources and sinks that do no depend on I_ν, and $k_\nu I_\nu$ represents sources and sinks that depend linearly on I_ν. Thermal emission does not depend on I_ν and therefore appears in j_ν. The rate of stimulated emission in a given direction, $\boldsymbol{\omega}$, however, depends on the amount of radiative intensity available in that direction. Stimulated emission, therefore, is actually accounted for in the absorption coefficient, k_ν. Thomson scattering is treated as an absorption and immediate re-emission of a photon. Since the absorption rate in this case is proportional to I_ν, absorption due to scattering appears in k_ν. The immediate re-emission is treated as isotropic in the rest frame of the fluid, and therefore this opposing effect is accounted for in j_ν.

A simplifying assumption is that of local thermodynamic equilibrium (LTE). Under LTE, the distribution of emitted photons in a fluid element follows Planck's law. This assumption usually holds for optically thick media but can fail in regions where the gas is diffuse. If thermal emission is the only source of emissivity in j_ν, this allows the emissivity to be written as

$$j_\nu = k_\nu B_\nu, \tag{3-9}$$

where B_ν is the frequency dependent Planck function. Scattering may be added as a second term, $\sigma_s E_\nu$, where σ_s is the scattering cross section.

The radiation field couples to the gas through exchange of energy and momentum. To conserve energy and momentum, the source terms that appear on the RHS of the 0^{th} and 1^{st} moment equations for the radiative intensity must appear as opposing terms on the RHS of the 0^{th} and 1^{st} moment equations for the gas. As in Castor (2004), we define the four-vector $(g^0, \mathbf{g})$ as the integral of terms on the RHS of equations (3-5) and (3-6),

$$g^0 = \int_0^\nu \int_\Omega (j_\nu - k_\nu I_\nu) d\Omega d\nu, \tag{3-10}$$

$$\mathbf{g} = \frac{1}{c} \int_0^\nu \int_\Omega (j_\nu - k_\nu I_\nu) \mathbf{n} d\Omega d\nu. \tag{3-11}$$

For the special case where j_ν and k_ν are not functions of $\boldsymbol{\omega}$, these terms are

$$g^0 = 4\pi j - c\kappa_E E_R, \tag{3-12}$$

$$\mathbf{g} = -\frac{\chi}{c} \mathbf{F}, \tag{3-13}$$

where E_R, j, and $\mathbf{F}$ are the respective integrals over frequency of E_ν, j_ν, and $\mathbf{F}_\nu$. The quantities κ_E and χ are the energy mean and flux mean opacities, defined respectively as

$$\kappa_E := \frac{1}{E_R} \int_0^\infty k_\nu E_\nu d\nu, \tag{3-14}$$

$$\chi := \frac{1}{|\mathbf{F}|} \int_0^\infty k_\nu |\mathbf{F}_\nu| d\nu. \tag{3-15}$$

To conserve energy and momentum, we subtract g^0 and $\mathbf{g}$ from the RHS of the gas fluid energy and momentum equations, respectively (see equations (4-2) and (4-3)).

3.3. Approximations to the Transport Equation

Deterministic integration of seven-dimensional problems of any useful size is outside the capability of even the most powerful computers. Therefore, in order to solve equation (3-1) numerically, sacrifices must be made. There are three standard approaches to this problem:

1. Use non-deterministic methods. Using Monte-Carlo techniques it is possible to solve the full seven-dimensional problem (e.g. Wolf et al. (1999), Nayakshin et al. (2009)). Although in principle these techniques solve the full equation, stochastic noise can be a limiting factor.
2. Reduce the number of spatial and/or directional dimensions by choosing problems with symmetry. For example, the VULCAN/2D code (Livne et al. (2004), Hubeny & Burrows (2007), Ott et al. (2008)), treats the gas as axi-symmetric, reducing the problem to six-dimensions.
3. Eliminate the directional terms entirely by using the moment equations (e.g. equations (3-7) and (3-8), closing them by making assumptions about the highest order moment used. Most codes that use this method evolve either the first moment equation or the first and second moment equations. The HERACLES code of González et al. (2007) use the latter approach. The Zeus-MP2 code of Hayes et al. (2006), the FLASH code of Fryxell

et al. (2000), as well as the code described in this paper, uses the former approach. This approach, known as the FLD approximation, is rooted in the diffusion approximation for radiation transport.

The diffusion approximation rests on the assumption that the mean free path of a photon is small compared to the spatial scale of the problem. That is, $1/k_\nu < l$, where l is the length scale of the problem. This assumption holds true for many astrophysical phenomena, for example, in the interiors of stars. Rearranging equation (3-1), we obtain

$$I_\nu = \frac{j_\nu}{k_\nu} - \frac{1}{k_\nu}\frac{1}{c}\frac{\partial}{\partial t}I_\nu - \frac{1}{k_\nu}\boldsymbol{\omega}\cdot\nabla I_\nu. \tag{3-16}$$

A 0^{th} order approximation for I_ν is j_ν/k_ν. Substituting this into the above equation yields a 1^{st} order approximation,

$$I_\nu = \left(\frac{j_\nu}{k_\nu} - \frac{1}{k_\nu}\frac{1}{c}\frac{\partial}{\partial t}\frac{j_\nu}{k_\nu}\right) - \left(\frac{1}{k_\nu}\boldsymbol{\omega}\cdot\nabla\frac{j_\nu}{k_\nu}\right). \tag{3-17}$$

For even moments, the second term on the RHS vanishes under integration of all angles and the first term vanishes for odd moments. The first three moments are

$$E_\nu = 4\pi\frac{j_\nu}{k_\nu} - \frac{4\pi}{k_\nu}\frac{1}{c}\frac{\partial}{\partial t}\frac{j_\nu}{k_\nu}, \tag{3-18}$$

$$\mathbf{F}_\nu = -\frac{1}{k_\nu}\nabla\frac{j_\nu}{k_\nu}, \tag{3-19}$$

$$\mathbf{P}_\nu = \frac{4\pi}{3}\frac{j_\nu}{k_\nu}\mathbf{I} - \frac{4\pi}{3k_\nu}\frac{1}{c}\frac{\partial}{\partial t}\frac{j_\nu}{k_\nu}\mathbf{I}, \tag{3-20}$$

where $\mathbf{I}$ is the identity 2^{nd} rank tensor. The tensor $\mathbf{P}_\nu$ can be expressed in terms of E_ν using equation (3-18) to get

$$\mathbf{P}_\nu = \frac{1}{3}E_\nu\mathbf{I}. \tag{3-21}$$

Substituting this into equation (3-8) we obtain,

$$\frac{\partial}{\partial t}\mathbf{F}_\nu + \frac{1}{3}c^2\nabla E_\nu = -c\chi\mathbf{F}_\nu. \tag{3-22}$$

Equation (3-22) with equation (3-7) form a closed set. This is known as the Eddington approximation. Under the assumption that the second term on the left hand side (LHS) of equation (3-22) and the RHS are much larger than the first term on the LHS, equation (3-22) becomes

$$\mathbf{F}_\nu = -\frac{c}{3\chi}\nabla E_\nu. \tag{3-23}$$

This is the diffusion approximation. Since $\mathbf{F}_\nu$ can now be expressed without time derivatives, we only need to evolve equation (3-5) in time.

Numerically integrating the diffusion approximation for radiation with the normal gas fluid equations has two problems. First, j_ν and k_ν are in general functions of $\boldsymbol{\omega}$, but the diffusion approximation requires j_ν and k_ν be independent of $\boldsymbol{\omega}$. Secondly, the diffusion approximation allows for arbitrarily high propagation speeds, which is of course, unphysical.

Many radiative processes, such as absorption and thermal emission, can be accounted for with absorption and emission coefficients that are independent of $\boldsymbol{\omega}$, so long as they are expressed

in the rest frame of the fluid. If the momentum distribution of particles from a source is isotropic in the rest frame, it is shifted towards the source's direction of travel in the frame moving with the source. We can make j_ν and k_ν independent of $\boldsymbol{\omega}$ with the appropriate coordinate transformation. This reduces the dimensionality of the radiative transfer equation to five: three spatial, one time, and one frequency dimension. Integrating the equations over ν further reduces the problem's complexity to four dimensions. In the "co-moving" frame approach, j_ν, k_ν, I_ν, and the moments of I_ν are taken in the frame co-moving with the fluid. This is the approach we implement in our new code. Another possible method is the "mixed frame approach", in which j_ν and k_ν are taken in the co-moving frame but I_ν and its moments are taken in the lab frame (Krumholz et al. (2007)).

To transform to the co-moving frame, we perform a Lorentz transformation on the variables ν, $\boldsymbol{\omega}$, I_ν, j_ν, and k_ν. The following are taken from Castor (2004):

$$I_\nu = (\frac{\nu}{\nu_o})^3 I_{\nu o}; \tag{3-24}$$

$$j_\nu = (\frac{\nu}{\nu_o})^2 j_{\nu o}; \tag{3-25}$$

$$k_\nu = (\frac{\nu_o}{\nu}) k_{\nu o}; \tag{3-26}$$

$$\nu = \nu_o(1 + \boldsymbol{\omega}_o \cdot \frac{\mathbf{u}}{c}); \tag{3-27}$$

$$\boldsymbol{\omega} = \frac{\frac{\mathbf{u}}{c} + \boldsymbol{\omega}_o}{(1 + \boldsymbol{\omega}_o \cdot \frac{\mathbf{u}}{c})}. \tag{3-28}$$

The "o" subscripts refer to the co-moving frame. The velocity $\mathbf{u}$ refers to the velocity of the co-moving frame. This is the same as the velocity of the fluid. The last two equations are not exact but are accurate to $O(\frac{u}{c})$. There is nothing to be gained from retaining terms higher than $O(\frac{u}{c})$ because the gas fluid equations we are using are non-relativistic and hence only accurate to $O(\frac{u}{c})$ themselves.

Substituting equations (3-24) through (3-28) into equation (3-1), integrating equation (3-1) over $\boldsymbol{\omega}_o$, and then integrating over the frequency, ν, leads to the gray field moment equations for E_R and $\mathbf{F}$ in the co-moving frame. These are

$$\frac{\partial}{\partial t} E_R + \nabla \cdot (E_R \mathbf{u}) + \nabla \cdot \mathbf{F} + \nabla \mathbf{u} : \mathbf{P} + \frac{2\mathbf{a}}{c^2} \cdot \mathbf{F} = 4\pi j - c\kappa_E E_R, \tag{3-29}$$

$$\frac{\partial}{\partial t} \mathbf{F} + \nabla \cdot (\mathbf{F}\mathbf{u}) + c^2 \nabla \cdot \mathbf{P} + \mathbf{a} \cdot \mathbf{P} + \mathbf{a} E_R + \nabla u \cdot \mathbf{F} = -c\chi \mathbf{F}, \tag{3-30}$$

where $\mathbf{a}$ is defined as $\frac{\partial \mathbf{u}}{\partial t}$ (Castor (2004)).

3.4. Flux-Limited Diffusion

By substituting the frequency integrated versions of equations (3-23) and (3-21) into equation (3-29) we have a single four-dimensional equation for the radiation energy density. The problem is that the diffusion approximation allows for unphysical propagation speeds. The radiative flux, $\mathbf{F}$, is the total amount of energy flowing through a unit of area per unit time. In the diffusion approximation, at a given point in space, all the radiative energy is traveling in the same direction.

The speed of propagation of this energy must satisfy $\mathbf{F} = \mathbf{u}_E E$, where $\mathbf{u_E}$ is the propagation velocity of the radiation energy. Using this fact, and rearranging equation (3-23), we get

$$\mathbf{u_E} = -\frac{c}{3\chi E_R}\nabla E_R = \frac{1}{3}c\Theta\mathbf{n_E}, \tag{3-31}$$

where $\mathbf{n_E} := -\nabla E_R / |\nabla E_R|$ is the direction of propagation for the radiation. The quantity Θ is defined as

$$\Theta := \frac{|\nabla E_R|}{\chi E_R}. \tag{3-32}$$

Note that if $\Theta > 3$ the energy propagates at super-luminal speeds. Not only is this physically implausible, but it can lead to numerical problems as well, as the maximum stable time step size depends in part on the maximum speed of propagation for the radiation.

To get around this problem, Levermore & Pomraning (1981) developed the concept of the radiative "flux-limiter". The resulting equations are the FLD approximation. The idea is to modify equation (3-23) so that it goes to the limit of $\mathbf{F} = cE\mathbf{n_E}$ when Θ gets very large. Defining Λ_E as the flux limiter, we can rewrite equation (3-23) as

$$\mathbf{F} = -\left(\frac{c\Lambda_E}{\chi}\right)\nabla E_R. \tag{3-33}$$

The flux limiter, Λ_E, is chosen as a function of Θ that satisfies $\lim_{\Theta\to 0}\Lambda_E = 1/3$ and $\lim_{\Theta\to\infty}\Lambda_E = 1/\Theta$. There are an infinite number of possibilities for Λ_E. Two very simple forms are $\Lambda_E = 1/\max(3,\Theta)$ or $\Lambda_E = 1/(3+\Theta)$. In Levermore & Pomraning (1981), a flux limiter is derived directly from the radiative transfer equation itself, under the assumption that the normalized intensity, $\psi_\nu = I_\nu/(cE_\nu)$, is a slowly varying function in space and time. That is,

$$\frac{\partial}{\partial t}\psi_\nu + \boldsymbol{\omega}\cdot\nabla\psi_\nu := 0. \tag{3-34}$$

The result, equation (22) from Levermore & Pomraning (1981), is

$$\Lambda_E = \frac{1}{\Theta}\left[\coth(\Theta) - \frac{1}{\Theta}\right]. \tag{3-35}$$

A rational approximation to this function is

$$\Lambda_E = \frac{2+\Theta}{6+3\Theta+\Theta^2}. \tag{3-36}$$

We see both limiters provide the proper limiting behaviors, specifically,

$$\lim_{\Theta\to 0}\mathbf{F} = -\frac{c}{3\chi}\nabla E_\nu, \tag{3-37}$$

$$\lim_{\Theta\to\infty}\mathbf{F} = cE_R\mathbf{n}_E. \tag{3-38}$$

Equations (3-37) and (3-23) are identical, as they should be; and equation (3-38) corresponds to the case of unidirectional free-streaming radiation, that is, $I(\mathbf{x},t,\boldsymbol{\omega}) = cE_R\delta(|\boldsymbol{\omega}-\mathbf{n}_E|)$, where δ is the Dirac delta function. Integrating this last expression over all angles for the 2^{nd} moment yields

$$\mathbf{P} = E_R\mathbf{n}_E\mathbf{n}_E. \tag{3-39}$$

Thus to accommodate the free-streaming limit, we must also modify equation (3-21). The solution employed in our new code is the same as in Hayes et al. (2006) and others. This is

$$\mathbf{P} = \frac{1}{2}(1-f)\mathbf{I}E_R + \frac{1}{2}(3f-1)\mathbf{n}_E\mathbf{n}_E E_R, \tag{3-40}$$

where $f = \Lambda_E + (\Lambda_E \Theta)^2$. This definition for the so called Eddington tensor satisfies equation (3-21) in the diffusive limit and equation (3-39) in the free- streaming limit.

Since we are only interested in the regime where $u/c << 1$, the $2\mathbf{a} \cdot \mathbf{F}/c^2$ term may be dropped from equation (3-29) to further simplify the problem. Also assuming LTE by using equation (3-9), equation (3-29) becomes

$$\frac{\partial}{\partial t}E_R + \nabla \cdot (E_R \mathbf{u}) + \nabla \cdot \mathbf{F} + \nabla \mathbf{u} : \mathbf{P} = 4\pi\kappa_p B_p - c\kappa_E E_R. \tag{3-41}$$

The quantity, B_p, is the Planck function integrated over frequency,

$$B_p := \frac{\sigma}{\pi}T^4, \tag{3-42}$$

where T is the temperature of the gas, σ is the Stefan-Boltzmann constant, and the Planck mean opacity, κ_p, is

$$\kappa_p = \frac{1}{B_p}\int_0^\infty k_\nu B_p d\nu. \tag{3-43}$$

We use equation (3-41) instead of equation (3-29) to represent the gray field moment equation for E_R in the new code.

The FLD approximation has at least two problems in the free-streaming limit. The first is that it allows for only unidirectional radiation flows. For example, two colliding streams of radiation traveling in different directions will produce a combined stream traveling between the two directions, whereas in the real world the two streams would simply pass right through one another and continue along their original paths. The second problem is that, since the direction of flow is defined by the gradient of the energy distribution, it is not possible to form realistic shadows. As soon as a shadow forms, radiation diffuses into the shadow from its edge. The major advantage that the FLD approximation has over the ordinary diffusion approximation is that the escape of radiation from optically thick media is more accurately handled. At the surface of a star, for instance, radiation can flow outwards from the boundary at arbitrarily high speeds in the diffusion approximation. In the FLD approximation, the propagation speed of radiation from that boundary, relative to the fluid, is limited to the speed of light.

4. The Model Equation Set[1]

As with our previous codes, our new code models the DWD system as a self-gravitating inviscid fluid, governed by the equations of Newtonian gravity coupled to the classical hydrodynamic equations for density, momentum, and gas energy transport. Our earliest codes assumed adiabatic flow and hence did not properly account for the conversion of kinetic energy into thermal energy at shock fronts (i.e. Motl et al. (2002)). This code, as well as another of our recent codes (Even (2010)), properly accounts for entropy generation at shock fronts. This is crucial for the proper modeling of super-Eddington accretion flows, as the generation of heat at the accretion stream's point of impact on the accretor is responsible for the conversion of accretion luminosity into radiative luminosity. Here we model the gas temperature and pressure based on the ideal gas equation of state. The most important additions to the new code are radiation energy transport and the coupling of radiation energy to the momentum and gas energy. These physical processes are the bare minimum required to simulate super-Eddington accretion. They can account for: (1) the conversion of kinetic energy into thermal energy and thermal energy into radiation energy at the accretion stream's point of impact; (2) the transport of radiation energy through space; and (3) the interaction of the resulting radiation energy flux on the momentum of the accretion stream. At the time of this writing, we are unaware of of any three-dimensional simulations of DWD mass transfer which simulate an entire DWD self-consistently and incorporate radiation transport for the entire model. Guillochon et al. (2010) combined an SPH code and the FLASH (Fryxell et al. (2000)) code to simulate DWD mass transfer. The FLASH code models radiative transport, as well as nuclear physics, however, it was used to model only the accretion stream and accretor. The boundary conditions for the FLASH code portion of the simulation were set based on the results of an SPH simulation of the complete binary. Potter (2009) suggested that the DJEHUTY code (Bazán et al. (2003)), which incorporates radiation transport, could be modified to simulate the common envelope phase of DWD mass transfer, however, we have be unable to find any evidence in the literature that the DJEHUTY code has since been modified and used for this purpose.

4.1. Governing Equations

Fundamentally we adopt the same basic set of dynamical governing equations as presented by Hayes et al. (2006) but with the magnetic field set to zero. Specifically, by taking the Eulerian form of equations (1) through (4) in Hayes et al. (2006), adding rotational terms and removing contributions from the magnetic field, our adopted governing equations are:

$$\frac{\partial}{\partial t}\rho + \nabla \cdot \rho\mathbf{u} = 0; \tag{4-1}$$

$$\frac{\partial}{\partial t}\rho\mathbf{u} + \nabla \cdot (\rho\mathbf{u}\mathbf{u} + p\mathbf{I}) = -\rho\nabla\Phi + \frac{\chi}{c}\mathbf{F} - 2\Omega \times \rho\mathbf{u} - \rho\Omega \times (\Omega \times \mathbf{r}); \tag{4-2}$$

$$\frac{\partial}{\partial t}e + \nabla \cdot e\mathbf{u} + p\nabla \cdot \mathbf{u} = -4\pi\kappa_p B_p + c\kappa_E E_R; \tag{4-3}$$

$$\frac{\partial}{\partial t}E_R + \nabla \cdot E_R\mathbf{u} + \nabla \cdot \mathbf{F} + \mathbf{P} : \nabla\mathbf{u} = 4\pi\kappa_p B_p - c\kappa_E E_R. \tag{4-4}$$

[1]A substantial portion of this section and its subsections have been reproduced from Marcello & Tohline (2011) with the permission of the AAS (see Appendix D).

The fluid velocity, $\mathbf{u}$, is defined in the *rotating* frame. The internal gas energy density is e. The gravitational potential, Φ, is determined from Poisson's equation,

$$\nabla^2 \Phi = 4\pi G\rho, \tag{4-5}$$

where G is the gravitational constant. The gas pressure, p, is given by,

$$p = (\gamma - 1)\, e, \tag{4-6}$$

where γ is the ratio of specific heats. We compute T by using equation (4-6) and the ideal gas equation,

$$p = \frac{\mathcal{R}}{\mu}\rho T, \tag{4-7}$$

where μ is the mean molecular weight and $\mathcal{R}$ is the gas constant. We determine B_p using T in equation (3-42).

The radiative flux, $\mathbf{F}$, is given by the FLD approximation of equation (3-33). The flux mean opacity, χ, energy mean opacity, κ_E, and Planck mean opacity, κ_p, are formally given by equations (3-15), (3-14), and (3-43), respectively. In Appendix A we describe how we treat the opacities in the code. We use equation (3-35) for the flux limiter, Λ_E. The symmetric radiative stress tensor, $\mathbf{P}$, is given by equation (3-40). The propagation speed of the radiation energy density under this simple diffusion approximation is not bounded by the speed of light. However, the use of the flux limiter, Λ_E, ensures that this propagation speed never exceeds $|\mathbf{u}| + c$. Although physically we expect that the propagation speed never exceeds c, the elimination of higher order terms in the FLD approximation can, in principle, result in super-luminal radiation transport. At shock discontinuities, kinetic energy is converted into internal gas energy so updating e via equation (4-3) will produce lower internal energies than physically expected. For this reason we generally prefer to update e by first evolving the total gas energy density,

$$E_G := e + \frac{1}{2}\rho u^2, \tag{4-8}$$

then subtracting $\frac{1}{2}\rho u^2$ from E_G to obtain e. Note that E_G is defined in the rotating frame. The equation governing the time-evolution of E_G is obtained by dotting $\mathbf{u}$ into equation (4-2), realizing that,

$$\mathbf{u} \cdot \left(\frac{\partial}{\partial t}\rho\mathbf{u} + \nabla \cdot \rho\mathbf{u}\mathbf{u} \right) \;=\; \frac{1}{2}\left(\frac{\partial}{\partial t}\rho u^2 + \nabla \cdot \rho u^2 \mathbf{u} \right), \tag{4-9}$$

and adding it to equation (4-3). Specifically, we obtain

$$\frac{\partial}{\partial t} E_G + \nabla \cdot (E_G + p)\,\mathbf{u} \;=\; -\rho\mathbf{u} \cdot \nabla\Phi + \mathbf{u} \cdot \frac{\chi}{c}\mathbf{F} - 4\pi\kappa_p B_p + c\kappa_E E_R - \rho\mathbf{u} \cdot \Omega \times (\Omega \times \mathbf{r})\,. \tag{4-10}$$

Equations (4-10) and (4-3) should both correctly describe the time-evolution of e in regions of space where $\mathbf{u}$ is continuous but, in the vicinity of shocks, only equation (4-10) provides the correct description. Hence, we replace equation (4-3) with equation (4-10) in our principal set of governing equations. However, due to the numerical issues described below in connection with equation (5-25), we adopt a dual energy formalism (Bryan et al. (1995)) and evolve equation (4-3) independently.

4.2. Momentum and Energy Conservation

It is useful to examine equation (4-2) to understand how each term might contribute to momentum conservation globally. Integrating equation (4-2) over all space, and using the divergence theorem,

$$\int_V \nabla \cdot \mathbf{v} \; d\mathrm{V} = \int_S \mathbf{v} \cdot \mathbf{da} \tag{4-11}$$

one can show that, when the density and pressure go to zero at large distances from the coordinate origin, the sum of momentum over all space is not altered by the term $\nabla \cdot (\rho \mathbf{u}\mathbf{u} + p\mathbf{I})$. Using equation (4-5) and following Shu (1992), we can rewrite the gravitational term as,

$$\rho \nabla \Phi \;=\; \frac{\nabla^2 \Phi}{4\pi G} \nabla \Phi \;=\; \frac{1}{4\pi G} \nabla \cdot \left(\mathbf{g}\mathbf{g} - \frac{1}{2} \left| \mathbf{g} \right|^2 \mathbf{I} \right), \tag{4-12}$$

where the gravitational acceleration is $\mathbf{g} := -\nabla\Phi$. Since equation (4-12) is zero when $\rho = 0$, momentum will be conserved within any volume containing all the mass of an isolated system. Using equation (3-33), we rewrite the radiative force term as

$$\frac{\chi}{c} \mathbf{F} \;=\; -\Lambda_E \nabla E_R \;=\; -\nabla \cdot \Lambda_E E_R \mathbf{I} + E_R \nabla \Lambda_E. \tag{4-13}$$

In the diffusion limit, $\Theta \to 0$, $\Lambda_E \to \frac{1}{3}$, and $\nabla \Lambda_E \to \mathbf{0}$, therefore the radiation term conserves momentum within any volume in the diffusion limit. Outside of this limit the gas exchanges net momentum with the radiation field. Because we do not evolve the radiative flux $\mathbf{F}$ separately, it is not possible for our method to account for this exchange in a manner which generally conserves momentum. Finally, defining the symmetric stress-energy tensor,

$$\mathbf{T} := \rho \mathbf{u}\mathbf{u} + \mathbf{g}\mathbf{g} + \left(p + \Lambda_E E_R - \frac{1}{2} g^2 \right) \mathbf{I}, \tag{4-14}$$

we can rewrite equation (4-2) as,

$$\frac{\partial}{\partial t} \rho \mathbf{u} + \nabla \cdot \mathbf{T} \;=\; E_R \nabla \Lambda_E - \rho \Omega \times \left(2\mathbf{u} + (\Omega \times \mathbf{r}) \right). \tag{4-15}$$

Written in this form, all the "source" terms, that is, all the terms that have been grouped together on the right hand side (RHS), will contribute to net changes in the sum of momentum over all space. Terms on the LHS are in conservative form.

Motl et al. (2002) have argued that a more accurate dynamical treatment will result from the adoption of an entropy tracer. By defining the entropy tracer,

$$\tau := e^{\frac{1}{\gamma}}, \tag{4-16}$$

in place of the internal energy density, the $p\nabla \cdot \mathbf{u}$ term no longer appears as a source. In terms of τ equation (4-3) becomes,

$$\frac{\partial}{\partial t} \tau + \nabla \cdot \tau \mathbf{u} \;=\; \frac{1}{\gamma \tau^{\gamma - 1}} \left(-4\pi \kappa_p B_p + c \kappa_E E_R \right). \tag{4-17}$$

As in equation (4-15), we have written equation (4-17) in a form that places the non-conservative source terms on the RHS. The term that appears in this case accounts for the exchange of entropy

with the radiation field. As discussed above in the context of equation (4-10), however, in the vicinity of shocks entropy is produced and equation (4-17) does not hold. Hence, through a dual energy formalism (see the discussion associated with equation (5-25)), we will rely on equation (4-10) instead of equation (4-17) in the presence of shocks.

It is worthwhile to ask what expression for the energy density will serve better than E_G to describe total energy conservation when integrated over the volume of our simulated system. Using equation (4-1), the gravitational term on the RHS of equation (4-10) can be written as

$$\rho\mathbf{u}\cdot\nabla\Phi \;=\; \nabla\cdot\rho\Phi\mathbf{u}-\Phi\nabla\cdot\rho\mathbf{u} \;=\; \nabla\cdot\rho\Phi\mathbf{u}+\Phi\frac{\partial}{\partial t}\rho \;=\; \frac{\partial}{\partial t}\frac{1}{2}\rho\Phi+\nabla\cdot\rho\Phi\mathbf{u}+\frac{1}{2}\Phi\frac{\partial}{\partial t}\rho-\frac{1}{2}\rho\frac{\partial}{\partial t}\Phi. \quad (4\text{-}18)$$

Also, using equation (4-1) and the definition,

$$\Phi_{\rm rot} := -\frac{1}{2}|\Omega\times\mathbf{r}|^2, \quad (4\text{-}19)$$

we can rewrite the centrifugal term as,

$$\rho\mathbf{u}\cdot\Omega\times(\Omega\times\mathbf{r}) \;=\; -\rho\mathbf{u}\cdot\nabla\frac{1}{2}|\Omega\times\mathbf{r}|^2 \;=\; \nabla\cdot\rho\Phi_{\rm rot}\mathbf{u}-\Phi_{\rm rot}\nabla\cdot\rho\mathbf{u} \;=\; \frac{\partial}{\partial t}\rho\Phi_{\rm rot}+\nabla\cdot\Phi_{\rm rot}\rho\mathbf{u}. \quad (4\text{-}20)$$

Defining,

$$\mathcal{E}_{\rm con} := E_G+\frac{1}{2}\rho\Phi+\rho\Phi_{\rm rot}, \quad (4\text{-}21)$$

equation (4-10) can be written as

$$\frac{\partial}{\partial t}\mathcal{E}_{\rm con}+\nabla\cdot\left(\mathcal{E}_{\rm con}+p+\frac{1}{2}\rho\Phi\right)\mathbf{u}+\frac{1}{2}\Phi\frac{\partial}{\partial t}\rho-\frac{1}{2}\rho\frac{\partial}{\partial t}\Phi \;=\; \mathbf{u}\cdot\frac{\chi}{c}\mathbf{F}-4\pi\kappa_pB_p+c\kappa_EE_R. \quad (4\text{-}22)$$

Note that $\mathcal{E}_{\rm con}$ represents a sum of kinetic, internal, and potential gas energies. Using equation (4-5) and Green's theorem, we see that the integral over all space of the last two terms on the LHS of equation (4-22) gives,

$$\int_V\left(\frac{1}{2}\Phi\frac{\partial}{\partial t}\rho-\frac{1}{2}\rho\frac{\partial}{\partial t}\Phi\right)\,d^3\mathbf{r} \;=\; \frac{1}{8\pi G}\int_V\left(\Phi\nabla^2\frac{\partial}{\partial t}\Phi-\left(\frac{\partial}{\partial t}\Phi\right)\nabla^2\Phi\right)\,d^3\mathbf{r} \;=\; \frac{1}{8\pi G}\int_S\left(\Phi\nabla\frac{\partial}{\partial t}\Phi-\left(\frac{\partial}{\partial t}\Phi\right)\nabla\Phi\right)\,\cdot d\mathbf{a}. \quad (4\text{-}23)$$

This quantity will go to zero at large distances from the origin for a finite mass distribution. As in equations (4-15) and (4-17), we have written equation (4-22) with conservative terms on the LHS and non-conservative source terms on the RHS. It should therefore be clear that, within the radiation diffusion limit, $\mathcal{E}_{\rm con}$ is a conserved quantity. Note that the contribution to $\mathcal{E}_{\rm con}$ from the gravitational potential is $\frac{1}{2}\rho\Phi$ (instead of $\rho\Phi$) due to the self interactive nature of the gravitational field (see equation (2-19) in Binney & Tremaine (1987)).

Equation (4-10) can also be written as

$$\frac{\partial}{\partial t}\mathcal{E}_{\rm loc}+\nabla\cdot(\mathcal{E}_{\rm loc}+p)\,\mathbf{u} \;=\; \rho\frac{\partial}{\partial t}\Phi+\mathbf{u}\cdot\frac{\chi}{c}\mathbf{F}-4\pi\kappa_pB_p+c\kappa_EE_R, \quad (4\text{-}24)$$

where we have defined

$$\mathcal{E}_{\rm loc} := E_G+\rho\Phi+\rho\Phi_{\rm rot}. \quad (4\text{-}25)$$

For a non-self gravitating fluid, with Φ fixed in time, and absent the radiation terms, $\mathcal{E}_{\rm loc}$ will be a globally conserved quantity. We may consider equation (4-24) to consist of three parts: (1) the LHS, describing the hydrodynamic flow of a "locally conserved" energy, $\mathcal{E}_{\rm loc}$; (2) a contribution to this energy from the first term on the RHS, $\rho\frac{\partial}{\partial t}\Phi$, which is due to the *global* effect of a time varying gravitational potential; and (3) a non-conservative contribution from the remaining terms on the RHS, due to the interaction with the radiation field. We describe $\mathcal{E}_{\rm loc}$ as "locally conserved" because it includes the kinetic, internal, and potential energy that is physically carried by the local flow of the fluid. The difference between $\mathcal{E}_{\rm con}$ and $\mathcal{E}_{\rm loc}$, $-\frac{1}{2}\rho\Phi$, is carried by the global flow of energy between non-adjacent fluid elements due to Newtonian gravity.

Defining the total energy density as

$$\mathcal{E}_{\rm tot} := \mathcal{E}_{\rm con} + E_R, \tag{4-26}$$

we can write the sum of equations (4-10) and (4-4) as

$$\frac{\partial}{\partial t}\mathcal{E}_{\rm tot} + \nabla\cdot\left[\left(\mathcal{E}_{\rm tot} + p + \frac{1}{2}\rho\Phi\right)\mathbf{u} + \mathbf{P}\cdot\mathbf{u}\right] + \frac{1}{2}\Phi\frac{\partial}{\partial t}\rho - \frac{1}{2}\rho\frac{\partial}{\partial t}\Phi \;=\; \mathbf{u}\cdot\left(\nabla\cdot\mathbf{P} - \Lambda_E\nabla E_R\right). \tag{4-27}$$

Again, we have placed non-conservative source terms on the RHS and conservative terms on the LHS. Physically, we should expect the quantity $\mathcal{E}_{\rm tot}$ to be globally conserved, as it is the volume integral over all space of all energy densities: kinetic energy; internal heat energy; gravitational potential energy; rotational potential energy; and radiation energy densities. In the diffusion limit the terms on the RHS will cancel one another, resulting in conservation of $\mathcal{E}_{\rm tot}$. Outside of the diffusion limit the same is not generally true. This is due to the fact that equation (4-4) is a zeroth order approximation to the relativistic radiative transport equation. However, since the overwhelming majority of the energy contained in our models will be in the diffusion limit, we do not expect this will have a significant effect.

In a cylindrical coordinate system rotating about the z axis with constant frequency Ω the components of equation (4-15) are:

$$\frac{\partial}{\partial t}s_R + \nabla\cdot\mathbf{T_R} \;=\; E_R\frac{\partial}{\partial R}\Lambda_E + \frac{T_{\phi\phi}}{R} + 2\rho\Omega u_\phi + \rho R\Omega^2; \tag{4-28}$$

$$\frac{\partial}{\partial t}s_\phi + \nabla\cdot\mathbf{T}_\phi \;=\; E_R\frac{1}{R}\frac{\partial}{\partial\phi}\Lambda_E - \frac{T_{R\phi}}{R} - 2\rho\Omega u_R; \tag{4-29}$$

$$\frac{\partial}{\partial t}s_z + \nabla\cdot\mathbf{T_z} \;=\; E_R\frac{\partial}{\partial z}\Lambda_E; \tag{4-30}$$

where $s_R := \rho u_R$, $s_\phi := \rho u_\phi$, and $s_z := \rho u_z$. The vertical angular momentum density, s_z, is conserved in the radiation diffusion limit. The second terms on the RHS of equations (4-28) and (4-29) are coordinate curvature terms that result from applying the divergence operator to $\mathbf{T}$. By using the inertial frame z-angular momentum density,

$$l_z = R\rho u_\phi + \rho R^2\Omega^2, \tag{4-31}$$

both the coordinate curvature and Coriolis terms in equation (4-29) can be eliminated. The new equation is

$$\frac{\partial}{\partial t}l_z + \nabla\cdot R\mathbf{T}_\phi \;=\; E_R\frac{\partial}{\partial\phi}\Lambda_E. \tag{4-32}$$

Therefore, in the diffusion limit, l_z is also a conserved quantity. A similar transformation cannot be performed on equation (4-28). This is because radial momentum is *not* physically conserved. By choosing a curvilinear coordinate system, we are limited to choosing, at most, two conserved generalized momentum components.

4.3. Reformulated Governing Equations

The binary systems we wish to study will begin their evolution in a state of near equilibrium and, for a significant part of their evolution, we expect them to remain in a state of near equilibrium. With the exception of a few computational zones near their surfaces, each star will begin evolution in the radiation diffusion limit. To accurately evolve such a system requires that quantities which are conserved analytically are also conserved numerically. In particular, we require the conservation of ρ and, in the diffusion limit, the conservation of s_R, l_z, s_z, and $\mathcal{E}_{\rm tot}$. For adiabatic flow in which the radiation and gas temperatures are the same, we also require local conservation of τ. Above we have manipulated equations (4-2), (4-10), (4-4), and (4-3) to illustrate these conserved quantities. Now we develop the same equations, as well as equation (4-1), in a form suitable for adaptation to the numerical method described in §5.

Applying the cylindrical divergence operator in equation (4-28), the radial momentum equation is

$$\frac{\partial}{\partial t}s_R + \frac{1}{R}\frac{\partial}{\partial R}R\left(s_R u_R + p\right) + \frac{\partial}{\partial R}p + \frac{1}{R}\frac{\partial}{\partial \phi}s_R u_\phi + \frac{\partial}{\partial z}s_R u_z + \Lambda_E \frac{\partial}{\partial R}E_R \;= \\ -\rho\frac{\partial}{\partial R}\Phi + \rho R\Omega^2 + 2\rho u_\phi \Omega + \frac{\rho u_\phi^2}{R} + \frac{p}{R}. \quad (4\text{-}33)$$

The second, third, and fourth terms on the RHS come from the last three terms on the RHS of equation (4-28). The pressure term on the LHS can be written $\frac{1}{R}\frac{\partial}{\partial R}Rp = \frac{\partial}{\partial R}p + \frac{p}{R}$, resulting in a $\frac{p}{R}$ on both sides of the equation. Though these terms will analytically cancel one another, as noted by Call et al. (2010), there is no guarantee they will numerically cancel. Because the LHS of our equations will be handled by an explicit advection scheme, and the RHS will be treated by other methods, we remove the $\frac{p}{R}$ term on both sides of the equation. Using equation (4-31), we can write the centrifugal, Coriolis, and remaining coordinate curvature terms as a single term, $\frac{l_z^2}{\rho R^3}$. These changes to equation (4-33) are reflected in equation (4-35).

For our total gas energy equation we will follow equation (4-24) and apply the advection scheme to the quantity $\mathcal{E}_{\rm loc}$. This is the quantity that is physically transported by advection. As we will show below, treating the gas energy equation in this manner results in numerical conservation of $\mathcal{E}_{\rm tot}$ in the diffusion limit.

The full set of equations, in a form suitable for adaptation to our numerical method, is:

$$\frac{\partial}{\partial t}\rho + \frac{1}{R}\frac{\partial}{\partial R}R\rho u_R + \frac{1}{R}\frac{\partial}{\partial \phi}\rho u_\phi + \frac{\partial}{\partial z}\rho u_z \;=\; 0 \quad (4\text{-}34)$$

$$\frac{\partial}{\partial t}s_R + \frac{1}{R}\frac{\partial}{\partial R}R s_R u_R + \frac{1}{R}\frac{\partial}{\partial \phi}s_R u_\phi + \frac{\partial}{\partial z}s_R u_z + \frac{\partial}{\partial R}p + \Lambda_E\frac{\partial}{\partial R}E_R \;=\; -\rho\frac{\partial}{\partial R}\Phi + \frac{l_z^2}{\rho R^3}; \quad (4\text{-}35)$$

$$\frac{\partial}{\partial t}l_z + \frac{1}{R}\frac{\partial}{\partial R}R l_z u_R + \frac{1}{R}\frac{\partial}{\partial \phi}\left(l_z u_\phi + Rp\right) + \frac{\partial}{\partial z}l_z u_z + \Lambda_E\frac{\partial}{\partial \phi}E_R \;=\; -\rho\frac{\partial}{\partial \phi}\Phi; \quad (4\text{-}36)$$

$$\frac{\partial}{\partial t}s_z + \frac{1}{R}\frac{\partial}{\partial R}R s_z u_R + \frac{1}{R}\frac{\partial}{\partial \phi}s_z u_\phi + \frac{\partial}{\partial z}\left(s_z u_z + p\right) + \Lambda_E\frac{\partial}{\partial z}E_R \;=\; -\rho\frac{\partial}{\partial z}\Phi; \quad (4\text{-}37)$$

$$\frac{\partial}{\partial t}\mathcal{E}_{\rm loc} - \rho\frac{\partial}{\partial t}\Phi + \frac{1}{R}\frac{\partial}{\partial R}R(\mathcal{E}_{\rm loc} + p)\,u_R + \frac{1}{R}\frac{\partial}{\partial \phi}(\mathcal{E}_{\rm loc} + p)\,u_\phi + \frac{\partial}{\partial z}(\mathcal{E}_{\rm loc} + p)\,u_z + \Lambda_E\left(\mathbf{u}\cdot\nabla\right)E_R \;= \\ -4\pi\kappa_p B_p + c\kappa_E E_R; \quad (4\text{-}38)$$

$$\frac{\partial}{\partial t}E_R + \frac{1}{R}\frac{\partial}{\partial R}RE_R u_R + \frac{1}{R}\frac{\partial}{\partial \phi}E_R u_\phi + \frac{\partial}{\partial z}E_R u_z + \nabla \mathbf{u} : \mathbf{P} \;=\; 4\pi\kappa_p B_p - c\kappa_E E_R - \nabla \cdot \mathbf{F}; \quad (4\text{-}39)$$

$$\frac{\partial}{\partial t}\tau + \frac{1}{R}\frac{\partial}{\partial R}R\tau u_R + \frac{1}{R}\frac{\partial}{\partial \phi}\tau u_\phi + \frac{\partial}{\partial z}\tau u_z \;=\; -\frac{4\pi\kappa_p B_p}{\gamma\tau^{\gamma-1}} + \frac{c\kappa_E E_R}{\gamma\tau^{\gamma-1}}. \quad (4\text{-}40)$$

On the LHS we have placed terms which are handled by the explicit advection scheme. The gravity terms on the RHS of equations (4-35), (4-36), and (4-37) are computed with a first-order explicit differencing scheme, as is the last term of equation (4-35). The remaining, radiation related terms on the RHS of equations (4-38), (4-39), and (4-40) are evolved in a separate implicit step.

5. Numerical Method[1]

Our method is designed to evolve six independent variables in time on a cylindrical mesh rotating with constant and uniform angular frequency Ω about the coordinate axis: the mass density, ρ, the *inertial* frame z-angular momentum density, l_z, the radial momentum density, s_R, the vertical momentum density, s_z, the gas energy density, E_G, and the radiation energy density, E_R. The Newtonian gravitational potential, Φ, is solved at each time (sub) step. We evolve a single auxiliary variable, the entropy tracer, τ.

5.1. Explicit Advection Scheme

We begin our discussion of the explicit advection scheme by applying it to equations (4-34) through (4-40) in the limit that $G = 0$, $\Omega = 0$, $\kappa_E = 0$, $\kappa_p = 0$, and $\Lambda_E = 0$. This has the effect of removing gravitational, rotational, and all radiation terms except the advection of E_R. We will denote the time derivatives of the evolution variables in this limit by prefacing them with $\lim_{\text{fluid}}$.

$$\lim_{\text{fluid}} \frac{\partial}{\partial t}\rho + \frac{1}{R}\frac{\partial}{\partial R}R\rho u_R + \frac{1}{R}\frac{\partial}{\partial \phi}\rho u_\phi + \frac{\partial}{\partial z}\rho u_z = 0; \quad (5\text{-}1)$$

$$\lim_{\text{fluid}} \frac{\partial}{\partial t}s_R + \frac{1}{R}\frac{\partial}{\partial R}Rs_R u_R + \frac{\partial}{\partial R}p + \frac{1}{R}\frac{\partial}{\partial \phi}s_R u_\phi + \frac{\partial}{\partial z}s_R u_z = \frac{l_z^2}{\rho R^3}; \quad (5\text{-}2)$$

$$\lim_{\text{fluid}} \frac{\partial}{\partial t}l_z + \frac{1}{R}\frac{\partial}{\partial R}Rl_z u_R + \frac{1}{R}\frac{\partial}{\partial \phi}\left(l_z u_\phi + Rp\right) + \frac{\partial}{\partial z}l_z u_z = 0; \quad (5\text{-}3)$$

$$\lim_{\text{fluid}} \frac{\partial}{\partial t}s_z + \frac{1}{R}\frac{\partial}{\partial R}Rs_z u_R + \frac{1}{R}\frac{\partial}{\partial \phi}s_z u_\phi + \frac{\partial}{\partial z}\left(s_z u_z + p\right) = 0; \quad (5\text{-}4)$$

$$\lim_{\text{fluid}} \frac{\partial}{\partial t}E_G + \frac{1}{R}\frac{\partial}{\partial R}R\left(E_G + p\right)u_R + \frac{1}{R}\frac{\partial}{\partial \phi}\left(E_G + p\right)u_\phi + \frac{\partial}{\partial z}\left(E_G + p\right)u_z R = 0; \quad (5\text{-}5)$$

$$\lim_{\text{fluid}} \frac{\partial}{\partial t}E_R + \frac{1}{R}\frac{\partial}{\partial R}RE_R u_R + \frac{1}{R}\frac{\partial}{\partial \phi}E_R u_\phi + \frac{\partial}{\partial z}E_R u_z = 0; \quad (5\text{-}6)$$

$$\lim_{\text{fluid}} \frac{\partial}{\partial t}\tau + \frac{1}{R}\frac{\partial}{\partial R}R\tau u_R + \frac{1}{R}\frac{\partial}{\partial \phi}\tau u_\phi + \frac{\partial}{\partial z}\tau u_z = 0. \quad (5\text{-}7)$$

Note that $\lim_{\text{fluid}} \mathcal{E}_{\text{loc}} = \lim_{\text{fluid}} E_G$.

The Kurganov-Tadmor (K-T) method (Kurganov & Tadmor (2000)), is a high resolution Godunov type central advection scheme that can be used to solve three-dimensional hyperbolic sets of first-order differential equations of the form

$$\frac{\partial}{\partial t}V + \sum_{i=1}^{3}\frac{\partial}{\partial x_i}H\left[V\right] = 0, \quad (5\text{-}8)$$

where $V = \{V_0 ... V_N\}$ is a set of N conserved quantities and $H\left[V\right] = \{H_0\left[V\right] ... H_N\left[V\right]\}$ a set of N fluxes dependent only on V. For the solution to be stable, the matrix $\partial H/\partial V$ must be hyperbolic. Like previous advection schemes such as the Lax-Friedrichs (Lax (1954), Friedrichs

[1]A substantial portion of this section and its subsections have been reproduced from Marcello & Tohline (2011) with the permission of the AAS (see Appendix D).

(1954)) and the Nessyahu-Tadmor schemes (Nessyahu & Tadmor (1990)), the K-T method does not require the use of (approximate) Riemann solvers. It is thus computationally more efficient than Riemann solver based methods. Unlike previous central schemes, the K-T method does not suffer from excessive spatial averaging of the solution, or "smearing". The K-T method can also be stated in a semi-discrete form, with discretized space and continuous time, allowing it to be coupled to a number of suitable time integration schemes.

One way to discretize the one-dimensional form of equation (5-8) is

$$V_i^{n+1} = V_i^n - \frac{\Delta t}{2\Delta x}\left[H\left(V_{i+1}^n\right) - H\left(V_{i-1}^n\right)\right]. \tag{5-9}$$

The problem is that equation (5-9) is numerically unstable. Any error present in the solution will continue to become larger and larger with each time step. The Lax-Friedrichs method solves this problem by substituting $V_i^n = \frac{1}{2}\left(V_{i+1}^n + V_{i-1}^n\right)$ to get

$$V_i^{n+1} = \frac{1}{2}\left(V_{i+1}^n + V_{i+1}^n\right) - \frac{\lambda}{2}\left[H\left(V_{i+1}^n\right) - H\left(V_{i-1}^n\right)\right], \tag{5-10}$$

where $\lambda \equiv \Delta t/\Delta x$. The resulting discretization is stable so long as the Courant - Friedrichs - Lewy condition is satisfied Courant et al. (1967). That is, $v_i\lambda < 1$ for all i, where v_i is the maximum possible signal speed at the cell i.

The problem with the Lax-Friedrichs scheme is that it is highly dissipative. The profile of discontinuities in the advected variables, such as fluid shocks, quickly becomes smeared. The reason for this can be seen by transforming the discrete equation (5-10) back into an equation of continuous functions. Subtracting Vi^n from both sides of equation (5-10), dividing through by Δt, and taking the limit as Δx and Δt goes to zero yields

$$\frac{\partial}{\partial t}V(x,t) + \frac{\partial}{\partial x}H\left[V(x,t)\right] = \nu_\alpha \frac{\partial^2}{\partial x^2}V(x,t), \tag{5-11}$$

where $\nu_\alpha = (\Delta x)^2/(2\Delta t)$. The LHS of equation (5-11) is identical to the LHS of equation (5-8), but we see that a non-zero source term now appears on the RHS. ν_α has units of kinematic viscosity so the term on RHS behaves as a viscosity. This unphysical viscosity term is what causes the Lax-Friedrich approach to be stable, but it also causes it to be extremely dissipative. The magnitude of this viscosity depends on grid spacing and time step size. Note that $\lim_{\Delta x\to 0}\nu_\alpha = 0$ and $\lim_{\Delta t\to 0}\nu_\alpha = \infty$.

The K-T method solves the problem of excess unphysical dissipation by use of what amounts to a variable ν_α. In regions of either high maximum signal speeds or discontinuities, such as shocks, ν_α is higher. In regions that are smooth and which have lower maximum signal speeds, ν_α is lower. The derivation of the K-T method is described in detail in Kurganov & Tadmor (2000). Its semi-discrete form is

$$\begin{aligned}\frac{d}{dt}V_i(t) = &-\frac{1}{2\Delta x}\left[\left(H\left(V_{i+\frac{1}{2}}^+(t)\right) + H\left(V_{i+\frac{1}{2}}^-(t)\right)\right) - \left(H\left(V_{i-\frac{1}{2}}^+(t)\right) + H\left(V_{i-\frac{1}{2}}^-(t)\right)\right)\right] \\ &+ \frac{1}{2\Delta x}\left[a_{j+\frac{1}{2}}(t)\left(V_{i+\frac{1}{2}}^+(t) - V_{i+\frac{1}{2}}^-(t)\right) - a_{j-\frac{1}{2}}(t)\left(V_{i-\frac{1}{2}}^+(t) - V_{i-\frac{1}{2}}^-(t)\right)\right]. \end{aligned} \tag{5-12}$$

This is identical to equation (4.2) from Kurganov & Tadmor (2000). The quantity $a_{j+\frac{1}{2}}$ is the maximum signal speed through the $j+\frac{1}{2}^{\text{th}}$ cell. The quantities $V_{i+\frac{1}{2}}^+$ and $V_{i+\frac{1}{2}}^-$ the reconstructed

values of V to the right and left of the cell face, respectively. To 1st order, $V^+_{i+\frac{1}{2}} = V_{i+1}$, $V^-_{i+\frac{1}{2}} = V_i$, $V^+_{i-\frac{1}{2}} = V_i$, $V^-_{i-\frac{1}{2}} = V_{i-1}$. Substituting into equation (5-12) and discretizing to 1st order in time, we obtain

$$V_i^{n+1} = V_i^n - \frac{\lambda}{2}\left[H\left(V_{i+1}^n\right) - H\left(V_{i+1}^n\right)\right] + \frac{\lambda}{2}\left[a_{i+\frac{1}{2}}(V_{j+1}^n - V_j^n) - a_{i-\frac{1}{2}}(V_j^n - V_{j-1}^n)\right]. \quad (5\text{-}13)$$

As pointed out by Kurganov & Tadmor (2000), this is equivalent to Rusanov's method (van Leer (1977)). Like equation (5-10), equation (5-13) can be transformed back into a continuous form. The result is

$$\frac{\partial}{\partial t}V(x,t) + \frac{\partial}{\partial x}H(V(x,t)) = \nu_\alpha \frac{\partial}{\partial x}\left[\frac{a(x,t)}{\lambda}\frac{\partial}{\partial x}u(x,t)\right]$$

By setting $a = \lambda$, we recover equation (5-11). Thus the 1st order Kurganov - Tadmor scheme reduces to the Lax-Friedrichs scheme when the signal speed is spatially constant and equal to λ.

Due to the use of cylindrical coordinates, equations (5-1) through (5-7) do not quite follow the form of equation (5-8). Instead these equations are of the general form

$$\lim_{\text{fluid}} \frac{\partial}{\partial t}V + \frac{1}{R}\frac{\partial}{\partial R}RH^R[V] + \frac{\partial}{\partial R}G[V] + \frac{1}{R}\frac{\partial}{\partial \phi}H^\phi[V] + \frac{\partial}{\partial z}H^z[V] \;=\; S[R,V], \quad (5\text{-}14)$$

where $S[R,V]$ refers to coordinate curvature terms that result from the application of the cylindrical divergence operator. For our particular set of equations,

$$V = \begin{bmatrix} \rho \\ s_R \\ l_z \\ s_z \\ E_G \\ E_R \\ \tau \end{bmatrix}, \; G = \begin{bmatrix} 0 \\ p \\ 0 \\ 0 \\ 0 \\ 0 \\ 0 \end{bmatrix}, \; S = \begin{bmatrix} 0 \\ \frac{l_z^2}{\rho R^3} \\ 0 \\ 0 \\ 0 \\ 0 \\ 0 \end{bmatrix},$$

$$H^R = \begin{bmatrix} \rho u_R \\ s_R u_R \\ l_z u_R \\ s_z u_R \\ (E_G + p)\, u_R \\ E_R u_R \\ \tau u_R \end{bmatrix}, \; H^\phi = \begin{bmatrix} \rho u_\phi \\ s_R u_\phi \\ l_z u_\phi + Rp \\ s_z u_\phi \\ (E_G + p)\, u_\phi \\ E_R u_\phi \\ \tau u_\phi \end{bmatrix}, \text{ and } H^z = \begin{bmatrix} \rho u_z \\ s_R u_z \\ l_z u_z \\ s_z u_z + p \\ (E_G + p)\, u_z \\ E_R u_z \\ \tau u_z \end{bmatrix}. \quad (5\text{-}15)$$

Application of the central-upwind method of Kurganov & Petrova (2001) to a two-dimensional curvilinear coordinate system is discussed in Illenseer & Duschl (2009). The K-T method differs from that of Kurganov & Petrova (2001) in that the latter is genuinely multi-dimensional: it requires reconstruction of the evolved variables at cell vertices (edges) as well at cell edges (faces). The multidimensional K-T method is simply the sum of the one-dimensional K-T method applied to each dimension. We choose the simpler method because it requires reconstruction only at six cell faces per cell, as opposed to six faces and and twelve edges, and is thus computationally simpler and more efficient. The key disadvantage is that the multi-dimensional K-T method at most delivers second-order spatial accuracy, regardless of the order of the one-dimensional reconstruction.

In order to express the K-T method in a more compact form, we define the discrete divergence operator

$$\begin{aligned}\mathcal{D}\left\{H\left[V\right]\right\}_{jkl} := \\ \frac{1}{2R_j\Delta}\left(R_{j+\frac{1}{2}}\left(H^R\left[V^+_{j+\frac{1}{2}kl}\right]+H^R\left[V^-_{j+\frac{1}{2}kl}\right]\right)-R_{j+\frac{1}{2}}\left(H^R\left[V^+_{j-\frac{1}{2}kl}\right]+H^R\left[V^-_{j-\frac{1}{2}kl}\right]\right)\right) \\ +\frac{1}{2R_j\Delta}\left(H^\phi\left[V^+_{jk+\frac{1}{2}l}\right]+H^\phi\left[V^-_{jk+\frac{1}{2}l}\right]-H^\phi\left[V^+_{jk-\frac{1}{2}l}\right]-H^\phi\left[V^-_{jk-\frac{1}{2}l}\right]\right) \\ +\frac{1}{2\Delta}\left(H^z\left[V^+_{jkl+\frac{1}{2}}\right]+H^z\left[V^-_{jkl+\frac{1}{2}}\right]-H^z\left[V^+_{jkl-\frac{1}{2}}\right]-H^z\left[V^-_{jkl-\frac{1}{2}}\right]\right) \quad (5\text{-}16)\end{aligned}$$

and the discrete viscosity operator

$$\begin{aligned}\mathcal{V}\left\{V\right\}_{jkl} := \\ \frac{1}{2R_j\Delta}\left\{R_{j+\frac{1}{2}}a_{j+\frac{1}{2}kl}\left(V^+_{j+\frac{1}{2}kl}-V^-_{j+\frac{1}{2}kl}\right)-R_{j-\frac{1}{2}}a_{j-\frac{1}{2}kl}\left(V^+_{j-\frac{1}{2}kl}-V^-_{j-\frac{1}{2}kl}\right)\right\} \\ +\frac{1}{2R_j\Delta}\left\{a_{jk+\frac{1}{2}l}\left(V^+_{jk+\frac{1}{2}l}-V^-_{jk+\frac{1}{2}l}\right)-a_{jk-\frac{1}{2}l}\left(V^+_{jk-\frac{1}{2}l}-V^-_{jk-\frac{1}{2}l}\right)\right\} \\ +\frac{1}{2\Delta}\left\{a_{jkl+\frac{1}{2}}\left(V^+_{jkl+\frac{1}{2}}-V^-_{jkl+\frac{1}{2}}\right)-a_{jkl-\frac{1}{2}}\left(V^+_{jkl-\frac{1}{2}}-V^-_{jkl-\frac{1}{2}}\right)\right\}. \quad (5\text{-}17)\end{aligned}$$

The quantity Δ is the uniform spacing between grid zones. For our particular implementation, this spacing is the same for each dimension. It is trivial to modify the above expressions for a grid where the spacing is different for each dimension. The quantities $V^\pm_{j\pm\frac{1}{2}kl}$, $V^\pm_{jk\pm\frac{1}{2}l}$, and $V^\pm_{jkl\pm\frac{1}{2}}$ are the reconstructed values of V at the faces located at $j\pm\frac{1}{2}kl$, $jk\pm\frac{1}{2}l$, and $jkl\pm\frac{1}{2}$, respectively. The superscript indicates whether the value is on the left (-) or right (+) side of the face. A value for V at each side of the cell face is required to account for discontinuities in the solution. Both of the above operators reduce to surface integrals when they are summed over a grid volume. Therefore when there is no net flow through such a surface, V is numerically conserved. The signal speeds are defined as

$$a_{j\pm\frac{1}{2}kl} := \max\left\{\lambda_{\max}\left\{\left.\frac{\partial H^R}{\partial V}\right|_{V=V^+_{j\pm\frac{1}{2}kl}}\right\},\lambda_{\max}\left\{\left.\frac{\partial H^R}{\partial V}\right|_{V=V^+_{j\pm\frac{1}{2}kl}}\right\}\right\}, \quad (5\text{-}18)$$

$$a_{jk\pm\frac{1}{2}k} := \max\left\{\lambda_{\max}\left\{\left.\frac{\partial H^\phi}{\partial V}\right|_{V=V^+_{jk\pm\frac{1}{2}k}}\right\},\lambda_{\max}\left\{\left.\frac{\partial H^\phi}{\partial V}\right|_{V=V^+_{jk\pm\frac{1}{2}k}}\right\}\right\} \quad (5\text{-}19)$$

and

$$a_{jkl\pm\frac{1}{2}} := \max\left\{\lambda_{\max}\left\{\left.\frac{\partial H^z}{\partial V}\right|_{V=V^+_{jkl\pm\frac{1}{2}}}\right\},\lambda_{\max}\left\{\left.\frac{\partial H^z}{\partial V}\right|_{V=V^+_{jkl\pm\frac{1}{2}}}\right\}\right\}, \quad (5\text{-}20)$$

where $\lambda_{\max}\left\{A\right\}$ is the spectral radius operator. For equations (5-1) through (5-7),

$$\lambda_{\max}\left\{\frac{\partial G^n}{\partial V}\right\} = |u_n| + \sqrt{\frac{\gamma p}{\rho}}, \quad (5\text{-}21)$$

where u_n refers to one of the vector components of $\mathbf{u}$. Note that for brevity we omit the dependence on signal speeds in writing $\mathcal{V}\left\{V\right\}_{jkl}$. To ensure numerical stability when using an explicit

time integrator, the Courant-Friedrichs-Lewy condition (CFL) (Courant et al. (1967)) must be satisfied for the chosen time step. For the K-T method in cylindrical coordinates, this condition is

$$\Delta t \;\leq\; \frac{1}{2}\min_{\text{all } jkl}\left\{\frac{\Delta}{a_{j\pm\frac{1}{2}kl}}, \frac{R\Delta}{a_{jk\pm\frac{1}{2}l}}, \frac{\Delta}{a_{jkl\pm\frac{1}{2}}}\right\} \tag{5-22}$$

We also define the non conservative radial component of the discrete gradient,

$$\mathcal{G}_{\mathcal{R}}\left\{G\left[V\right]\right\}_{jkl} := \frac{1}{2\Delta}\left(G\left[V^{+}_{j+\frac{1}{2}kl}\right] + G\left[V^{-}_{j+\frac{1}{2}kl}\right] - G\left[V^{+}_{j-\frac{1}{2}kl}\right] - G\left[V^{-}_{j-\frac{1}{2}kl}\right]\right). \tag{5-23}$$

The semi-discrete form of the K-T method in three-dimensional cylindrical coordinates can now be written as

$$\lim_{\text{fluid}}\frac{d}{dt}V_{jkl} + \mathrm{D}\left\{H\left[V\right]\right\}_{jkl} + \mathrm{G_R}\left\{G\left[V\right]\right\}_{jkl} - S_{jkl} \;=\; \mathcal{V}\left\{V\right\}_{jkl}. \tag{5-24}$$

Note that here, and for the remainder of this paper, $\frac{d}{dt}$ does *not* refer to the Lagrangian time derivative, $\frac{\partial}{\partial t} + \mathbf{u}\cdot\nabla$, but instead refers to the total time rate of change of the value of a grid cell. The LHS of equation (5-24) contains the numerical representation of the physical flux components and coordinate curvature terms. The terms on the RHS are, in effect, artificial viscosity terms. These unphysical terms are required for numerical stability. The magnitude of the viscosity grows larger with increasing maximum signal speed as well as with increasing difference between the values of V at left and right sides of cell faces. When the values of V are identical on both sides of a cell face, the viscosity term at that face becomes zero.

We use the one-dimensional piecewise parabolic (PPM) reconstruction of Colella & Woodward (1984) to compute the cell face values $V^{\pm}_{j\pm\frac{1}{2}kl}$, $V^{\pm}_{jk\pm\frac{1}{2}l}$, and $V^{\pm}_{jkl\pm\frac{1}{2}}$. Although the reconstruction is third order in one dimension, because we do not use a genuinely multidimensional method, the reconstruction reduces to second-order accuracy. However, we still retain another advantage of using a high order reconstruction: in sufficiently smooth regions, left and right face values will be exactly equal to one another, completely eliminating the artificial viscosity. In Figure 5.1 we compare the PPM reconstruction to the ubiquitous minmod linear reconstruction. For PPM, the left and right face values differ only at the two extrema and at the discontinuity, whereas the minmod reconstruction has unequal face values at numerous locations. Rather than applying the reconstruction to the conserved variables, as in Kurganov & Tadmor (2000), we apply the reconstruction to the variables ρ, $\frac{s_R}{\rho}$, $\frac{s_z}{\rho}$, $\frac{l_z}{\rho}$, $\frac{\tau}{\rho}$, $\frac{E_G}{\rho}$, and $\frac{E_R}{\rho}$, and then transform these quantities back to the conserved variables. Reconstructing face values in this manner has two advantages: (1) the velocity values obtained at cell faces transform correctly under a Galilean transformation and (2) the magnitude of the sound speed and velocity at cell faces will not exceed their respective values at cell centers.

As mentioned above, we evolve the entropy tracer, τ, independently of E_G. When the internal energy is a small fraction of E_G, the expression

$$e = \left(E_G - \frac{1}{2}\rho u^2\right) \tag{5-25}$$

can suffer from numerical difficulties. If the minuend and subtrahend of a difference are nearly equal, the result can lose significant numerical precision when determined by a computer. To account for this, we use the dual energy formalism of Bryan et al. (1995). The pressure is

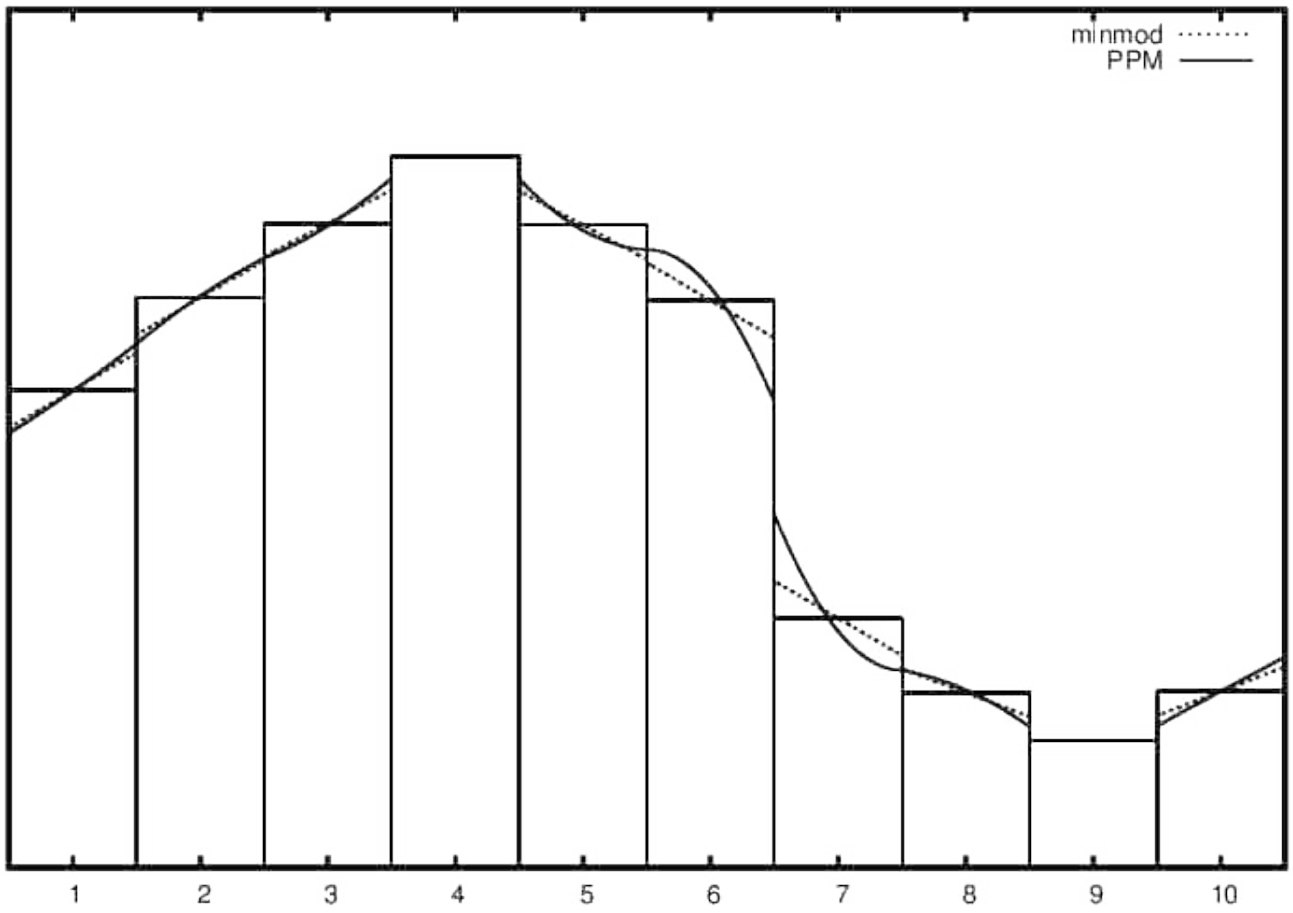

Fig. 5.1.— Comparison of minmod to PPM reconstruction schemes. The PPM reconstruction has unequal face values (resulting in artificial viscosity) only at the faces of the two extrema (the fourth and ninth cells from the left) and at the face of the discontinuity (between the sixth and seventh cells from the left). The minmod reconstruction has unequal face values at numerous other locations and the difference in face values is larger than PPM for all faces.

computed according to

$$p = \begin{cases} (\gamma - 1)\left(E_G - \frac{1}{2}\rho u^2\right) & \text{if } \left(E_G - \frac{1}{2}\rho u^2\right) > \epsilon_1 E_G \\ (\gamma - 1)\,\tau^\gamma & \text{else} \end{cases} , \tag{5-26}$$

where $0 < \epsilon_1 \ll 1$. Additionally, at the end of each computational time step, the entropy tracer is updated according to

$$\tau \rightarrow \begin{cases} \left(E_G - \frac{1}{2}\rho u^2\right)^{\frac{1}{\gamma}} & \text{if } \left(E_G - \frac{1}{2}\rho u^2\right) > \epsilon_2 E_G \\ \tau & \text{else} \end{cases} , \tag{5-27}$$

where $0 < \epsilon_1 < \epsilon_2 \ll 1$. For the simulations discussed in this paper we use $\epsilon_1 = 0.001$ and $\epsilon_2 = 0.1$.

5.2. Extension to Gravity

We now extend the K-T method in cylindrical coordinates to include a potential formed by Newtonian gravitation and/or rotation. We take equations (4-34) through (4-40) in the limit that $\kappa_E = 0$, $\kappa_p = 0$, and $\Lambda_E = 0$. We refer to this limit by prefacing time derivatives with $\lim_{\text{grav}}$.

$$\lim_{\text{grav}} \frac{\partial}{\partial t}\rho + \frac{1}{R}\frac{\partial}{\partial R}R\rho u_R + \frac{1}{R}\frac{\partial}{\partial \phi}\rho u_\phi + \frac{\partial}{\partial z}\rho u_z \;=\; 0; \tag{5-28}$$

$$\lim_{\text{grav}} \frac{\partial}{\partial t}s_R + \frac{1}{R}\frac{\partial}{\partial R}Rs_R u_R + \frac{\partial}{\partial R}p + \frac{1}{R}\frac{\partial}{\partial \phi}s_R u_\phi + \frac{\partial}{\partial z}s_R u_z \;=\; -\rho\frac{\partial}{\partial R}\Phi + \frac{l_z^2}{\rho R^3}; \tag{5-29}$$

$$\lim_{\text{grav}} \frac{\partial}{\partial t}l_z + \frac{1}{R}\frac{\partial}{\partial R}Rl_z u_R + \frac{1}{R}\frac{\partial}{\partial \phi}\left(l_z u_\phi + Rp\right) + \frac{\partial}{\partial z}l_z u_z \;=\; -\rho\frac{\partial}{\partial \phi}\Phi; \tag{5-30}$$

$$\lim_{\text{grav}} \frac{\partial}{\partial t}s_z + \frac{1}{R}\frac{\partial}{\partial R}Rs_z u_R + \frac{1}{R}\frac{\partial}{\partial \phi}s_z u_\phi + \frac{\partial}{\partial z}\left(s_z u_z + p\right) \;=\; -\rho\frac{\partial}{\partial z}\Phi; \tag{5-31}$$

$$\lim_{\text{grav}} \frac{\partial}{\partial t}\mathcal{E}_{\text{loc}} - \rho\frac{\partial}{\partial t}\Phi + \frac{1}{R}\frac{\partial}{\partial R}R\left(\mathcal{E}_{\text{loc}} + p\right)u_R + \frac{1}{R}\frac{\partial}{\partial \phi}\left(\mathcal{E}_{\text{loc}} + p\right)u_\phi + \frac{\partial}{\partial z}\left(\mathcal{E}_{\text{loc}} + p\right)u_z \;=\; 0; \tag{5-32}$$

$$\lim_{\text{grav}} \frac{\partial}{\partial t}E_R + \frac{1}{R}\frac{\partial}{\partial R}RE_R u_R + \frac{1}{R}\frac{\partial}{\partial \phi}E_R u_\phi + \frac{\partial}{\partial z}E_R u_z \;=\; 0; \tag{5-33}$$

$$\lim_{\text{grav}} \frac{\partial}{\partial t}\tau + \frac{1}{R}\frac{\partial}{\partial R}R\tau u_R + \frac{1}{R}\frac{\partial}{\partial \phi}\tau u_\phi + \frac{\partial}{\partial z}\tau u_z \;=\; 0. \tag{5-34}$$

To solve equation (4-5) for the gravitational potential, Φ, we solve the discrete equation

$$R_{j+\frac{1}{2}}\Phi_{j+1kl} + R_{j-\frac{1}{2}}\Phi_{j-1kl} + \Phi_{jk+1l} + \Phi_{jk-1l} + R_j\Phi_{jkl+1} + R_j\Phi_{jkl-1} - \left(4R_j + 2\right)\Phi_{jkl} \;=\; 4\pi G R_j \Delta^2 \rho, \tag{5-35}$$

using a conjugate gradient solver for the interior (Hestenes (1952)). The boundary cell values for Φ are computed using the solver of Cohl & Tohline (1999).

Equation (5-32) differs from equation (5-5) only in the addition of an extra time derivative term, $\rho\frac{\partial}{\partial t}\Phi$, and the use of $\mathcal{E}_{\text{loc}}$ in place of E_G. The semi-discrete form of this equation is

$$\lim_{\text{grav}} \frac{d}{dt}\mathcal{E}_{\text{loc},jkl} - \rho_{jkl}\frac{d}{dt}\Phi_{jkl} + \mathcal{D}\left\{\left(\mathcal{E}_{\text{loc}} + p\right)\mathbf{u}\right\}_{jkl} \;=\; \mathcal{V}\left\{\mathcal{E}_{\text{loc}}\right\}_{jkl}. \tag{5-36}$$

Because time is continuous in the semi-discrete form, we may use equation (4-25) to rewrite equation (5-36) as

$$\lim_{\text{grav}} \frac{d}{dt}E_{G,jkl} + \mathcal{D}\left\{\left(\mathcal{E}_{\text{loc}} + p\right)\mathbf{u}\right\}_{jkl} - \left[\Phi_{\text{eff}}\right]_{jkl}\frac{d}{dt}\rho_{jkl} \;=\; \mathcal{V}\left\{\mathcal{E}_{\text{loc}}\right\}_{jkl}. \tag{5-37}$$

where $\Phi_{\text{eff}} := \Phi + \Phi_{\text{rot}}$ is the "effective potential". Note that the term $\frac{d}{dt}\rho_{jkl}$ is obtained by applying equation (5-24) to equation (5-28). The quantity $\mathcal{E}_{\text{con}}$ will be nearly globally conserved under application of equation (5-37). To prove this, we rewrite equation (5-36) as

$$\lim_{\text{grav}} \frac{d}{dt}\mathcal{E}_{\text{con},jkl} + \frac{1}{2}\left(\rho_{jkl}\frac{d}{dt}\Phi_{jkl} - \Phi_{jkl}\frac{d}{dt}\rho_{jkl}\right) + \mathcal{D}\left\{\left(\mathcal{E}_{\text{loc}} + p\right)\mathbf{u}\right\}_{jkl} \;=\; \mathcal{V}\left\{\mathcal{E}_{\text{loc}}\right\}_{jkl}. \tag{5-38}$$

The discrete divergence and viscosity operators are conservative. Using equation (5-35), we can rewrite the sum over volume of the middle term on the LHS,

$$\sum_{jkl} \frac{1}{2} \left(\rho_{jkl} \frac{d}{dt} \Phi_{jkl} - \Phi_{jkl} \frac{d}{dt} \rho_{jkl} \right) R_j \Delta^3 = \frac{\Delta}{8\pi G} \sum_{jkl} \Big\{ \Big(R_{j+\frac{1}{2}} \dot{\Phi}_{j+1kl} + R_{j-\frac{1}{2}} \dot{\Phi}_{j-1kl} + \dot{\Phi}_{jk+1l} + \dot{\Phi}_{jk-1l} - R_j \left(\dot{\Phi}_{jkl+1} + \dot{\Phi}_{jkl-1} \right) - (4R_j + 2) \dot{\Phi}_{jkl} \Big) \Phi_{jkl} - \Big[R_{j-\frac{1}{2}} \Phi_{j-1kl} + R_{j+\frac{1}{2}} \Phi_{j+1kl} + \Phi_{jk-1l} + \Phi_{jk+1l} + R_j \left(\Phi_{jkl-1} + \Phi_{jkl+1} \right) - (4R_j + 2) \Phi_{jkl} \Big] \dot{\Phi}_{jkl} \Big\}, \quad (5\text{-}39)$$

where $\dot{\Phi}_{jkl} := \frac{d}{dt} \Phi_{jkl}$. Expression (5-39) sums to zero for interior grid points, depending only on the values of Φ_{jkl} and $\dot{\Phi}_{jkl}$ along a two-cell-wide boundary at the surface of the computational grid. To be physically correct, these terms must also sum to zero (so long as there is no mass leaving the grid), however, this is not numerically guaranteed. The extent to which equation (5-35) is numerically satisfied will also affect conservation. As shown below, these non-conservative effects are minimized when the center of mass of the system is coincident with the center of the coordinate system.

The application of the viscosity operator, $\mathcal{V}\{V\}_{jkl}$, to the mass density, ρ, for any cell in which left and right face values are unequal (non-smooth regions), results in the flow of mass from cells of higher density to cells of lower density. In the absence of a potential, this will not alter energy conservation. When a potential force is applied, however, this non-physical movement of mass will violate energy conservation unless it is properly accounted for. To illustrate this effect, consider the one-dimensional PPM reconstruction of an equilibrium $n = \frac{3}{2}$ polytrope in Figure (5.2). Even with the PPM reconstruction, there are discontinuities in the reconstruction of ρ at the faces of the center cell and at the outer cells. Application of the the K-T method will therefore cause mass to move up the gravitational potential, from the center cell to the surrounding cells and from the cells just below the surface cells of the star to the surface cells. If not properly accounted for, this added potential energy comes at no cost to either the kinetic energy or the internal gas energy of the fluid and $\mathcal{E}_{\rm con}$ will not be conserved. For models of gravitationally bound objects in near equilibrium, this effect will accumulate over time, and the object can become gravitationally unbound and dissipate. Equation (5-37) accounts for this spontaneous potential energy generation by removing it from the total gas energy. Because we do not alter how the kinetic energy is calculated, the difference is effectively removed from the internal energy. Matter which moves up (down) a potential by application of the viscosity operator will lose (gain) internal energy. This presents a problem for a zero temperature fluid. With no internal energy to lose, application of equation (5-37) will result in values for E_G which yield negative internal energies under application of equation (5-25). Regions with non-positive pressure have nothing to prevent them from collapsing due to their own gravity, leading to numerically unstable conditions. We avoid this issue by using the dual energy formalism, which guarantees a positive pressure so long as τ is positive.

There are two applications of the viscosity operator resulting from the potential energy in equation (5-37). The $\frac{d}{dt}\rho_{jkl}$ term contains $\mathcal{V}\{\rho\}_{jkl}$. It is this term that cancels the spontaneous gains or losses in potential energy. The second source is the contribution from the potential energy to $\mathcal{V}\{\mathcal{E}_{\rm loc}\}_{jkl}$. This term causes the correction in energy due to $\frac{d}{dt}\rho_{jkl}$ to flow with the fluid. Without it, this correction would be applied to the cell the fluid is flowing out of instead of to the cell into which it is flowing. We refer to these extra viscosity terms in the energy

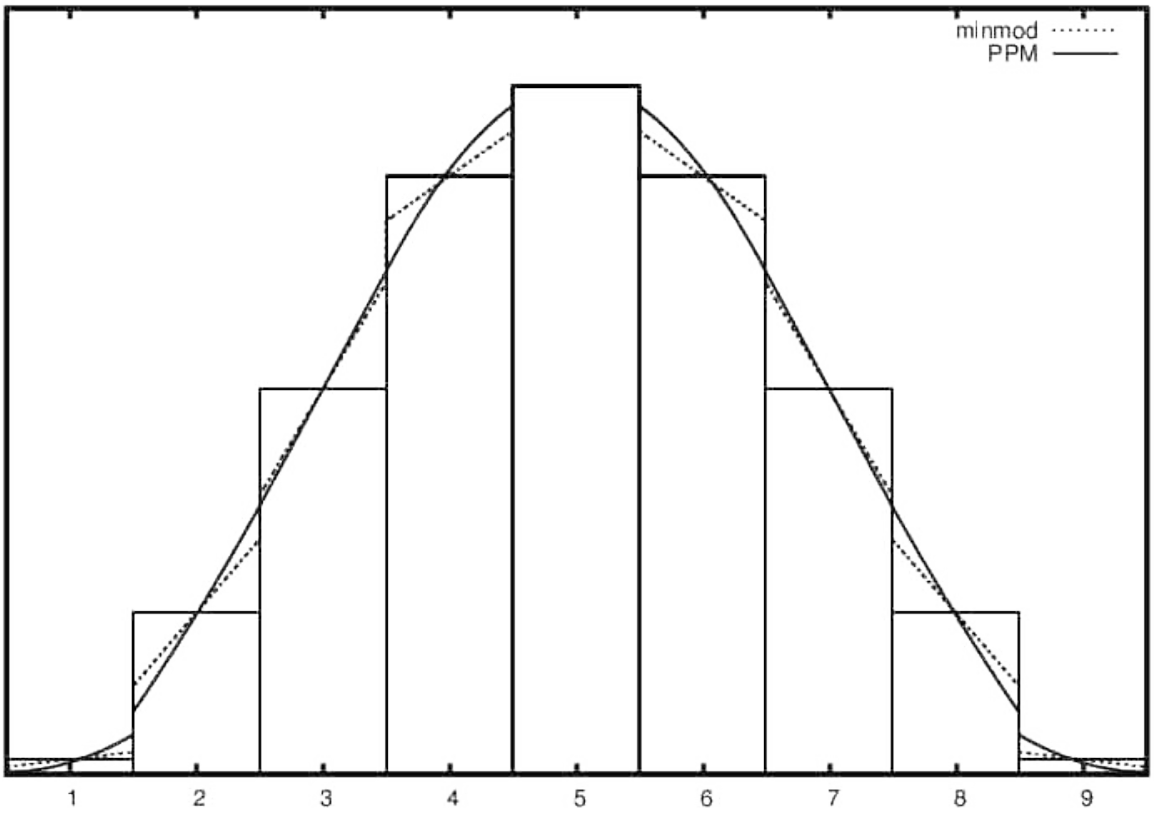

Fig. 5.2.— PPM reconstruction of a polytrope. In this one-dimensional PPM reconstruction of the mass density of an $n = \frac{3}{2}$ polytrope, there are discontinuities in the reconstruction at the center and near the surface. Artificial viscosity will be applied to the cells next to these discontinuities. As a result, mass will move from the center cell to the two cells next to it, and from the second (eighth) cell to the first (ninth) cell.

equation as the "E*" correction. Appendix B outlines two additional methods of treating the energy equation. These methods are compared to the "E*" correction in some of the verification problems presented below.

Equations (5-29), (5-30), and (5-31) differ from equations (5-2), (5-3), and (5-4) in that they each contain a gravitational term on the RHS. We require that l_z and s_z be nearly conserved, therefore the numerical form of these terms for equations (5-30) and (5-31) must be numerically conservative. This can be accomplished using second-order differencing for $\nabla\Phi$ and the cell-centered values of ρ. The resulting equations for l_z and s_z are, respectively,

$$\lim_{\text{grav}} \frac{d}{dt} l_z + \mathcal{D}\left\{ l_z + \mathbf{u} + p\hat{\phi} \right\}_{jkl} + \rho_{jkl} \frac{1}{2\Delta} \left(\Phi_{jk+1l} - \Phi_{jk-1l} \right) \;=\; \mathcal{V}\left\{ l_z \right\}_{jkl} \tag{5-40}$$

and

$$\lim_{\text{grav}} \frac{d}{dt} s_z + \mathcal{D}\left\{ s_z \mathbf{u} + p\hat{\mathbf{z}} \right\}_{jkl} + \rho_{jkl} \frac{1}{2\Delta} \left(\Phi_{jkl-1} - \Phi_{jkl-1} \right) \;=\; \mathcal{V}\left\{ s_z \right\}_{jkl} . \tag{5-41}$$

Just as with the total energy equation, by using equation (5-35) to remove ρ_{jkl} from the gravitational terms, it is possible to show that equations (5-40) and (5-41) nearly conserve angular and vertical momentum over the interior of the computational grid. There is a similar non-conservative effect from the limited precision of the Poisson solver and numerical boundary

conditions. Using the same second-order differencing, the radial momentum equation is

$$\lim_{\text{grav}} \frac{d}{dt} s_R + \mathcal{D}\left\{s_R \mathbf{u}\right\}_{jkl} + \mathcal{G}_{\mathcal{R}}\left\{p\right\}_{jkl} + \rho_{jkl} \frac{1}{2\Delta}\left(\Phi_{j+1kl} - \Phi_{j-1kl}\right) - \frac{l_{z,jkl}^2}{\rho_{jkl} R_j^3} \;=\; \mathcal{V}\left\{s_R\right\}_{jkl}. \quad (5\text{-}42)$$

Without the addition of gravity, the one-dimensional Kurganov-Tadmor method will satisfy the maximum principle. Positive scalars at $t = 0$ remain positive throughout the evolution. With multiple dimensions, it is also possible to satisfy the maximum principle by using a small enough time-step (see §5 of Kurganov & Tadmor (2000)). The addition of gravity complicates matters, however, and we have not found a general method to guarantee that positive scalars remain positive without using overly small time-steps. There are four evolved quantities which are physically expected to be positive: the mass density, ρ; the entropy tracer, τ; the radiation energy density, E_R; and the total gas energy density, E_G. We adopt "floor" values for the first three of these quantities. At the beginning of each time sub-step and for each grid cell, ρ, τ, and E_R are all set to the maximum of themselves or a predefined floor value. The total gas energy, E_G, is not altered. When it is negative, the dual energy formalism will use τ to determine the internal energy. The floor values we use are simulation dependent. Gravity also has the potential to complicate the CFL requirement. For our particular purposes, we have found this to only be a problem during the initial stages of the evolution. Our simulations generally begin with zero or near-zero velocities. If the time-step is limited to only the CFL time-step limit, velocities (especially in low density regions) can grow very large within the first time-step, leading to immediate numerical instability. For our evolutions with gravity, we begin the evolution with a time-step size that has empirically been shown to not lead to immediate instability. Then we gradually increase the time-step size over the next several hundred time-steps, until it is equal to the maximum imposed by the CFL condition.

5.3. Radiation Transport - Explicit Step

In a manner similar to Krumholz et al. (2007), we take equations (4-34) through (4-40) and split them into explicit and implicit parts,

$$\frac{\partial}{\partial t} V + \mathbf{q}_{\text{explicit}} = \mathbf{q}_{\text{implicit}}, \quad (5\text{-}43)$$

where

$\mathbf{q}_{\text{explicit}} =$

$$\left[\begin{array}{l}
\frac{1}{R}\frac{\partial}{\partial R} R\rho u_R + \frac{1}{R}\frac{\partial}{\partial \phi}\rho u_\phi + \frac{\partial}{\partial z}\rho u_z \\
\frac{1}{R}\frac{\partial}{\partial R} R s_R u_R + \frac{\partial}{\partial R} p + \frac{1}{R}\frac{\partial}{\partial \phi} s_R u_\phi + \frac{\partial}{\partial z} s_R u_z + \Lambda_E \frac{\partial}{\partial R} E_R + \rho \frac{\partial}{\partial R}\Phi - \frac{l_z^2}{\rho R^3} \\
\frac{1}{R}\frac{\partial}{\partial R} R l_z u_R + \frac{1}{R}\frac{\partial}{\partial \phi}\left(l_z u_\phi + Rp\right) + \frac{\partial}{\partial z} l_z u_z + \Lambda_E \frac{\partial}{\partial \phi} E_R + \rho \frac{\partial}{\partial \phi}\Phi \\
\frac{1}{R}\frac{\partial}{\partial R} R s_z u_R + \frac{1}{R}\frac{\partial}{\partial \phi} s_z u_\phi + \frac{\partial}{\partial z}\left(s_z u_z + p\right) + \Lambda_E \frac{\partial}{\partial z} E_R + \rho \frac{\partial}{\partial z}\Phi \\
\frac{1}{R}\frac{\partial}{\partial R} R\left(\mathcal{E}_{\text{loc}} + p\right) u_R + \frac{1}{R}\frac{\partial}{\partial \phi}\left(\mathcal{E}_{\text{loc}} + p\right) u_\phi + \frac{\partial}{\partial z}\left(\mathcal{E}_{\text{loc}} + p\right) u_z + \Lambda_E \left(\mathbf{u}\cdot\nabla\right) E_R - \rho \frac{\partial}{\partial t}\Phi \\
\frac{1}{R}\frac{\partial}{\partial R} R E_R u_R + \frac{1}{R}\frac{\partial}{\partial \phi} E_R u_\phi + \frac{\partial}{\partial z} E_R u_z + \nabla \mathbf{u} : \mathbf{P} \\
\frac{1}{R}\frac{\partial}{\partial R} R\tau u_R + \frac{1}{R}\frac{\partial}{\partial \phi}\tau u_\phi + \frac{\partial}{\partial z}\tau u_z
\end{array}\right], \quad (5\text{-}44)$$

and

$$\mathbf{q}_{\text{implicit}} = \begin{bmatrix} 0 \\ 0 \\ 0 \\ 0 \\ -4\pi\kappa_p B_p + c\kappa_E E_R \\ -\nabla\cdot\mathbf{F} + 4\pi\kappa_p B_p - c\kappa_E E_R \\ \frac{1}{\gamma\tau^{\gamma-1}}\left(-4\pi\kappa_p B_p + c\kappa_E E_R\right) \end{bmatrix}. \tag{5-45}$$

The expression $\mathbf{q}_{\text{explicit}}$ contains the terms in the $\lim_{\text{grav}}$ case described in §5.2, as well as $\Lambda_E \nabla E_R$ terms in the momentum equations, the $\Lambda_E \mathbf{u}\cdot\nabla E_R$ term in the total gas energy equation, and the $\mathbf{P}:\nabla\mathbf{u}$ term in the radiation energy equation. These terms are calculated using cell-centered quantities, V_{ijk}, and the first-order differences,

$$\frac{1}{2}\left(\left(V^-_{j+\frac{1}{2}kl} + V^+_{j+\frac{1}{2}jk}\right) - \left(V^-_{j-\frac{1}{2}jk} + V^+_{j-\frac{1}{2}kl}\right)\right), \tag{5-46}$$

for derivatives in the radial direction,

$$\frac{1}{2}\left(\left(V^-_{jk+\frac{1}{2}l} + V^+_{jk+\frac{1}{2}l}\right) - \left(V^-_{jk-\frac{1}{2}l} + V^+_{jk-\frac{1}{2}l}\right)\right), \tag{5-47}$$

for derivatives in the azimuthal direction, and

$$\frac{1}{2}\left(\left(V^-_{jkl+\frac{1}{2}} + V^+_{jkl+\frac{1}{2}}\right) - \left(V^-_{jkl-\frac{1}{2}} + V^+_{jkl-\frac{1}{2}}\right)\right), \tag{5-48}$$

for derivatives in the vertical direction. With radiation, the characteristic speeds are calculated using

$$a_i = |u_i| + \sqrt{\frac{\gamma p + (f_{ii}+1)\,\Lambda_E E_R}{\rho}}. \tag{5-49}$$

The subscripts for a, u, and f refer to the i^{th} vector and ii^{th} tensor component of those quantities. This equation is exact in the diffusion limit, where $f_{ii} \to \frac{1}{3}$ and $\Lambda_E \to \frac{1}{3}$. In the free-streaming limit, equation (5-49) is only an approximation. It was chosen so that as Λ_E goes to zero, the contribution of radiation to the sound speed also goes to zero.

To compute the explicit step, we solve equation (5-43) with $\mathbf{q}_{\text{implicit}}$ set to zero. The solution is computed this way over all time sub-steps of the integration. The set of semi-discrete equations is:

$$\frac{d}{dt}\rho + \mathcal{D}\left\{\rho\mathbf{u}\right\}_{jkl} \;=\; \mathcal{V}\left\{\rho\right\}_{jkl}; \tag{5-50}$$

$$\frac{d}{dt}s_R + \mathcal{D}\left\{s_R\mathbf{u}\right\}_{jkl} + \mathcal{G}_{\mathcal{R}}\left\{p\right\}_{jkl} + \rho_{jkl}\frac{1}{2\Delta}\left(\Phi_{j+1kl} - \Phi_{j+1kl}\right) + \\ + \Lambda_{jkl}\frac{1}{\Delta}\left(E_{R,j+\frac{1}{2}kl} - E_{R,j-\frac{1}{2}kl}\right) - \frac{l^2_{z,jkl}}{\rho_{jkl}R^3_j} \;=\; \mathcal{V}\left\{s_R\right\}_{jkl}; \tag{5-51}$$

$$\frac{d}{dt}l_z + \mathcal{D}\left\{l_z\mathbf{u}\mathbf{u} + p\hat{\phi}\right\}_{jkl} + \rho_{jkl}\frac{1}{2\Delta}\left(\Phi_{jk+1l} - \Phi_{jk-1l}\right) + \\ + \Lambda_{jkl}\frac{1}{\Delta}\left(E_{R,jk+\frac{1}{2}l} - E_{R,jk-\frac{1}{2}l}\right) \;=\; \mathcal{V}\left\{l_z\right\}_{jkl}; \tag{5-52}$$

$$\frac{d}{dt}s_z + \mathcal{D}\left\{s_z\mathbf{u}\mathbf{u} + p\hat{\mathbf{z}}\right\}_{jkl} + \rho_{jkl}\frac{1}{2\Delta}\left(\Phi_{jkl+1} - \Phi_{jkl-1}\right) + \\ + \Lambda_{jkl}\frac{1}{\Delta}\left(E_{R,jkl+\frac{1}{2}} - E_{R,jkl-\frac{1}{2}}\right) \;=\; \mathcal{V}\left\{s_z\right\}_{jkl}; \quad (5\text{-}53)$$

$$\frac{d}{dt}E_{G,jkl} + \mathcal{D}\left\{\left(\mathcal{E}_{\rm loc} + p\right)\mathbf{u}\right\}_{jkl} - \Phi_{{\rm eff},jkl}\frac{d}{dt}\rho_{jkl} + u_{R,jkl}\Lambda_{jkl}\frac{1}{\Delta}\left(E_{R,jkl+\frac{1}{2}} - E_{R,jlk-\frac{1}{2}}\right) + \\ \frac{u_{\phi,jkl}}{R}\Lambda_{jkl}\frac{1}{\Delta}\left(E_{R,jk+\frac{1}{2}l} - E_{R,jk-\frac{1}{2}l}\right) + u_{z,jkl}\Lambda_{jkl}\frac{1}{\Delta}\left(E_{R,j+\frac{1}{2}kl} - E_{R,j-\frac{1}{2}kl}\right) \;=\; \mathcal{V}\left\{\mathcal{E}_{\rm loc}\right\}_{jkl}; \quad (5\text{-}54)$$

$$\frac{d}{dt}E_{R,jkl} + \mathcal{D}\left\{E_R\mathbf{u}\right\}_{jkl} + \\ P_{RR,jkl}\frac{1}{\Delta}\left(u_{R,j+\frac{1}{2}kl} - u_{R,j-\frac{1}{2}kl}\right) + P_{R\phi,jkl}\frac{1}{\Delta}\left(u_{\phi,j+\frac{1}{2}kl} - u_{\phi,j-\frac{1}{2}kl}\right) + \\ P_{Rz,jkl}\frac{1}{\Delta}\left(u_{z,j+\frac{1}{2}kl} - u_{z,j-\frac{1}{2}kl}\right) + P_{\phi R,jkl}\frac{1}{\Delta}\left(u_{R,jkl+\frac{1}{2}} - u_{R,jkl-\frac{1}{2}}\right) + \\ P_{\phi\phi,jkl}\frac{1}{\Delta}\left(u_{\phi,jkl+\frac{1}{2}} - u_{\phi,jkl-\frac{1}{2}}\right) + P_{\phi z,jkl}\frac{1}{\Delta}\left(u_{z,jkl+\frac{1}{2}} - u_{z,jkl-\frac{1}{2}}\right) + \\ P_{zR,jkl}\frac{1}{\Delta}\left(u_{R,jk+\frac{1}{2}l} - u_{R,jk-\frac{1}{2}l}\right) + P_{z\phi,jkl}\frac{1}{\Delta}\left(u_{\phi,jk+\frac{1}{2}l} - u_{\phi,jk-\frac{1}{2}l}\right) + \\ P_{zz,jkl}\frac{1}{\Delta}\left(u_{z,jk+\frac{1}{2}l} - u_{R,jk-\frac{1}{2}l}\right) \;=\; \mathcal{V}\left\{E_R\right\}_{jkl}; \quad (5\text{-}55)$$

$$\frac{d}{dt}\tau + \mathcal{D}\left\{\tau\mathbf{u}\right\}_{jkl} \;=\; \mathcal{V}\left\{\tau\right\}_{jkl}. \quad (5\text{-}56)$$

The average of the left- and right-face quantities is $V_{j+\frac{1}{2}kl} := \frac{1}{2}\left(V^+_{j+\frac{1}{2}kl} + V^-_{j+\frac{1}{2}kl}\right)$. Equations (5-50) through (5-56) are transformed into fully discrete form by using the third-order Runge Kutta (RK) time integrator of Shu & Osher (1988). After the RK update is performed, the evolution variables are in a state between the last, $n^{\rm th}$, and the next, $n+1^{\rm th}$, time-step. We refer to this as the $n + a^{\rm th}$ time step.

5.4. Radiation - Implicit Update

We solve for the implicit terms by taking equation (5-43) with $\mathbf{q}_{\rm explicit}$ set to zero. The resulting equation set is

$$\lim_{\rm imp}\frac{\partial}{\partial t}E_G = -4\kappa_p B_p + c\kappa_E E_R, \quad (5\text{-}57)$$

$$\lim_{\rm imp}\frac{\partial}{\partial t}E_R + \nabla\cdot\mathbf{F} = 4\kappa_p B_p - c\kappa_E E_R, \quad (5\text{-}58)$$

and

$$\lim_{\rm imp}\frac{\partial}{\partial t}\tau = \frac{1}{\gamma\tau^{(\gamma-1)}}\left(-4\kappa_p B_p + c\kappa_E E_R\right). \quad (5\text{-}59)$$

The implicit step is computed as if there are no contributions from explicit terms over an entire time-step. We have applied the prefix $\lim_{\rm imp}$ to indicate that we are referring only to the time variance of these quantities due to the implicit terms. Since the fluid momentum does not

change due to implicit terms, $\lim_{\text{imp}} \frac{\partial}{\partial t} E_G = \lim_{\text{imp}} \frac{\partial}{\partial t} e$, and using $e := \tau^\gamma$, we can eliminate equation (5-59) and solve only equations (5-59) and (5-57). We compute the solution to these equations using a backward Euler time step and first-order spatial differencing. The fully discrete equations are:

$$E^{n+1}_{R,jkl} - E^{n+a}_{R,jkl} - \Delta t \left(4\kappa^{n+1}_{p,jkl} B^{n+1}_{p,jkl} - c\kappa^{n+1}_{E,jkl} E^{n+1}_{R,jkl} - [\nabla \cdot \mathbf{F}]^{n+1}_{jkl} \right) = 0 \tag{5-60}$$

and

$$E^{n+1}_{G,jkl} - E^{n+a}_{G,jkl} + \Delta t \left(4\kappa^{n+1}_{p,jkl} B^{n+1}_{p,jkl} - c\kappa^{n+1}_{E,jkl} E^{n+1}_{R,jkl} \right) = 0, \tag{5-61}$$

The term $[\nabla \cdot \mathbf{F}]^{n+1}_{jkl}$ is defined as

$$\begin{aligned}
&[\nabla \cdot \mathbf{F}]^{n+1}_{jkl} := \\
&\tfrac{1}{R_i \Delta^2} \left[R_{i+\frac{1}{2}} D^{n+a}_{i+\frac{1}{2}jk} \left(E^{n+1}_{R,i+1jk} - E^{n+1}_{R,ijk} \right) - R_{i-\frac{1}{2}} D^{n+a}_{i-\frac{1}{2}jk} \left(E^{n+1}_{R,ijk} - E^{n+1}_{R,i-1jk} \right) \right] + \\
&\tfrac{1}{R_i^2 \Delta^2} \left[D^{n+a}_{ij+\frac{1}{2}k} \left(E^{n+1}_{R,ij+1k} - E^{n+1}_{R,ijk} \right) - D^{n+a}_{ij-\frac{1}{2}k} \left(E^{n+1}_{R,ijk} - E^{n+1}_{R,ij-1k} \right) \right] + \\
&\tfrac{1}{\Delta^2} \left[D^{n+a}_{ijk+\frac{1}{2}} \left(E^{n+1}_{R,ijk+1} - E^{n+1}_{R,ijk} \right) - D^{n+a}_{ijk-\frac{1}{2}} \left(E^{n+1}_{R,ijk} - E^{n+1}_{R,ijk-1} \right) \right],
\end{aligned} \tag{5-62}$$

where

$$D^{n+a}_{j\pm\frac{1}{2}kl} = \frac{c\Lambda^{n+a}_{E,j\pm\frac{1}{2}kl}}{\chi^{n+a}_{j\pm\frac{1}{2}kl}}, \tag{5-63}$$

$$D^{n+a}_{jk\pm\frac{1}{2}l} = \frac{c\Lambda^{n+a}_{E,jk\pm\frac{1}{2}l}}{\chi^{n+a}_{jk\pm\frac{1}{2}l}}, \tag{5-64}$$

and

$$D^{n+a}_{jkl\pm\frac{1}{2}} = \frac{c\Lambda^{n+a}_{E,jkl\pm\frac{1}{2}}}{\chi^{n+a}_{jkl\pm\frac{1}{2}}}. \tag{5-65}$$

We compute the Λ_E's and χ's using the cell averaged quantities and the first-order differences in equations (5-46) through (5-48). As in Hayes et al. (2006), we obtain the numerical solution to the nonlinear equations (5-60) and (5-61) with a linear iterative solver coupled to a Newton-Raphson solver. Unlike Hayes et al. (2006), our method has fewer implicit terms to compute. Krumholz et al. (2007) argue it is only necessary to implicitly compute the terms found in equations (5-58) and (5-57). Explicit gas pressure terms also fit more easily into the framework of the K-T method.

5.5. Implementation

Our method is implemented in FORTRAN-90 with the Message Passing Interface (MPI) standard for execution on high performance computing clusters. We have relied heavily on the Hyper Adaptive Mesh Refinement (AMR) Driver (HAD) of Liebling (2002), which we have modified to suite our particular needs. At the time of this writing, we have not yet implemented the AMR feature in our code.

6. Verification Testing[1]

Here we present the results of tests that have been used to verify the accuracy of our new code. We test the Poisson solver with a sphere of constant density. As a test of basic hydrodynamics, we simulate a Sod shock tube. To test the radiation diffusion solver we use the Marshak problem. We have also devised an analytic problem in the diffusion limit whereby an initial sinusoidal radiation energy profile moving with the fluid at constant velocity decays due to diffusion and absorption. To test the FLD solver in the free-streaming limit we evolve an initial step function in radiation energy density. To verify that the radiation energy is properly coupled to the fluid energy and momentum, we simulate two cases of a radiating wall shock and compare the results to Zeus-MP2. Lastly, we investigate the degree to which our E* energy scheme is able to preserve an equilibrium polytrope.

6.1. Newtonian Gravity

The Poisson solver was tested in cylindrical coordinates against the analytic solution of an off-center sphere of constant density. The sphere is placed so that the origin of the coordinate system is at its surface. We tested the solution on four meshes of different resolution: $24\times48\times24$, $32 \times 64 \times 32$, $48 \times 96 \times 48$, and $64 \times 128 \times 64$, where the first number is the number of radial zones, the second the number of azimuthal zones, and the third the number of vertical zones. The right panel of Figure 6.1 demonstrates the solver converges to 2nd order, as expected. The

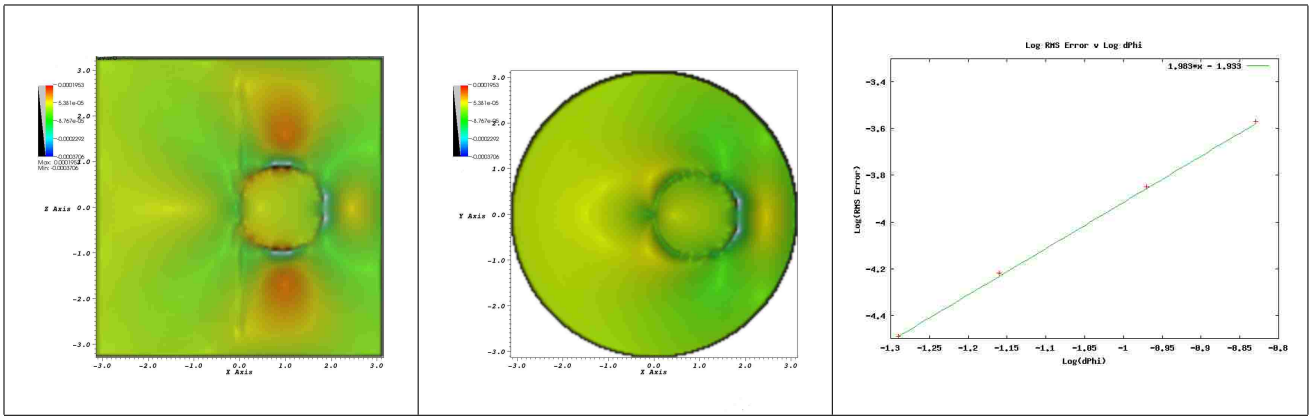

Fig. 6.1.— Poisson solver test. *Left:* The relative error in Φ on the vertical plane coincident with the sphere's center of mass. *Middle:* The error in Φ on the equatorial plan at $z = 0$. *Right:* The relative RMS error of Φ is plotted against the logarithm of size of Δ. The slope of the green line is 1.933, so convergence is very close to 2nd order.

left two panels of Figure 6.1 show the relative error for the $64 \times 128 \times 64$ case for two different slices through the grid. This error does not exceed 4×10^{-4} and it is largest on the surface of the sphere, where the gradient of the density is the steepest.

[1]Part of this section has been reproduced from Marcello & Tohline (2011) with the permission of the AAS (see Appendix D).

6.2. Sod Shock Tube[1]

The Sod shock tube problem is a Riemann problem which includes the three fundamental hydrodynamic waves: shock waves, contact discontinuities, and rarefaction waves (Sod (1978)). There are known analytic solutions to the problem, making it suitable as a test of basic hydrodynamics. The initial conditions are defined as

$$\rho = \begin{cases} 1.0 & z > 0 \\ 0.125 & \text{else} \end{cases}, \tag{6-1}$$

$$E_G = \begin{cases} 2.5 & z > 0 \\ 0.25 & \text{else} \end{cases}, \tag{6-2}$$

and

$$\mathbf{u} = 0. \tag{6-3}$$

We set $\gamma = 1.4$ and turn off reflection along the z plane. The simulation was run with 34 radial, 34 azimuthal, and 144 vertical interior zones. Figure (6.2) depicts, from left to right and top to bottom, the mass density, specific entropy, velocity, and pressure at time $t = 4.001$ for zones along the vertical line occupying the 22^{nd} radial and azimuthal locations. Comparing these results with those of our previous code in Figure 5 of Motl et al. (2002), we see that the present method represents the shock with greater accuracy. The width of the shock is narrower and there is an entropy jump across the shock. The method of Motl et al. (2002) did not include an equation for total gas energy and thus could not properly account for the shock jump conditions. The numerical solutions in both codes disagree slightly at the tail end of the rarefaction wave. The one way in which the present code is less accurate is at the contact discontinuity. The results of our code at the shock also compare favorably with those of other codes, including the ZEUS-2D code of Stone & Norman (1992) and most of the codes mentioned in Tasker et al. (2008). Other codes, such as FLASH, however, resolve the contact discontinuity better.

6.3. Marshak Wave[1]

There are few problems involving radiative transport that admit analytic solutions. Certain forms of the Marshak wave are an exception. In this problem, radiation is incident along the boundary of a semi-infinite slab of uniform optical opacity. Initially the slab is at zero temperature. In the original problem, described by Marshak (1958), the radiation and fluid temperatures were taken equal to one another throughout the evolution. Pomraning (1979) extended the problem to allow the radiation and fluid temperatures to evolve separately and presented a semi-analytic solution for the case where the speed of light is taken to be infinite. Su & Olson (1996) developed a semi-analytic solution for the case with a finite speed of light. To make an analytic solution possible, it is necessary to alter the heat capacity such that

$$e = c_0 T^4, \tag{6-4}$$

where c_0 is a constant. This linearizes the RHS of the radiation energy density equation and total gas energy equation. The hydrodynamics part of our code is disabled for this test problem. We

[1]This subsection has been reproduced from Marcello & Tohline (2011) with the permission of the AAS (see Appendix D).

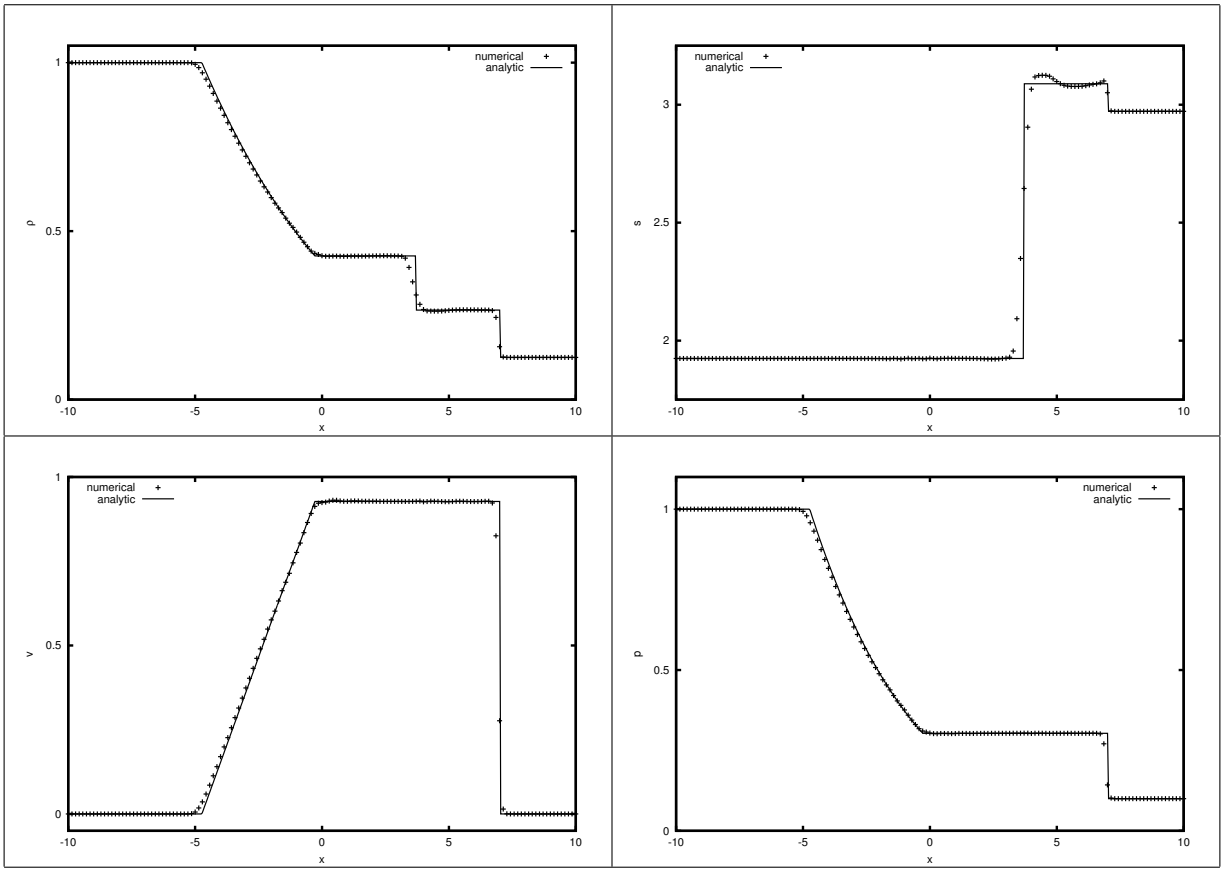

Fig. 6.2.— Sod's shock tube. Our code's results for the Sod shock tube are compared to analytic results at $t = 4.001$. *Top Left:* Density. *Top Right:* Specific entropy. *Bottom Left:* Velocity. *Bottom Right:* Pressure.

use a grid of 20 radial zones, 20 azimuthal zones, and 194 vertical interior zones. The Marshak boundary condition identified by Su & Olson (1996),

$$E_R\left(z = z_0, t\right) - \frac{2}{3\kappa}\frac{\partial}{\partial z}E_R\left(z = z_0, t\right) = \frac{4}{c}F_{\rm in}, \tag{6-5}$$

is imposed at all zones along the upper vertical boundary. The inflowing radiative flux, $F_{\rm in}$, is taken as 1. Outflow conditions are imposed at the lower vertical and outer radial boundaries.

In Figure 6.3 we compare our results to the semi-analytic results of Su & Olson (1996) in a format similar to their Figure 3 (Hayes et al. (2006) also uses a similar format). Depicted are the radiation and material energy densities at two sample times in the evolution. With the exception of a slight disagreement at the inflow boundary point, our results are consistent with the analytic results. Because the analytic solutions apply to a semi-infinite slab geometry, numerical results are not expected to be accurate once the wave hits the grid's outer boundary, and therefore the run is terminated close to that point.

6.4. Free-Streaming Radiation

In this problem we simulate a free-streaming front of radiation. The hydrodynamics are disabled, the radiation is decoupled from the gas equations, and the constant opacity is set such

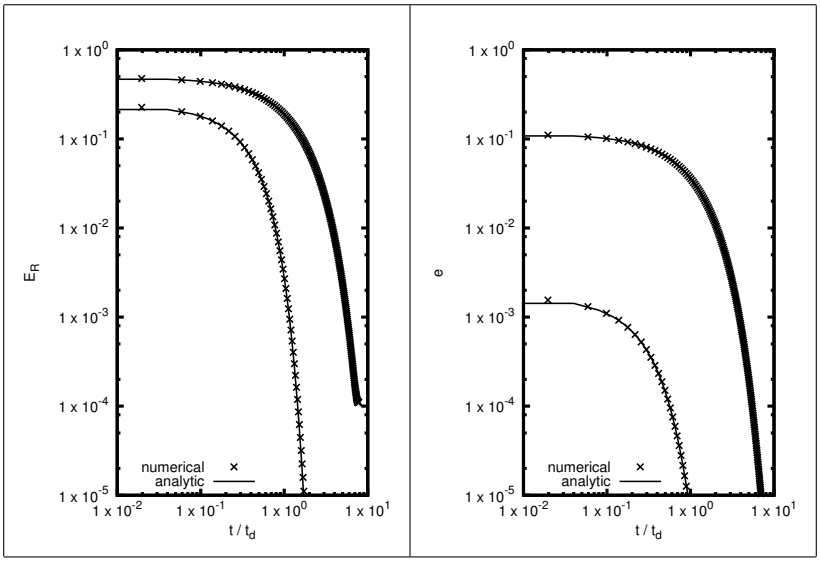

Fig. 6.3.— Marshak wave. Simulation for the Marshak wave is compared to analytic results. The top curve in both plots is at $t = 0.3$ and the bottom curve is at $t = 0.01$. *Left:* The radiation energy density versus vertical coordinate. *Right:* The internal gas energy density versus vertical coordinate.

that radiation is firmly in the free-streaming limit. The initial condition for the radiation energy profile is a step function

$$E = \begin{cases} 10 & \text{if} \quad z > 0 \\ 1 & \text{else} \end{cases}. \tag{6-6}$$

The simulation was run with several resolutions. The left panel of Figure 6.4 illustrates the results for a mesh of $96 \times 96 \times 96$ zones. Analytically, the waveform should propagate to the left at the speed of light, without changing its shape, but because we are using a diffusion approximation, the waveform quickly becomes smeared. As seen in the right panel of Figure 6.4, the results do converge, but at a rate less than 1$^{\text{st}}$ order. The wavefront propagates at approximately c, but otherwise the FLD approximation handles free-streaming radiation very crudely.

6.5. Dynamic Radiation Diffusion

If we remove the thermal source term from the radiation energy equation, in the diffusion limit for a constant fluid velocity, we obtain

$$\left[\frac{\partial}{\partial t} - \frac{1}{3}\frac{c}{\kappa}\nabla^2 + c\kappa\right] E_R = 0, \tag{6-7}$$

where we have set $\chi = \kappa_E = \kappa$ constant. Equation (6-7) is linear and has analytic solutions of the form

$$E_R \propto e^{ik - \left(\frac{c}{3\kappa}k^2 + c\kappa\right)t}, \tag{6-8}$$

where k is the wave number. A initial sine wave profile will decay over the timescale $t_{\text{decay}} := \left(\frac{c}{3\kappa}k^2 + c\kappa\right)^{-1}$. The decay is caused by two physical processes: diffusion, and absorption. The former appears as the $\frac{c}{3\kappa}k^2$ term and the latter as the $c\kappa$ term in equation (6-8). If the fluid is moving at a constant velocity, the waveform moves with it.

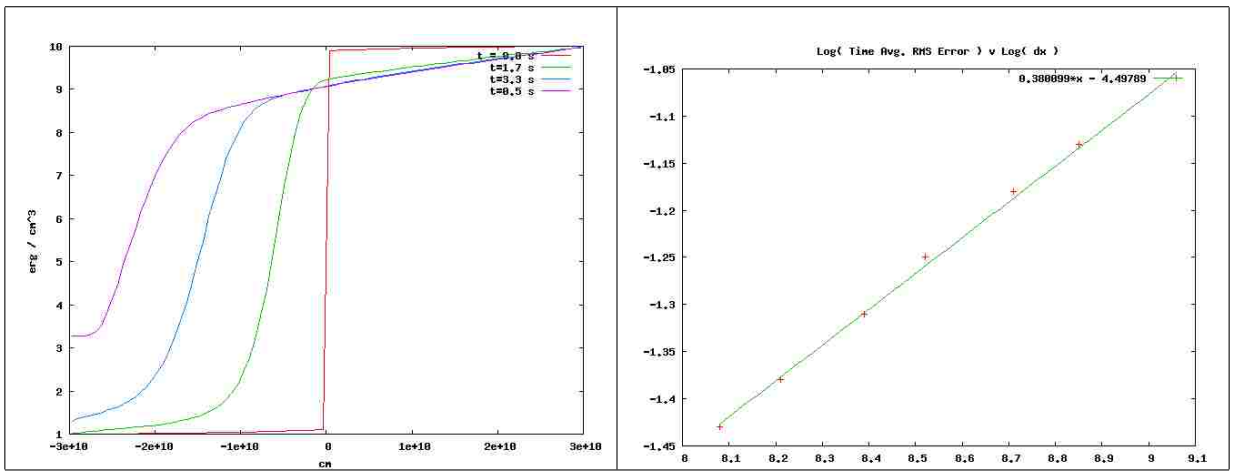

Fig. 6.4.— Free-streaming front of radiation. *Left:* Free-streaming front of radiation propagating to the left. Radiation energy density in erg/cm^3 is plotted against distance along the x-axis in cm. The red curve is for $t = 0.0$ s, the green curve is for $t = 1.67$ s, the blue curve is for $t = 3.33$ s, and the purple curve is for $t = 5.0$ s. *Right:* Convergence plot of free-streaming front of radiation propagating to the left. The RMS error for the solution is averaged over the entire time period of the run (1 s), and its logarithm is plotted against the logarithm of the cell size, Δx.

The results of such a diffusion problem are depicted in depicted in Fig. 6.5. This run was performed with a one-dimensional precursor to our new code with 256 zones and periodic boundary conditions. The wavenumber, k, is chosen such that the time decay due to absorption and diffusion are roughly equal. The flux limiter, Λ_E, is fixed at $\frac{1}{3}$ and the fluid propagates from the left to the right at constant velocity. In this case the FLD approximation results are nearly indistinguishable from the analytic solution. FLD performs well in the diffusion limit even with a moving fluid and significant absorption.

6.6. Radiating Shock Waves[1]

Coupled radiation and hydrodynamics does not readily admit test problems with analytic solutions. Nonetheless, the numerical results of different codes can be compared with one another for consistency. A problem suitable for these purposes, described in Ensman (1994), is the radiating shock wave. The problem in its one-dimensional form consists of a reflecting boundary condition on one end of the computational domain and an inflow boundary condition at the other. As the inflowing gas strikes the reflecting boundary, a shock wave is formed. In the purely hydrodynamical case, this wave forms a step discontinuity in mass density, velocity, and energy density. When radiation transport is present, the heat created at the shock front is radiated into the incoming gas stream, preheating it. When the radiation preheating is intense enough to heat the incoming material to the same temperature as the post-shock material, the shock is said to be super-critical. When the temperature of the incoming stream is below the temperature of the post-shock material, the shock is said to be sub-critical.

[1]This subsection has been reproduced from Marcello & Tohline (2011) with the permission of the AAS (see Appendix D).

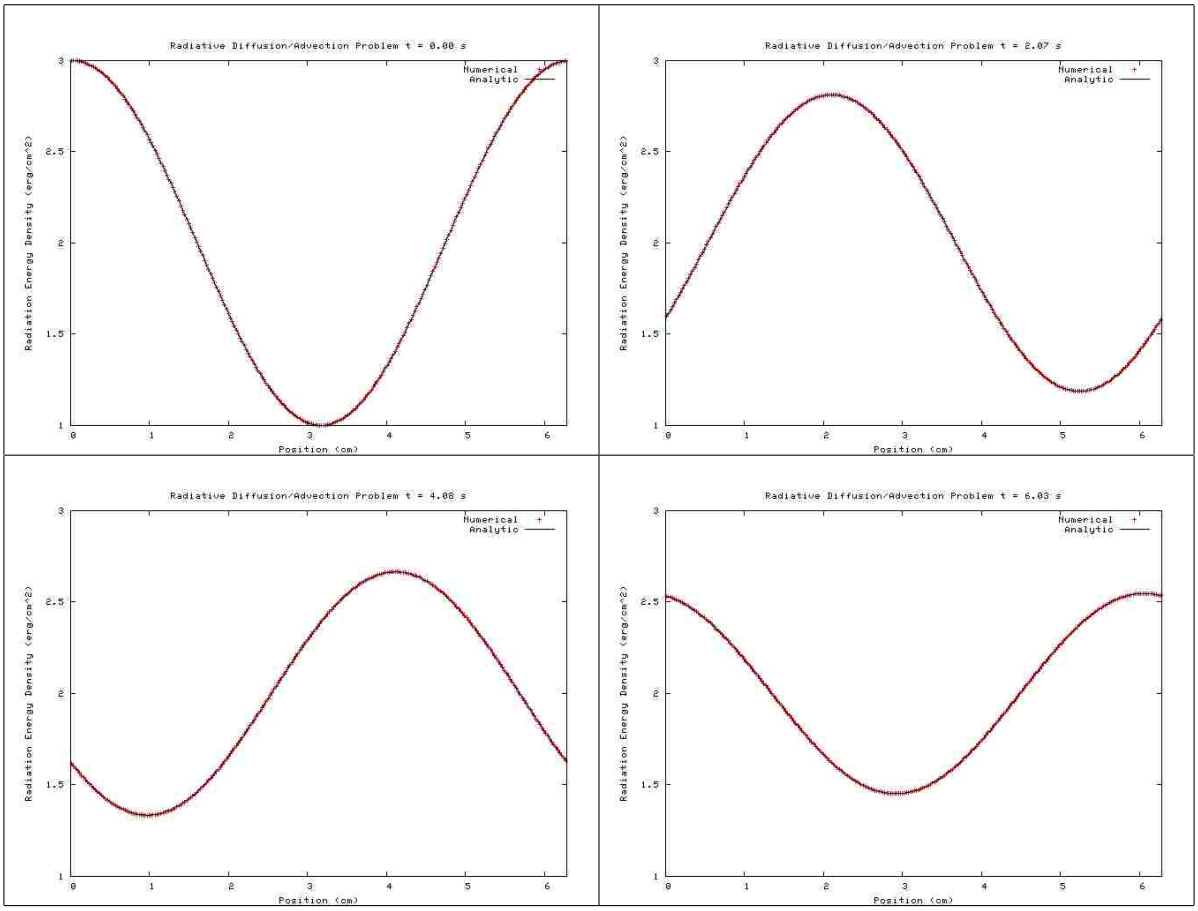

Fig. 6.5.— Dynamic radiation diffusion. Time series of a dynamic diffusion problem on a 256 zone grid. Radiation energy density, in erg/cm^3, is plotted against distance in cm. From left to right and top to bottom the plots correspond to times $t = 0.00$, 2.07, 4.08, and 4.83 seconds. The grid is periodic. The 1D waveform propagates from left to right due to advection and decreases in amplitude due to diffusion and coupling to the gas.

Figure 6.6 compares the results obtained with our code with results from the ZeusMP2 code of Hayes et al. (2006). Our computations were conducted using 10 radial, 26 azimuthal, and 256 vertical interior zones, with the in-falling gas injected at the upper vertical boundary. The ZeusMP2 runs were performed using a one-dimensional 256 zone mesh. The displayed profiles are averages of the plotted quantities over all radial and azimuthal zones for a given vertical displacement. In the problem as posed by Ensman (1994), the lab frame is co-moving with the in-falling gas and the reflecting boundary condition, acting as a piston, moves relative to the gas. Our Figure 6.6 is plotted in this frame, with the profile curves moving to the right in time. The left panels of Figure 6.6 are for the sub-critical case and the right panels for the super-critical case. The radiation temperature is displayed in the upper panels and the gas temperature in the lower panels. There is generally good agreement with ZeusMP2. The biggest disagreements are at times $t = 10^3$ s and $t = 1.3 \times 10^4$ s. In the former case, the difference is likely due to the different ways in which the codes handle shocks, and in the latter, likely due to differences in the outer z-boundary condition. The two codes also handle the gas pressure terms differently.

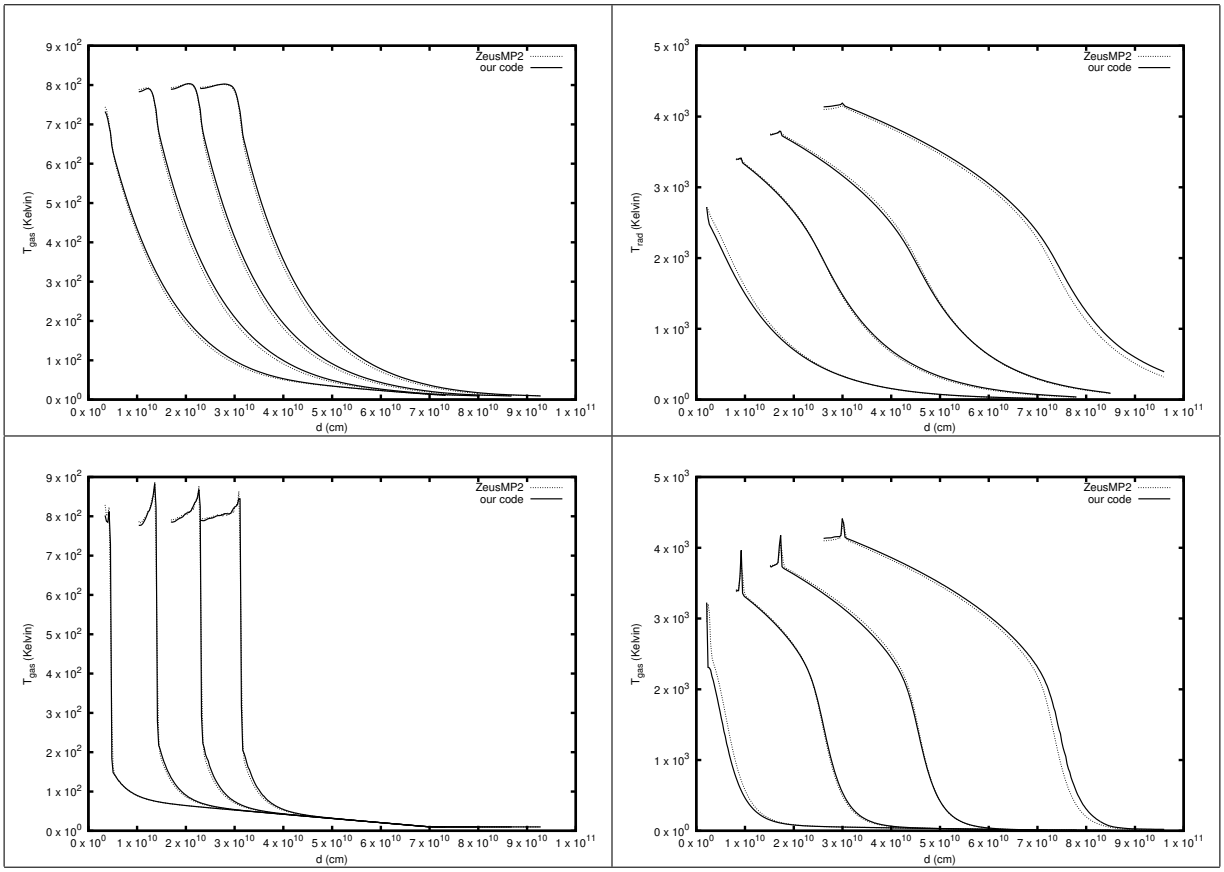

Fig. 6.6.— Radiating shock wave. Our code's results for the radiating shock wave are compared to results generated using ZeusMP2. The profiles are shown in the frame which is at rest relative to the inflowing gas. For the sub-critical shock (*left*), the times shown are $t = 5.5 \times 10^3$ s, $t = 1.7 \times 10^4$ s, $t = 1.7 \times 10^4$ s, $t = 2.8 \times 10^4$ s, and $t = 3.8 \times 10^4$ s. For the super-critical shock (*right*), the times shown are $t = 1.0 \times 10^3$ s, $t = 4.0 \times 10^3$ s, $t = 7.5 \times 10^3$ s, and $t = 1.3 \times 10^4$ s. *Top Left*: Radiation temperature profile for sub-critical shock. *Top Right*: Radiation temperature profile for super-critical shock. *Bottom Left*: Gas temperature profile for sub-critical shock. *Bottom Right*: Gas profile for super-critical shock.

6.7. Single Polytrope[1]

We have run a series of test simulations involving a single, spherically symmetric, polytropic star with polytropic index $n = \frac{3}{2}$. The initial density is computed by solving the Lane-Emden equation with a fourth-order Runge Kutta solver. The initial internal energy is then determined from equation (4-7) and equation (2-6). We have run four simulations, without radiation transport, at two resolutions. Each resolution is run with the E* energy correction and without it. The center of mass of the polytrope is initially coincident with the coordinate origin. The center of mass correction, described in Appendix C, was turned on for each run. The high (low) resolution run was computed with 94 (44) radial, 128 (64) azimuthal, and 44 (20) vertical interior zones. The polytrope has a radius of 33 (17) cells at high (low) resolution.

[1]A substantial portion of this subsection has been reproduced from Marcello & Tohline (2011) with the permission of the AAS (see Appendix D).

This initial configuration is placed in the cylindrical grid of our code and evolved for many dynamical time scales to test how well the code preserves the star's original structure. Figure 6.7 depicts the sum of $\mathcal{E}_{\rm con}$ (top panels) over the grid and the maximum density (bottom panels) on

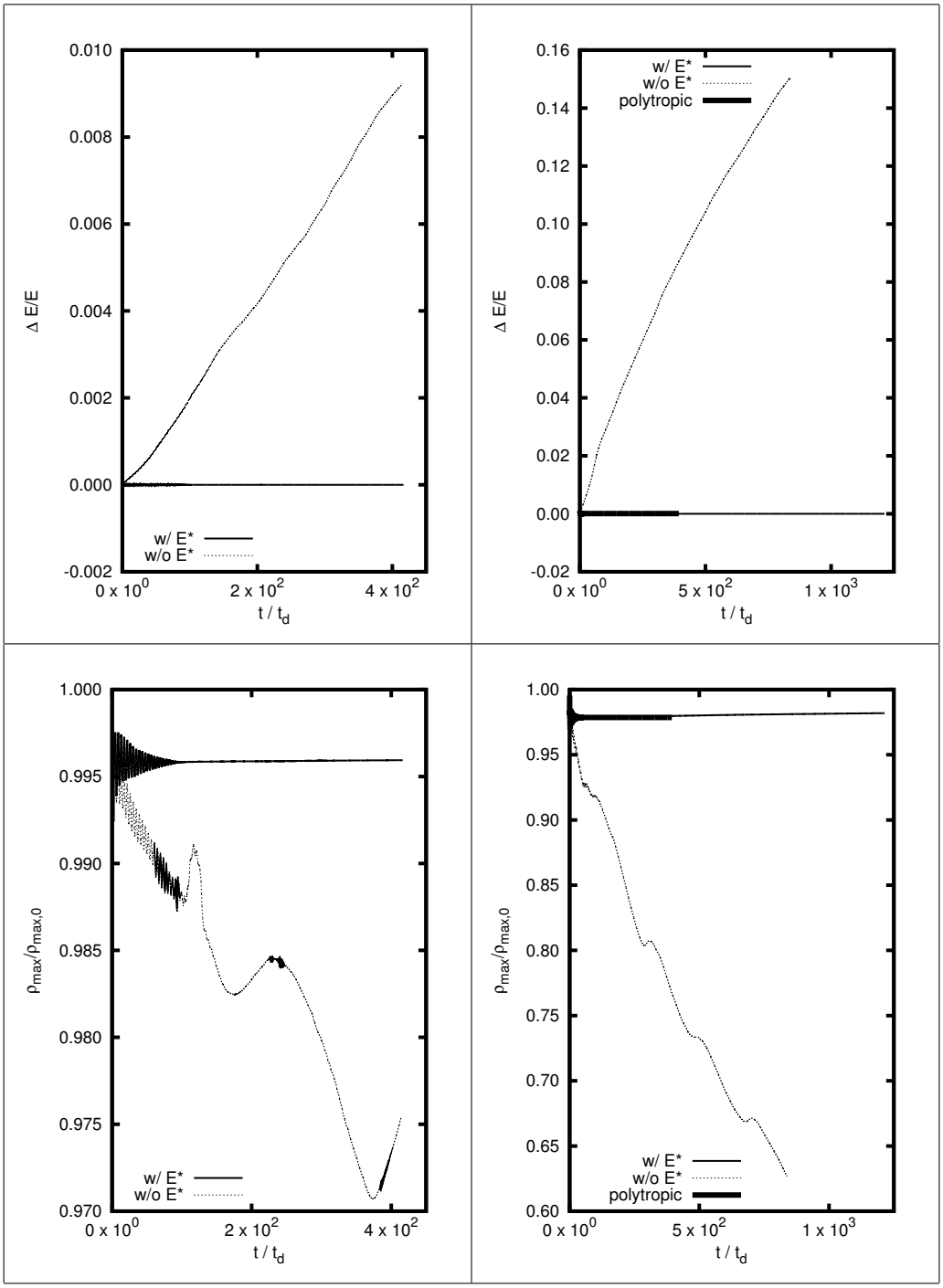

Fig. 6.7.— Single Polytrope. *Top Left*: Relative change in total energy from initial value for the high resolution run. *Top Right*: Relative change in total energy from initial value for the low resolution run. *Bottom Left*: Maximum density normalized to its initial value for the high resolution run. *Bottom Right*: Maximum density normalized to its initial value for the low resolution run.

the grid for the high (left panels) and low (right panels) resolution runs. The maximum density is equivalent to the central density for these particular simulations. With the E* correction turned on, the sum of $\mathcal{E}_{\rm con}$ remains nearly constant. Without the E* correction it increases monotonically with time. Similarly, the central density of the polytrope without the E* correction secularly decreases over time, while the central density of the polytrope with the E* correction oscillates for a few dozen dynamical timescales before it settles to a constant near its initial value.

The initial equilibrium numerical model with no internal velocity structure, as computed with the Lane-Emden equation, is initially *not* in equilibrium when placed in our dynamical solver. The model with the E* correction, when left to itself, is capable of forming a steady-state configuration within a few dozen dynamical timescales. The resulting steady-state configuration has the sawtooth radial momentum profile depicted by the solid curve in Figure 6.8. Despite the

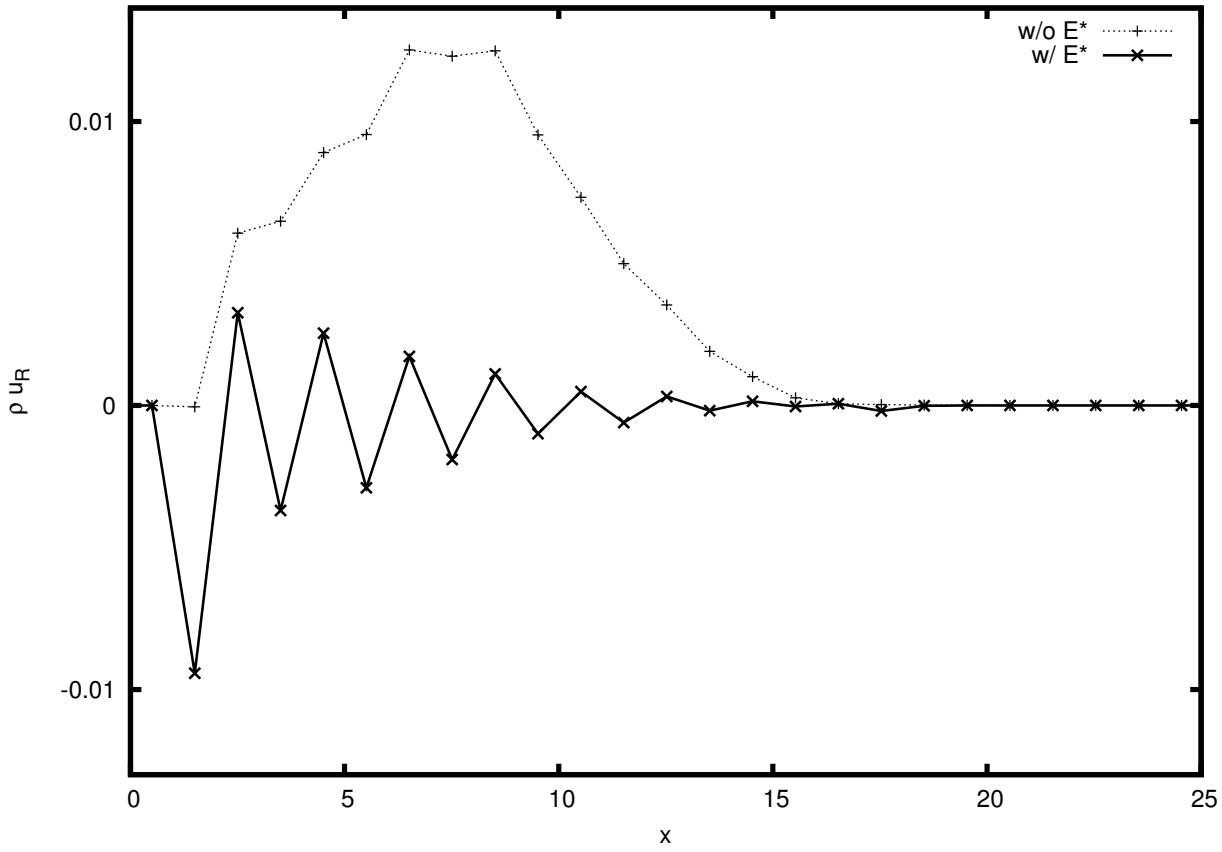

Fig. 6.8.— Centered polytrope radial momentum profile. The radial momentum profiles for the low resolution, centered polytrope with the E* correction (sold curve) and without it (dotted curve) at $t = 900$ dynamical timescales. This is several hundred dynamical timescales after the E* corrected polytrope settles into the depicted steady-state configuration.

non-zero velocities implied by this profile, the structure of the polytropic star is time-invariant. The physical fluxes resulting from the reconstructed evolution variables are canceled by the application of the viscosity operator in the K-T method. In the case without the E* correction, depicted by the dotted curve, the momentum is directed outward from the center of the polytrope for all but the inner two cells. The result is that the polytrope without the E* correction does not reach equilibrium within the several hundred dynamical timescales over which we have run

the simulation. If an equilibrium point is ever reached, the resulting evolution variable profiles will likely look nothing like the initial model. In contrast, the structure of the polytrope with the E* correction only deviates slightly from the initial conditions. Note that while the resulting radial momentum profile is oscillatory for the E* correction, the reconstructed total (physical plus viscous) fluxes at cell faces are not, as they sum to zero.

The binary simulations described below are evolved for over 20 orbital periods. From equation (2-14) we see that during this period both components will go through hundreds of dynamical times. Although the grid sizes used in our binary evolutions are larger than that used for the high resolution single polytrope runs, the binary components occupy only a slightly larger number of grid cells. Hence without the E* correction, they will tend to lose energy and dissipate on approximately the same time-scale as the high resolution single polytropes presented here.

We have also run four simulations with the spherical polytrope placed off of the coordinate center. Because we have chosen to evolve the radial, azimuthal, and vertical momenta instead of three Cartesian momenta, we cannot expect that the x and y Cartesian momenta will be conserved. Cartesian momenta are globally conserved for the centered polytrope due to symmetry. The off-center polytropes do not have this symmetry, and as a result, they act as if they are pushed by an outside force. As shown in the right panel of Figure 6.9, the polytrope is pushed

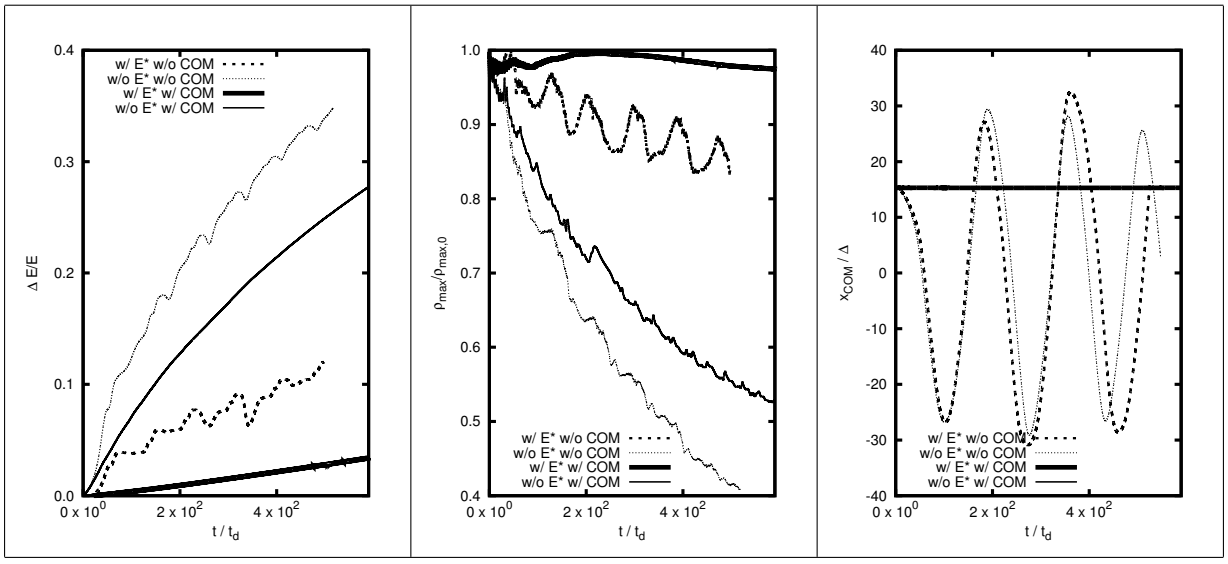

Fig. 6.9.— Off-center polytrope. *Left:* Relative change in total energy. *Middle:* Relative change in central density. *Right:* The x-location of the center of mass.

toward the coordinate center, passes it, and eventually changes directions, resulting in a roughly sinusoidal pattern. A similar effect was noted by Motl (2001), except the direction of the net force was away from the coordinate origin.

In Appendix C we detail a method we have used to correct for unphysical center of mass motion. For the simulations detailed in this paper, we have applied the center of mass correction to the above coordinate centered polytrope runs and to two of the off center runs. For the off-center polytrope runs, this correction cancels out the net force pushing on the polytrope. As seen in Figure 6.9, both the center of mass correction and the E* corrections result in better conservation of total energy (left panel) and a more stable equilibrium configuration. Unlike the coordinate centered runs, however, even with both corrections in use, there is a noticeable increase in the total energy over many dynamical timescales.

7. $q = 0.7$ Binary Simulations[1]

Here we present the results of two binary simulations. Both begin with the same initial condition of a polytropic binary with mass ratio $q = 0.7$ with the less massive star filling its Roche lobe. In one of the runs, we have disabled the radiation feature. We call this run "$q = 0.7b$". We refer to the run with the radiation feature enabled as "$q = 0.7a$". We evolved each on a grid with 159 radial, 256 azimuthal, and 49 vertical interior grid zones. We used reflective symmetry about the equatorial plane, so the effective size in the vertical direction is 98 zones. The initial equatorial plane mass density distribution and Roche configuration is shown in Figure 7.1. The logarithmic color scale runs from 10^{-6} to 10^{0} in code units and the contour lines are contours of the effective potential.

7.1. Initial Conditions

The initial conditions were generated using a self-consistent field (SCF) technique similar to that of Hachisu (1986). We have used this technique for several of our previous simulations (e.g. New & Tohline (1997), Motl et al. (2002), D'Souza et al. (2006)), and recently we have extended it to include a cold white dwarf equation of state (Even & Tohline (2009)). For the present simulations we use the SCF technique with a polytropic equation of state. The polytropic index is set to $n = \frac{3}{2}$. The SCF code generates an initial density configuration and a polytropic constant, K, for each component, and determines the orbital period and separation. The parameters of the SCF model used for these simulations are given in Table 7.1.

Given the density and polytropic constants, p in equation (4-6) is set equal to $P_{\rm poly}$ in equation (2-6), to obtain the initial internal energy density for the $q = 0.7b$ run. The $q = 0.7a$ run requires that we also compute an initial value for the radiation energy density. For the interiors of the stars, where the radiation diffusion approximation applies, the radiation and gas temperatures are equal and the pressure due to radiation is isotropic. In this limit the radiation pressure is

$$P_{\rm rad} = \frac{1}{3} E_R = \frac{4}{3} \frac{\sigma}{c} T^4. \tag{7-1}$$

[1]This section and its subsections have been reproduced from Marcello & Tohline (2011) with the permission of the AAS (see Appendix D).

Table 7.1: $q = 0.7$ Initial Parameters [a]

	Donor	Accretor
Mass	0.282	0.403
Effective Radius	0.887	0.840
Central Mass Density	0.608	1.000
Polytropic Constant (K)	0.236	0.257
Period	31.19	
Separation	2.58	
Grid Spacing	$\frac{\pi}{128} \approx 0.0245$	

[*]These values are in "code" units.

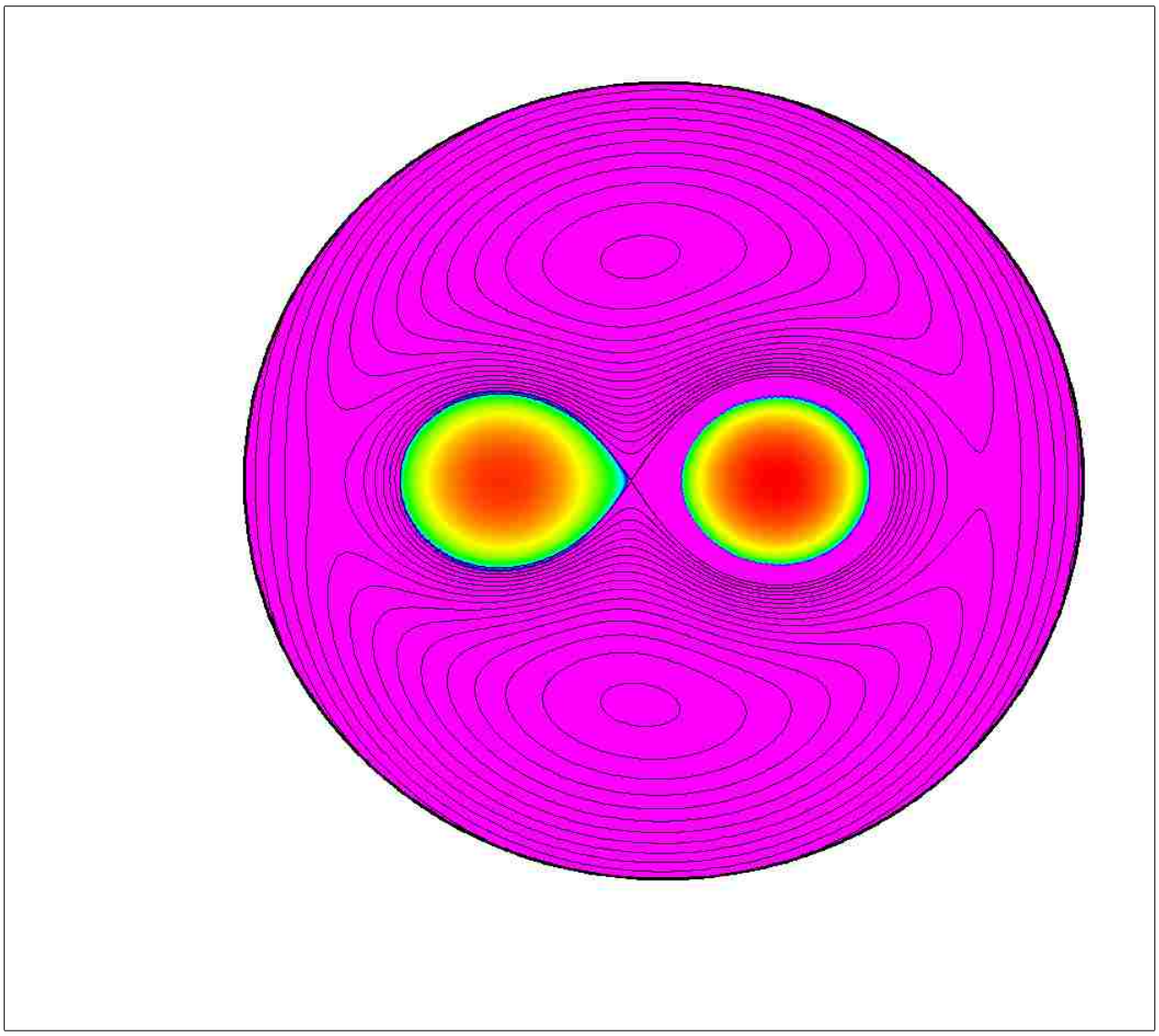

Fig. 7.1.— Initial equatorial plane mass distribution for the $q = 0.7a$ and $q = 0.7b$ runs at $t = 0$. The logarithmic color scale runs from 10^{-6} to 10^{0} in code units. The black lines are contours of effective potential for $\Phi_{\rm eff} \geq \Phi_{\rm L1}$.

We set the sum of the radiation and gas pressures equal to the polytropic pressure,

$$P_{\rm poly} = K\rho^{1+\frac{1}{n}} = \frac{\mathcal{R}}{\mu}\rho T + \frac{4}{3}\frac{\sigma}{c}T^4, \tag{7-2}$$

and numerically solve for T. Then, using equations (4-7) and (7-1), we set the initial values for internal and radiation energy densities, respectively.

The results of our previous simulations without radiation and with a polytropic equation of state had the benefit of scalability. They were evolved using equations which contain three fundamental units of measure (length, time, and mass), but only one physical constant, Newton's gravitational constant. For a given value of that constant as represented in the code, one is free to choose two out of three scaling constants for the length, mass, and time. With the introduction of radiation transport to the simulation, there are now four independent physical constants in

the equation set: (1) the speed of light, (2) the Stefan-Boltzmann constant, (3) the gas constant, and (4) Newton's gravitational constant. Setting these constants fixes the ratio of code units to physical units for length, time, mass, and temperature to only one possible value for each. Therefore the simulation results correspond to a unique physical system. In Table 7.2 we list our choice of physical constants for the binary runs, in code units. Note that only G has to be specified in the $q = 0.7b$ run. For the $q = 0.7a$ run, this choice of constants fixes the the ratio of code units to cgs units. These are shown in Table 7.3. The binary presented here has a period of 1685 s and components with masses $0.57M_\odot$ and $0.40M_\odot$ and respective radii $0.098R_\odot$ and $0.104R_\odot$. Physically the radii are about ten times too large for fully degenerate white dwarfs (there do exist, however, semi-degenerate helium stars with radii of the same order). The main purpose of these two simulations was to test the method described above rather than to simulate a particular realistic system.

We must also be careful in our choice of γ. If the entropy gradient is opposite the pressure gradient, convective instability results. To avoid instability without radiation, setting $\gamma \geq 1 + \frac{1}{n}$ is sufficient. Since $\gamma = \frac{5}{3}$ for a monatomic ideal gas, and $1 + \frac{1}{n} = \frac{5}{3}$ for an $n = \frac{3}{2}$ polytrope, usually we would set $\gamma = \frac{5}{3}$. This results in an isentropic entropy profile. The addition of radiation, however, changes the entropy profile. Since the temperature is now set by equation (7-2) instead of equation (4-7), the entropy profile runs with the pressure gradient. One way to get the entropy gradient to point in the right direction is to set γ to a higher value. Chandrasekhar (1939) gives an equation for determining the minimum γ needed (Chapter IV equation (42)). This equation depends only on the ratio of central gas pressure to the central total pressure,

$$\beta_{\rm rad} := \frac{\mathcal{R}T}{\mu K \rho^{1+\frac{1}{n}}}. \tag{7-3}$$

Our choice of the values of c and $\frac{\mathcal{R}}{\mu}$ for a given polytropic constant and density determine the value of $\beta_{\rm rad}$. For the $q = 0.7a$ run, $\beta_{\rm rad}$ is approximately 0.9996 at the center of the donor and 0.9936 at the center of the accretor. We set $\gamma = 1.671$ for the $q = 0.7a$ and $q = 0.7b$ runs. By Chandrasekhar (1939), for the $q = 0.7a$ run, donor stability requires $\gamma \geq 1.667$ and accretor stability requires $\gamma \geq 1.713$. Our accretor should therefore show a convective instability, but we have found that none develops on the timescale of the simulation. The region of the accretor which should theoretically be unstable is at the center of the accretor and occupies less than 2% of its total volume. It is possible that since the accretor is just barely over the convective stability limit in this region, numerical viscosity is sufficient to prevent instability. Although this change in γ is not required to keep the $q = 0.7b$ model stable against convection, we include it for consistency with the $q = 0.7a$ model.

Outside of the two stars we simply set the internal gas and radiation energy densities to their floor values. For the present simulations, theses values are 1.49×10^{-23} and 1.174×10^{-24},

Table 7.2: $q = 0.7$ Physical Constants in Code Units

Newton's gravitational constant (G)	1.00×10^{0}	$l^3_{\rm code}/m_{\rm code}/t^2_{\rm code}$
speed of light (c)	1.98×10^{2}	$l^3_{\rm code}/t_{\rm code}$
gas constant ($\frac{\mathcal{R}}{\mu}$) [a]	4.40×10^{-1}	$l^2_{\rm code}/t^2_{\rm code}/K_{\rm code}$
Stefan-Boltzmann constant (σ)	2.18×10^{0}	$m_{\rm code}/t^3_{\rm code}/K^4_{\rm code}$

[a] The gas constant only appears in the equations divided by the mean molecular weight.

respectively, in code units. They were chosen such that the radiation coupling terms (i.e. the RHS of equation (4-3) will sum to zero.

7.2. Quality of Results

The $q = 0.7a$ and $q = 0.7b$ runs were evolved for approximately 23 and 25 orbits, respectively. The relative change in the total angular momentum (left panel), mass (middle panel), and energy (right panel) are plotted in Figure 7.2. The runs were terminated because the center of mass

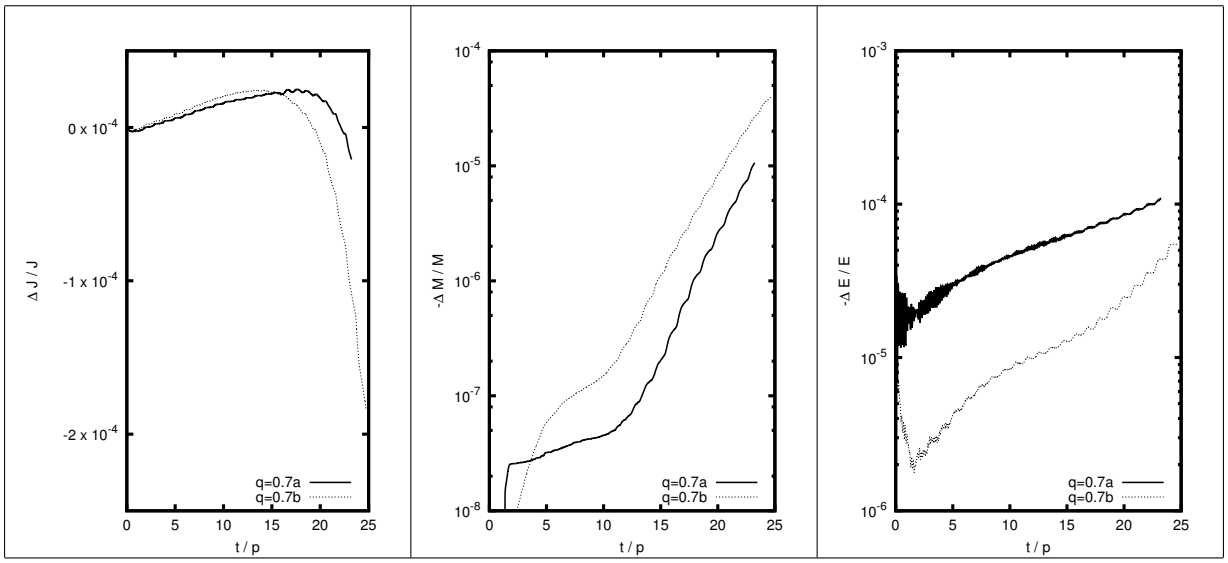

Fig. 7.2.— Total angular momentum, mass, and energy for the $q = 0.7a$ (solid curve) and $q = 0.7b$ (dotted curve) runs. *Left:* The relative change in the total z-angular momentum on the grid from its initial value. *Middle:* The negative of relative change in the total mass on the grid from its initial value. *Right:* The negative of relative change in the total energy on the grid from its initial value.

moved off the coordinate origin by several grid zones (see left most panel in Figure 7.3). D'Souza et al. (2006) used a center of mass correction. We did not use such a correction for the $q = 0.7a$ and $q = 0.7b$ runs. There is significant epicyclic variation evident in many of the Figures towards the end of each run, and we believe this is primarily due to the wandering center of mass. Our chosen grid size also turned out to be too small. The expanded atmospheres of the stars were beginning to come into contact with the upper vertical boundary shortly before terminating each run. This is the reason for the accelerated rate of mass loss seen in the middle panel of Figure 7.4. Since the $q = 0.7a$ and $q = 0.7b$ runs we have added a correction to the present code (see Appendix C). This correction is used in some of the single polytrope runs described in §6.7 and

Table 7.3: $q = 0.7$ Real Units per Code Unit

$l_{\rm code}$	8.18×10^9 cm
$m_{\rm code}$	2.81×10^{33} g
$t_{\rm code}$	5.40×10^1 s
$K_{\rm code}$	1.62×10^8 °K

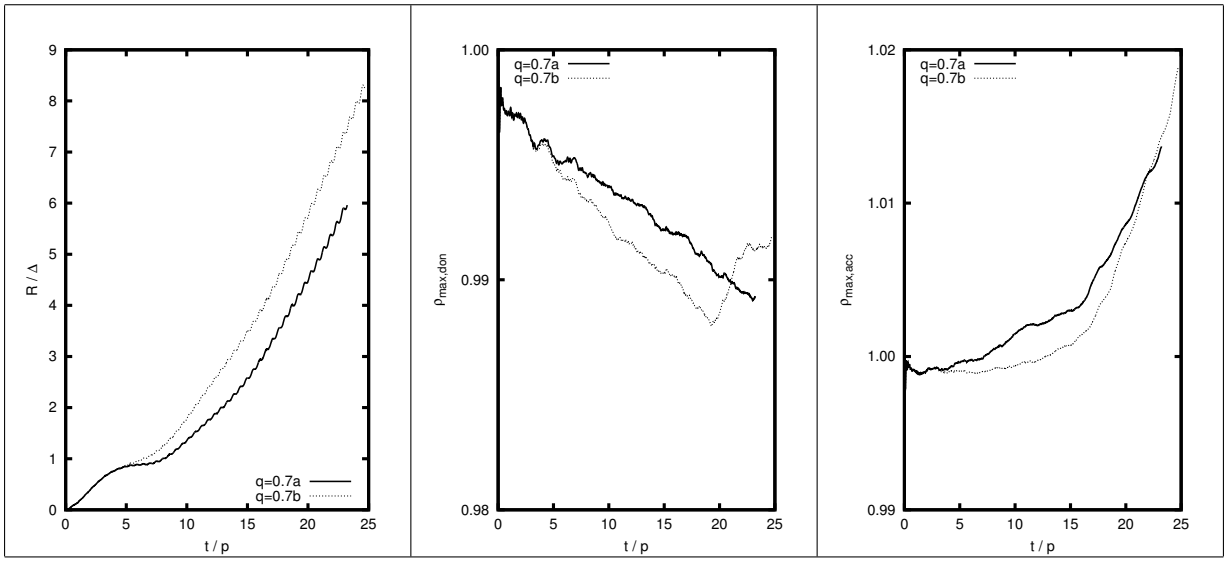

Fig. 7.3.— Center of mass location and maximum densities for the $q = 0.7a$ (solid curve) and $q = 0.7b$ (dotted curve) runs. *Left:* The orbit averaged radial location of the center of mass of the entire grid. *Middle:* The orbit averaged maximum density of the donor, normalized to its initial value. *Right:* The orbit averaged maximum density of the accretor, normalized to its initial value.

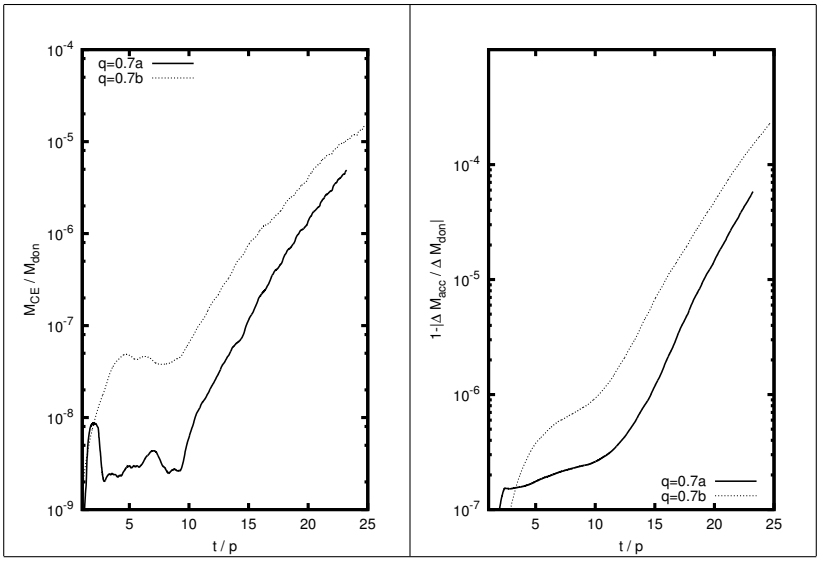

Fig. 7.4.— Common envelope mass and fraction of mass lost for the $q = 0.7a$ (solid curve) and $q = 0.7b$ (dotted curve) runs. *Left:* The orbit averaged mass of the common envelope, normalized to the mass of the donor. *Right:* The running total of the fraction of mass lost from the donor that is not captured by the accretor.

in the $q = 0.4$ runs of §8.

As seen in Figure 7.2, relative mass loss through the grid boundaries of the same order as the relative changes in total angular momentum and energy does not begin until just after the 15^{th} period. We may therefore assume that most all of the changes in angular momentum and

total energy at early times are due to error in the numerical scheme. During this period of the evolution, the total z-angular momentum is conserved to within a relative error of approximately 1.7×10^{-6} per orbit. This is a marked improvement over our previous code, which conserves angular momentum to within an error of about 1×10^{-4} per orbit (Motl et al. (2002)), and it is on par with recent SPH codes (Yoon et al. (2007), Guerrero et al. (2004)). Because of the E* scheme, our code is able to conserve total energy to even better accuracy. Over the first 15 orbits, total energy is conserved to within a relative error of about 8×10^{-7} per orbit for the $q = 0.7b$ run and 4×10^{-6} per orbit for the $q = 0.7a$ run. Although we should expect the $q = 0.7a$ run to lose total energy by radiation leaving the grid, as will be shown below the amount of radiative luminosity is not enough to account for the higher error in the $q = 0.7a$ run relative to the $q = 0.7b$. Each of the runs conserve total energy better than the SPH codes mentioned above.

For the purposes of producing the figures, we have defined the "common envelope" to be any point on the grid for which $\Phi_{\rm eff} + \frac{1}{2}\mathbf{u}^2 < \Phi_{L2}$, where Φ_{L2} is the effective potential at the stationary point opposite the donor from the accretor. If its gravitational binding energy is below this threshold, a grid cell belongs to either the accretor or donor depending on which of the two exerts more gravitational acceleration at that point.

Four still frames from the $5^{\rm th}$, $10^{\rm th}$, $15^{\rm th}$, $20^{\rm th}$ orbit for both runs are shown in Figures 7.5 through 7.7. Figures 7.5 and 7.7 show density with a logarithmic color scale, in code units,

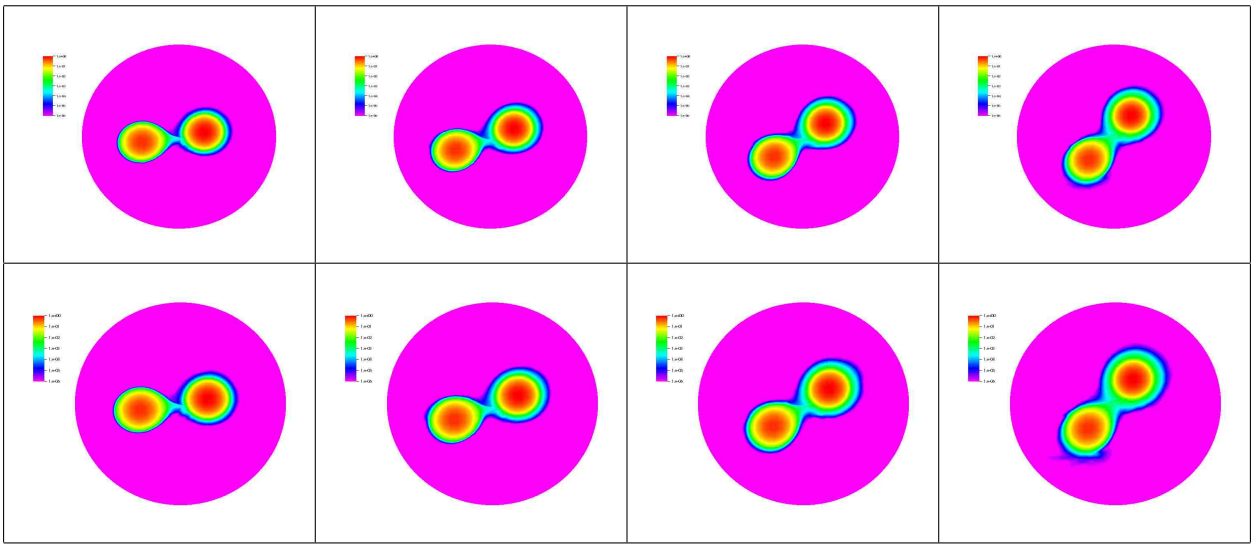

Fig. 7.5.— High density range equatorial slices for $q = 0.7$ runs. These are density plots of a slice through the equatorial plane for the $q = 0.7$ runs. The top row is the $q = 0.7a$ run and the bottom row the $q = 0.7b$ run. From left to right, the columns correspond to $t = 5$ orbits, 10 orbits, 15 orbits, and 20 orbits. The color density scale runs from 10^{-6} to 1 in code units.

running from 10^{-6} to 10^{0}. To highlight the low density regions, the logarithmic density scale in Figure 7.6 runs from 10^{-12} to 10^{-6}. Figures 7.5 and 7.6 depict slices through the equatorial plane, while Figure 7.7 is a slice through the plane perpendicular to the equatorial plane and coincident with the center of mass of both stars. The $q = 0.7a$ run in Figure 7.6 also contains contour lines. For this plot, we have defined regions of super-Eddington accretion to be any region for which the condition

$$-\mathbf{f}_{\rm rad} \cdot \mathbf{f}_{\rm grav} \leq \mathbf{f}_{\rm grav} \cdot \mathbf{f}_{\rm grav}, \tag{7-4}$$

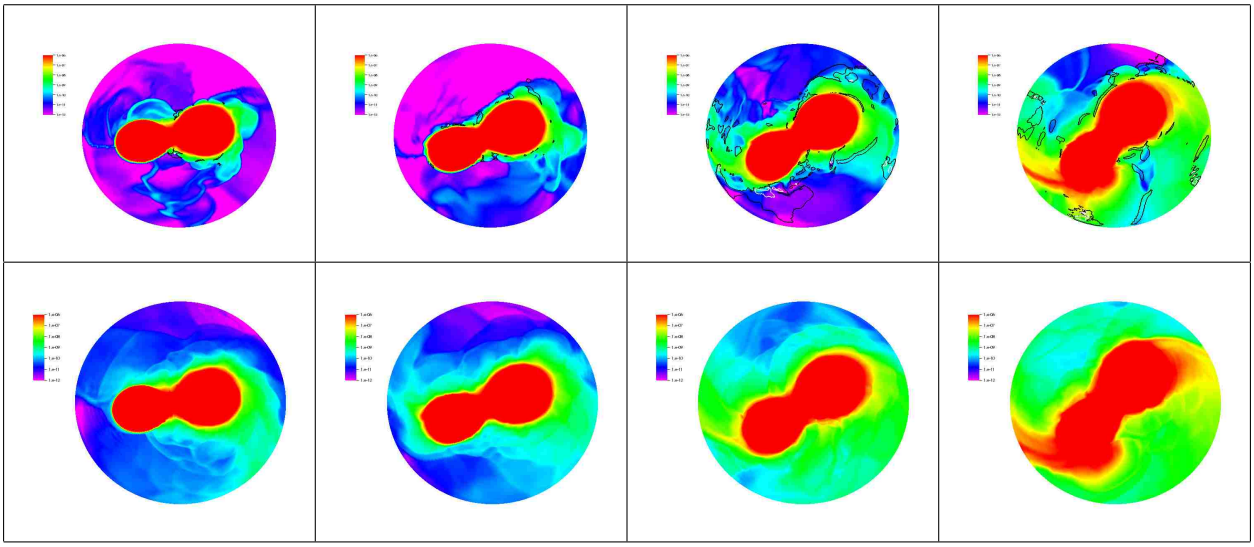

Fig. 7.6.— Low density range equatorial slices for $q = 0.7$ runs. These are density plots of a slice through the equatorial plane, with the scale altered to highlight low density regions. The top row is the $q = 0.7a$ run and the bottom row the $q = 0.7b$ run. From left to right, the columns correspond to $t = 5$ orbits, 10 orbits, 15 orbits, and 20 orbits. The color density scale runs from 10^{-12} to 10^{-6} in code units. For the $q = 0.7a$ run we have also plotted black contours around regions in which the flow is super-Eddington. The white contours are regions where the radiation is ten times or more super-Eddington. The definition of these contours is provided in the last paragraph of §7.2

.

is satisfied. Here, $\mathbf{f}_{\rm rad} := -\Lambda_E \nabla E_R$ and $\mathbf{f}_{\rm grav} := -\rho \nabla \Phi$ are the forces of radiation and gravity, respectively. This condition is satisfied inside the black contours. Inside the white contours, the force of radiation is ten times more than what is needed to satisfy equation (7-4). Figure 7.8 is a close-up of the $15^{\rm th}$ orbit for the $q = 0.4a$ run in Figure 7.6.

7.3. Discussion

Immediately after the evolution begins, the donor in both runs overflows its Roche lobe. Although the initial configuration is in equilibrium according to the algebraic system of equations used by the SCF code, it is slightly out of equilibrium once placed in the hydrodynamics code. As seen in the upper left panel of Figure 7.9, mass transfer proceeds at a steadily increasing rate until about the $15^{\rm th}$ orbit. At this point the transfer rate begins to grow suddenly. It is generally expected that runaway mass transfer will occur for binaries of this mass ratio. The mass within the common envelope is relatively very small, and hence the rate of increase of the accretor's mass is nearly the same as the rate of decrease of the donor's. In the upper middle and upper right panel, we see that the Roche lobe effective radius and orbital separation shrink throughout the evolution, consistent with dynamically unstable mass transfer. We define the Roche lobe effective radius as the radius of the sphere with the same volume as the Roche lobe. As more mass is removed from the donor and piled onto the accretor, the central density of the donor decreases while increasing for the accretor (see the middle and right panels of Figure 7.3, respectively). As seen in the bottom left panel of Figure 7.9, initially the donor's spin

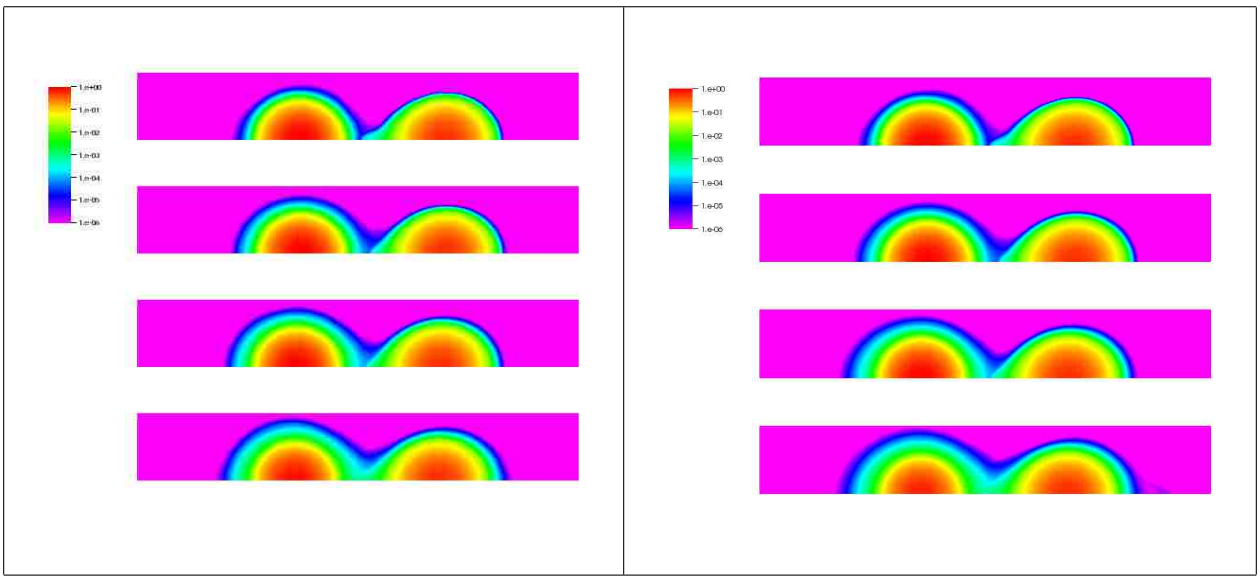

Fig. 7.7.— Density for the $q = 0.7$ runs in the vertical slice perpendicular to the equatorial plane and coinciding with the line running from one star's center of mass to the other's. The left column is the $q = 0.7a$ run and the right column the $q = 0.7b$ run. From top to bottom, the rows correspond to $t = 5$ orbits, 10 orbits, 15 orbits, and 20 orbits. The color density scale runs from 10^{-6} to 1 in code units. Note that we use symmetry across the equatorial plane in these simulations, so there is only a "top" half of the grid.

angular momentum increases very slightly, but after a few orbits it decreases monotonically for the remainder of the evolution. The accretor's spin angular momentum increases throughout the evolution (see bottom middle panel of Figure 7.9). There are a variety of forces in play here: the transport of angular momentum from the donor to accretor by advection; the gravitational tidal interaction between donor and accretor; and the torque created by the accretion stream impacting the accretor off-center.

The stationary point in $\Phi_{\rm eff}$ which lies between the two stars is the L1 point. As seen in the left panel of Figure 7.10, almost all of the common envelope has roughly the same specific kinetic energy as the difference in effective potential between the L1 point and the surface of the accretor, independent of time. This is consistent with physical expectations, as in order for a piece of the fluid to reach a potential high enough to escape into the common envelope, it must have sufficient kinetic energy. In the middle panel, we see that initially the specific radiation energy exceeds specific internal energy in the common envelope for the $q = 0.7a$ run. This is reversed as the envelope cools by radiative transport and as a higher rate of mass transfer produces more internal gas energy. In the right panel, we show the inertial frame specific gravitational binding energy of the envelope in units of $\Phi_{\rm L1}$. The envelope remains above the energy of the L1 point throughout the evolution, yet very little of the mass on the grid is above zero binding energy. However, as seen in the right panel of Figure 7.11, relative to the $q = 0.7b$ run, far more grid material is gravitationally unbound in the $q = 0.7a$ run. After approximately the $6^{\rm th}$ orbit, none of the material in the $q = 0.7b$ run is unbound, while a fraction (albeit tiny) of the material in the $q = 0.7a$ run is unbound throughout the simulation.

The accretion luminosity of both runs is shown in the left panel of Figure 7.11. For the $q = 0.7a$ run, the radiation luminosity that escapes through the grid boundaries is also shown.

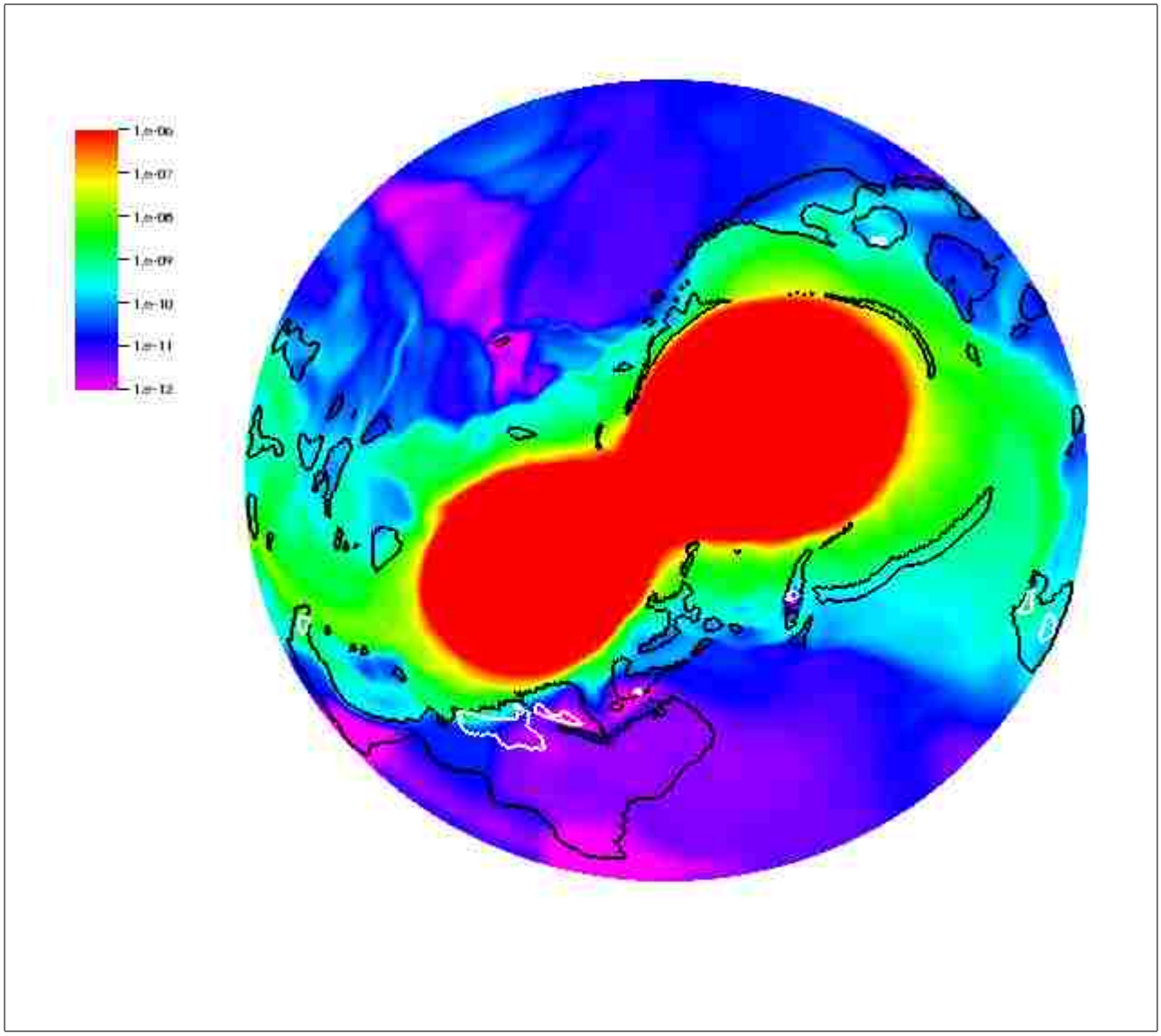

Fig. 7.8.— Close up of low density plot for $q = 0.7a$ at 15 orbits. This figure is seen from the upper row of Figure 7.6, third from the left.

These luminosities are normalized to the nominal Eddington luminosity for spherical accretion. The accretion luminosity of both runs exceeds the radiative luminosity of the $q = 0.7a$ run by many orders of magnitude. The radiative luminosity itself is roughly on the order of $L_{\rm Edd}$. This is consistent with the prediction by Han & Webbink (1999) that most of the radiation in a highly super-Eddington mass transfer will be swept up by the accretion flow, leaving approximately the Eddington luminosity to escape. Between the $q = 0.7a$ and $q = 0.7b$ runs, however, we see very little substantial differences between the state of the donor and accretor. The mass transfer rates and central densities begin to diverge from one another at about the 11^{th} orbit, and the transfer rate of the $q = 0.7a$ run is less than the $q = 0.7b$ run. Although this is consistent with super-Eddington accretion, other evidence suggests that the force of radiation cannot be the cause of these differences. As seen in Figure 7.6, very little of the matter is actually in a region of space where the force of radiation is sufficient to cancel the force of gravity. The lowest density depicted

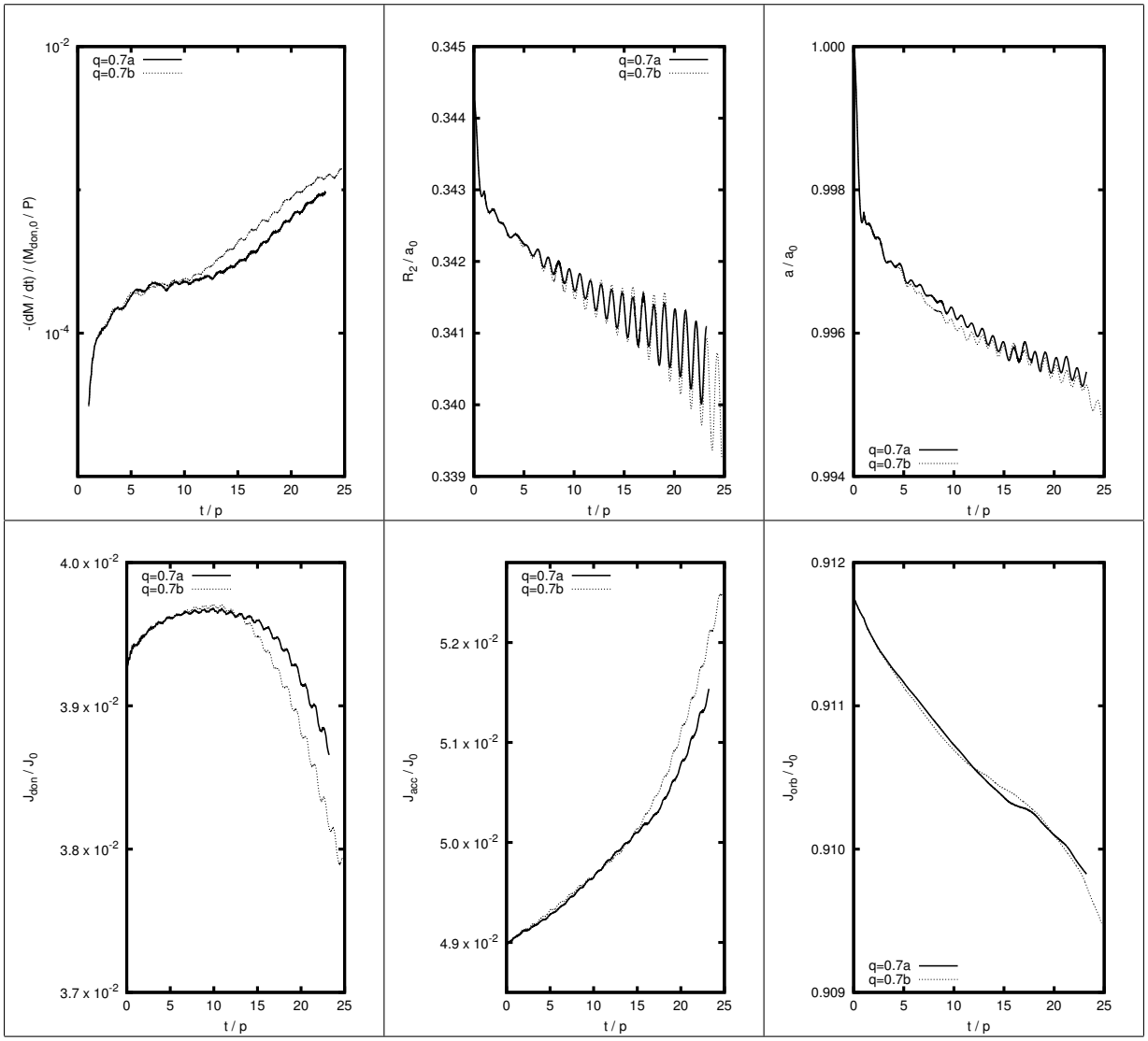

Fig. 7.9.— Mass transfer rate, Roche lobe radius, orbital separation, and angular momenta of the $q = 0.7a$ (solid curve) and $q = 0.7b$ (dotted curve) runs. *Top Left:* The orbit averaged rate of mass transfer from the donor, normalized to donor masses per orbital period. *Top Middle:* The orbit averaged effective Roche lobe radius of the donor, in units of the initial orbital separation. *Top Right:* The orbit averaged orbital separation normalized to its initial value; *Bottom Left:* The spin angular momentum of the donor, in units of initial total angular momentum. *Bottom Middle:* The spin angular momentum of the accretor, in units of initial total angular momentum. *Bottom Right:* The orbit averaged orbital angular momentum, in units of initial total angular momentum.

in Figure 7.6, represented by the color purple, is on the order of the lowest optically thick density. As the run progresses the grid fills with optically thick material, and the radiation field is mostly in the diffusion limit. Since the flow is dominated by advection, the radiation produced where the stream impacts the accretor simply moves with the flow of the material, rather than escaping the material and exerting a force on the stream further up. If anything, it would appear the presence of radiation *reduces* the flow of material into the common envelope. In the color figures of the

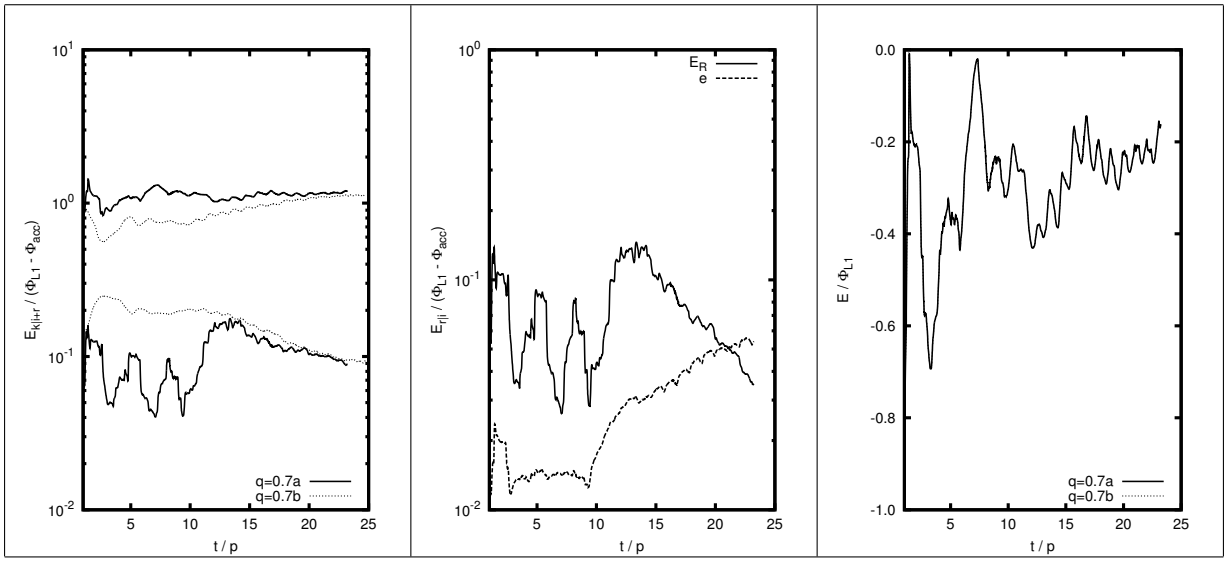

Fig. 7.10.— Common envelope specific energies of the $q = 0.7$ runs. *Left:* The top two curves are the orbit averaged specific kinetic energies. For the $q = 0.7b$ run (dotted curve), the bottom curve is the orbit averaged specific internal energy. For $q = 0.7a$ run (solid curve), the bottom curve is the sum of the orbit averaged specific internal and specific radiation energies. All are plotted in units of $\Phi_{L1} - \Phi_{acc}$. *Middle:* The orbit averaged specific radiation energy (solid curve) and the orbit averaged specific internal energy (dotted curve) for the $q = 0.7a$ run, in units of $\Phi_{L1} - \Phi_{acc}$. *Right:* The orbit averaged specific gravitational binding energy of the common envelope, in units of Φ_{L1}, taken in the inertial frame for the $q = 0.7a$ (solid curve) and $q = 0.7b$ (dotted curve) runs.

evolution (Figures 7.5, 7.6, and 7.7), the envelope seems to be less extended for the $q = 0.7a$ run. Because the envelope begins to flow off the grid, however, we cannot make any firm conclusions about its evolution past the first few orbits using these simulations.

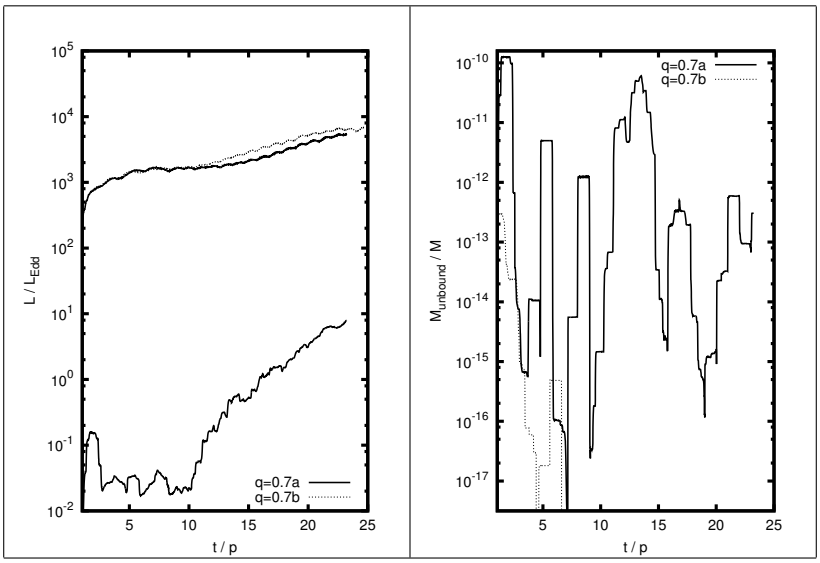

Fig. 7.11.— Accretion luminosity, radiative luminosity, and above zero-binding energy mass fraction for the $q = 0.7a$ (solid curve) and $q = 0.7b$ (dotted curve) runs. *Left:* The top two curves are the orbit averaged accretion luminosities, in units of Eddington luminosity, for the $q = 0.7a$ (solid curve) and $q = 0.7b$ (dotted curve) runs. The bottom curve is the radiative luminosity for the $q = 0.7a$ run. *Right:* The orbit averaged fraction of mass on the grid with a gravitational binding energy above zero for the $q = 0.7a$ (solid curve) and $q = 0.7b$ (dotted curve) runs.

8. $q = 0.4$ Binary Simulations

Here we present the results of three binary simulations. All three begin with the same initial condition of a polytropic binary with mass ratio $q = 0.4$, with the less massive star filling its Roche lobe. In the run referred to as $q = 0.4a$, the radiation feature is enabled. As in §7, we also ran the simulation with the radiation feature disabled, and call it $q = 0.4b$. We also evolve a third run, named $q = 0.4c$. In this run the gas pressure is determined using a polytropic equation of state, much like some of the single polytrope runs in §6.7 and as described in Appendix B. We evolved all three $q = 0.4$ runs on a grid with 180 radial, 256 azimuthal, and 54 vertical interior grid zones. We used reflective symmetry about the equatorial plane, so the effective size in the vertical direction is 108 zones. The grid is larger than that used for the $q = 0.7$ runs. The initial equatorial plane mass density distribution and Roche configuration is shown in Figure 8.1. The logarithmic color scale runs from 10^{-6} to 10^{0} in code units and the contour lines are

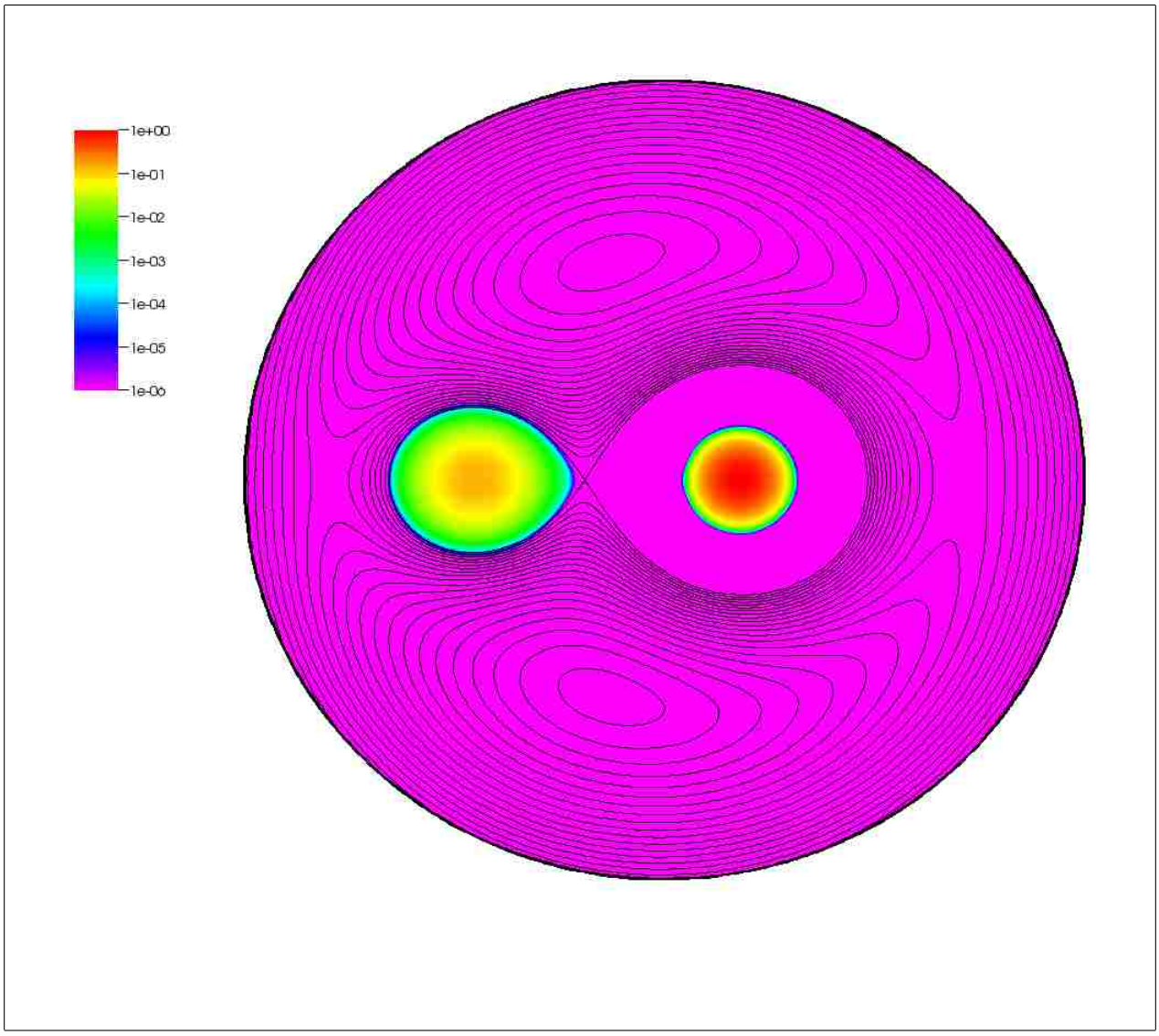

Fig. 8.1.— Equatorial plane mass distribution for the $q = 0.4$ runs at $t = 0$. The logarithmic color scale runs from 10^{-6} to 10^{0} in code units. The black lines are contours of effective potential for $\Phi_{\rm eff} \geq \Phi_{\rm L1}$.

contours of the effective potential. Comparing Figure 7.1 with Figure 8.1, we see that the donor is comparatively larger than the accretor and the donor's center of mass appears further from the coordinate origin, necessitating the use of a larger grid.

We are motivated, in part, to simulate a binary of lower mass ratio because a lower mass ratio binary of polytropes with equal polytropic constants places the surface of the accretor in a deeper effective potential. The accreting matter samples a larger range of the potential and therefore has higher kinetic energy when it strikes the accretor. This produces more internal energy and radiation energy. The $q = 0.4$ mass ratio is also interesting because the question of whether mass transfer is stable for this mass ratio is unsettled. Motl et al. (2007) were able to run a $q = 0.4$ polytropic model for over 40 orbits, and the mass transfer appeared to be stable when the run terminated. D'Souza et al. (2006) obtained similar results for a $q = 0.5$ model. Although earlier SPH simulations suggest DWD systems of this mass ratio fall prey to dynamical, and in some cases, secular instability, and merge within a few orbital periods (Rasio & Shapiro (1995)), recently an SPH model of a $q = 0.5$ DWD took over 60 orbital periods to merge (Dan et al. (2009)). We avoid a lower mass ratio than $q = 0.4$ because, as discussed in §2.2, we do not expect direct impact accretion for a binary of polytropes with equal polytropic constants and $q < 0.35$.

Note that unlike the $q = 0.7$ runs in §7, the center of mass correction, described in Appendix C, is used in the $q = 0.4$ runs.

8.1. Initial Conditions

For the $q = 0.4$ runs we use a different method to obtain the initial conditions. This method allows us to obtain a binary where both polytropes have the same polytropic constant, K. In a manner similar to Rasio & Shapiro (1994), we use the dynamical evolution code itself to generate the initial equilibrium configuration. The method begins by placing two spherical equilibrium polytropes on the grid, each with the same K. The spherical polytropes are obtained by high resolution numerical integration of the Lane-Emden equation (Chandrasekhar (1939)). Their locations on the grid and the initial orbital frequency are determined assuming a point mass Roche geometry. A small frictional force is added to the RHS of the momentum equation. This force is proportional to the fluid velocity, and hence acts to damp any oscillations that develop. The stars are then evolved dynamically, held in place at their initial locations in the manner described in Appendix C. Over a few orbital periods, provided the donor does not overflow its Roche lobe, an equilibrium configuration develops. The polytropes, especially the donor, initially distort rapidly and then slowly settle into a quiet configuration. Once a detached configuration is obtained, the orbital separation and frequencies are adjusted to bring the polytropes closer together and the process is repeated, until the donor is just barely touching the L1 point. Figure 8.1 depicts the $q = 0.4$ initial model we obtained using this method. The initial parameters are given in Table 8.1. As discussed in §7.1, we are free to choose four physical constants. The values used for the $q = 0.4$ runs are shown in Table 8.2. The choice of these constants fixes the ratio of code units to real units shown in Table 8.3. The $q = 0.4$ initial conditions correspond to a physical system with a period of 313 s and components with masses $0.87 M_\odot$ and $0.35 M_\odot$ and respective radii $0.022 R_\odot$ and $0.031 R_\odot$. This model is closer to a real DWD than the $q = 0.7$ model.

Unlike in the $q = 0.7$ run, we evolve the $q = 0.4$ simulations with $\gamma := 1 + \frac{1}{n}$. We are able to avoid convective instability in the $q = 0.a$ run by determining the gas temperature, used in

Table 8.1: $q = 0.4$ Initial Parameters *

	Donor	Accretor
Mass	5.73×10^{-2}	1.43×10^{-1}
Effective Radius	0.823	0.598
Central Mass Density	0.147	0.983
Polytropic Constant (K)	0.131	0.131
Period	66.52	
Separation	2.825	
Grid Spacing	$\frac{\pi}{128} \approx 0.0245$	

*These values are in "code" units.

Table 8.2: $q = 0.4$ Physical Constants in Code Units

Newton's gravitational constant (G)	1.00×10^{0}	$l_{\rm code}^3/m_{\rm code}/t_{\rm code}^2$
speed of light (c)	5.4×10^{1}	$l_{\rm code}^3/t_{\rm code}$
gas constant ($\frac{\mathcal{R}}{\mu}$)	2.68×10^{-1}	$l_{\rm code}^2/t_{\rm code}^2/K_{\rm code}$
Stefan-Boltzmann constant (σ)	4.71×10^{-1}	$m_{\rm code}/t_{\rm code}^3/K_{\rm code}^4$

Table 8.3: $q = 0.4$ Real Units per Code Unit

$l_{\rm code}$	2.61×10^{9} cm
$m_{\rm code}$	1.20×10^{34} g
$t_{\rm code}$	4.70×10^{0} s
$K_{\rm code}$	9.92×10^{8} °K

equation (3-42), with

$$(\gamma - 1)\, e := \frac{\mathcal{R}}{\mu}\rho T_{>\mathrm{ad}} + K\rho^{1+\frac{1}{n}}, \tag{8-1}$$

instead of using equations (4-7) and (4-6). The quantity $T_{>\mathrm{ad}}$ can be thought of as the temperature due to internal energy density above that of the original adiabat. When $T_{>\mathrm{ad}}$ is zero, B_p is also zero and hence there is no cooling. Therefore, physically we expect $T_{>\mathrm{ad}}$ to never drop below zero, but due to numerical error it can drop just below zero. To work around this, we set the gas temperature in equation (3-42) equal to the greater of $T_{>\mathrm{ad}}$ or zero. The limiting behavior of the gas temperature obtained in this manner is more realistic than for the $q = 0.7$ runs. At low enough internal energy densities, the temperature is zero and the gas obeys a polytropic equation of state with $n = \frac{3}{2}$, approximating a non-relativistic cold white dwarf equation of state. At high internal energy densities, the gas temperature asymptotically approaches that obtained from an ideal gas equation of state. Because the K used in equation (8-1) is the same as used in the initial conditions, the evolution begins with the polytropes at zero temperature. Note that using this method to obtain the gas temperature for the $q = 0.7$ runs would be more complicated, as the initial state of each polytrope is determined with different polytropic constants.

We also abandon the use of the approximation to free-free electron scattering outlined in Appendix A. In the $q = 0.7$ runs this component of the opacity turned out to be insignificant. Instead we set all the opacities to the electron scattering cross section, $\kappa_E = \kappa_P = \chi = \sigma_T$.

8.2. Quality of Results

The $q = 0.4$ runs were evolved for approximately 20 orbits each. The relative change in the total angular momentum (left panel), mass (middle panel), and energy (right panel) are plotted in Figure 8.2. The total error in z-angular momentum is an order of magnitude greater than the mass loss throughout the evolution for all $q = 0.4$ runs. Thus it is reasonable to assume the loss in angular momentum is mostly due to error. This relative error is on the order of 10^{-3} per orbit, and therefore angular momentum is not conserved as well as in the $q = 0.7$ runs (see Figure 8.2 and §7.2). We believe this difference is because the $q = 0.4$ DWD binary has a more lopsided mass distribution. As discussed in §5.2, the degree to which the code conserves angular momentum is partially due to how well equation (5-35) is satisfied. At just past the 11^{th} orbit, we decreased the allowed error tolerance for the Poisson solver (that is, the Poisson solver was set to run for more iterations). The bend evident in the curves for the $q = 0.4a$ and $q = 0.4b$ runs (hereafter referred to collectively as the $q = 0.4ab$ runs), coincides with this. Also as discussed §5.2 with regards to equation (5-39), there is an error associated with the grid boundary itself and this error is higher when there is less symmetry in the density distribution. For similar reasons, the $q = 0.4ab$ runs, which conserve energy to approximately one part in 10^{-5} per orbit, do not conserve energy as well as the $q = 0.7$ runs. In the plot of total energy, there is also a bend in the curves for the $q = 0.4ab$ runs at the same time the Poisson solver was adjusted. The larger error in the $q = 0.7c$ run is a result of the polytropic equation of state used in that run. With this equation of state, the model is not expected to conserve total energy. The rate of mass loss through the grid is approximately 10^{-5} per orbit, an order of magnitude higher than for the $q = 0.7$ runs. This is expected due to the higher rate of energy generation from accretion. The $q = 0.4ab$ runs show nearly identical mass loss, indicating the mass loss is not driven by radiation.

For the purposes of producing the figures, we have defined the "common envelope" to be

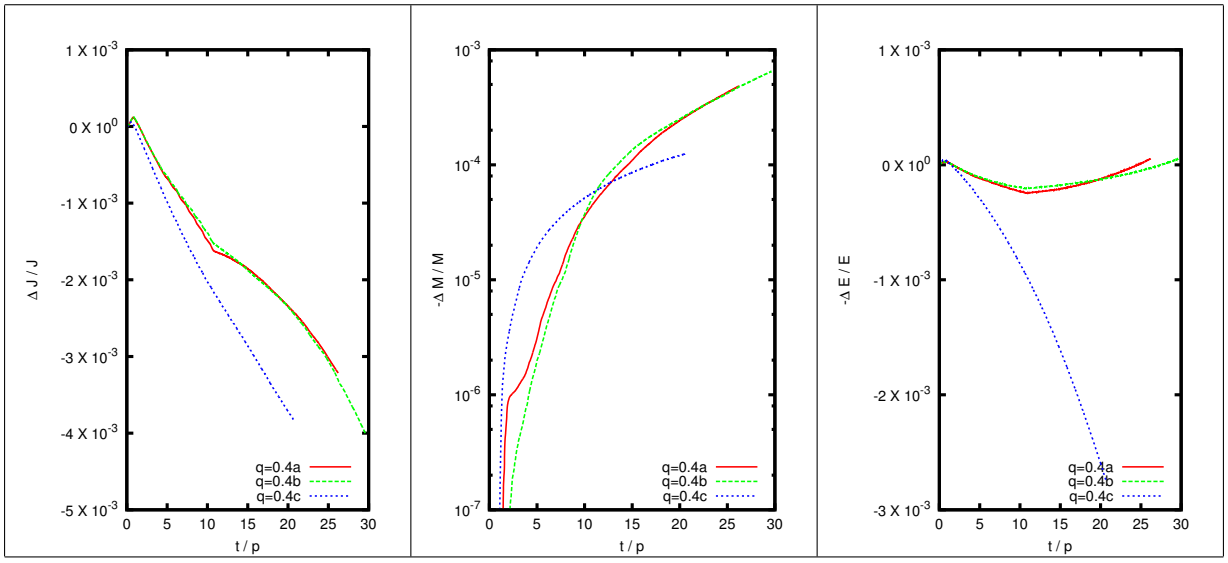

Fig. 8.2.— Total angular momentum, mass, and energy for the $q = 0.4a$ (red curve), $q = 0.4b$ (green curve), and $q = 0.4c$ (blue curve) runs. *Left:* The relative change in the total z-angular momentum on the grid from its initial value. *Middle:* The negative of relative change in the total mass on the grid from its initial value. *Right:* The negative of relative change in the total energy on the grid from its initial value.

any point on the grid for which $\Phi_{\rm eff} + \frac{1}{2}\mathbf{u}^2 < \Phi_{L1}$. If the fluid's gravitational binding energy is below this threshold, a grid cell belongs to either the accretor or donor depending on which of the two exerts more gravitational acceleration at that point. Note that this is not quite the same method described in §7.2. Strictly speaking, the common envelope *should* be defined relative to the L1 potential, as any ballistic particle above this potential can travel between both stars. Due to the wandering center of mass in the $q = 0.7$ simulations, however, it was found that using L1 to define the envelope boundary resulted in extremely high epicyclic variations in many of the Figures shown in §7, so we used L2 instead.

In the left panel of Figure 8.3 we show the radial location of center of mass of the system in units of grid cell widths. Because of the center of mass correction (see Appendix C), the center of mass wanders off at less than 2×10^{-5} grid cell widths per orbit. In the middle and right panels are the maximum densities of the donor and accretor, respectively. The maximum densities in the $q = 0.4c$ run are noticeably different than the $q = 0.4ab$ runs. We attribute this to the simplistic equation of state used in the $q = 0.4c$ run.

8.3. Discussion

Four still frames from the $5^{\rm th}$, $10^{\rm th}$, $15^{\rm th}$, $20^{\rm th}$ orbit for all three runs are shown in Figures 8.4 through 8.6. Figures 8.4 and 8.6 show density with a logarithmic color scale, in code units, running from 10^{-6} to 10^{0}. To highlight the low density regions, the logarithmic density scale in Figure 8.5 runs from 10^{-12} to 10^{-6}. Figures 8.4 and 8.5 depict slices through the equatorial plane, while Figure 8.6 is a slice through the plane perpendicular to the equatorial plane and coincident with the centers of mass of both stars. The $q = 0.4a$ run in Figure 8.5 also contains black and white contour lines. For this plot, we have defined regions of super-Eddington accretion in a

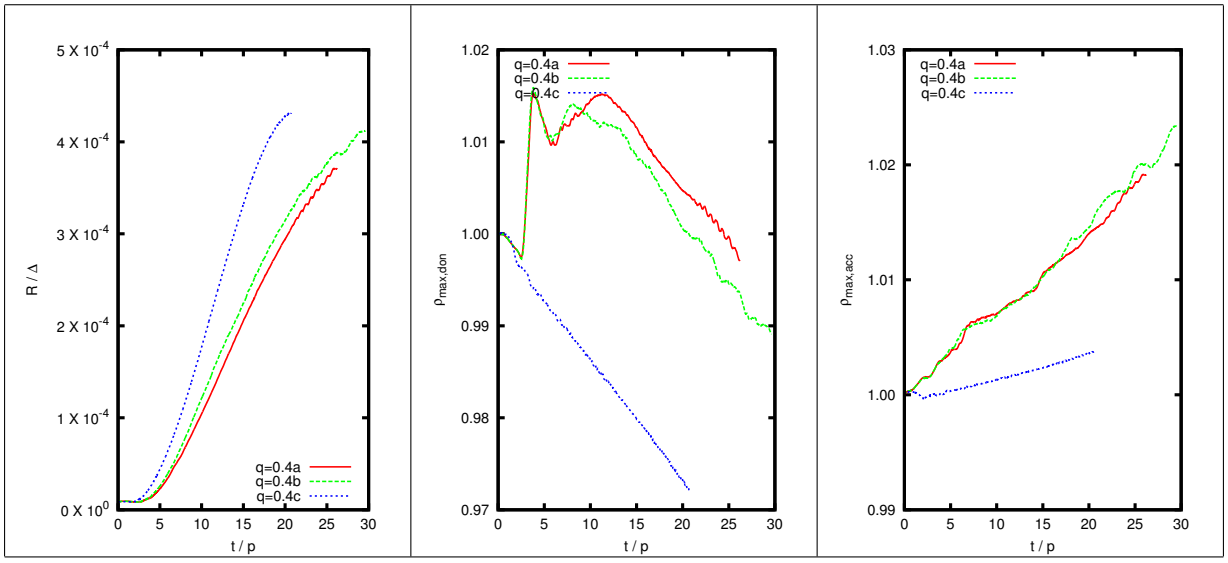

Fig. 8.3.— Center of mass location and maximum densities for the $q = 0.4a$ (red curve), $q = 0.4b$ (green curve), and $q = 0.4c$ (blue curve) runs. *Left:* The orbit averaged radial location of the center of mass of the entire grid. *Middle:* The orbit averaged maximum density of the donor, normalized to its initial value. *Right:* The orbit averaged maximum density of the accretor, normalized to its initial value.

manner identical to that used in Figure 7.6 and described in §7.2. Figure 8.7 is a close-up of the 10^{th} orbit for the $q = 0.4a$ run in Figure 8.5. In these Figures we see that, much like in the $q = 0.7$ runs, an optically thick common envelope fills the grid of the $q = 0.4ab$ runs within a few orbital periods. Since the $q = 0.4c$ run does not incorporate shock heating, the accreted material remains bound to the accretor.

As with the $q = 0.7$ runs in §7, the $q = 0.4$ donors experience RLOF very soon after their evolutions begin. Unlike the $q = 0.7$ runs, the mass transfer rate does not experience a sudden increase after the initial onset of mass transfer. In the top left panel of Figure 8.8 we plot the mass transfer rate. Although it is increasing for the duration of the evolution, after the 5^{th} orbit the rate of increase slows down. The transfer rate for the $q = 0.4c$ run is far lower because of its equation of state. This is because a small amount of heat generation present in the $q = 0.4ab$ runs' outer layers is enough to place the donor into slightly deeper contact. The orbital separation (top right panel) levels off for the $q = 0.4ab$ runs at about the 10^{th} orbit. The $q = 0.4c$ run appears to be heading that direction, just more slowly. Because the $q = 0.4c$ run's mass transfer rate is lower, it tends to take longer for the negative feedbacks responsible for dynamically stable mass transfer to kick in. The effective radius of the donor's Roche lobe (top middle panel) also appears to be leveling off near the end of the runs for $q = 0.4ab$ and again, heading that direction more slowly for $q = 0.4c$. In the bottom panels we see that the spin angular momentum of the donor (left) and accretor (middle) are increasing at the expense of the orbital angular momentum (right) throughout the evolution. The orbital separation can level off, despite the continuous drop in orbital angular momentum, because of the mass transfer.

In the left panel of Figure 8.9 we show the accretion luminosity for all three $q = 0.4$ runs and the radiative luminosity for the $q = 0.4a$ run, in units of Eddington luminosity. As with the $q = 0.7$ runs in §7, the radiative luminosity is only a tiny fraction of the accretion luminosity. The radiation is trapped by the optically thick accretion flow. In the right panel we plot the

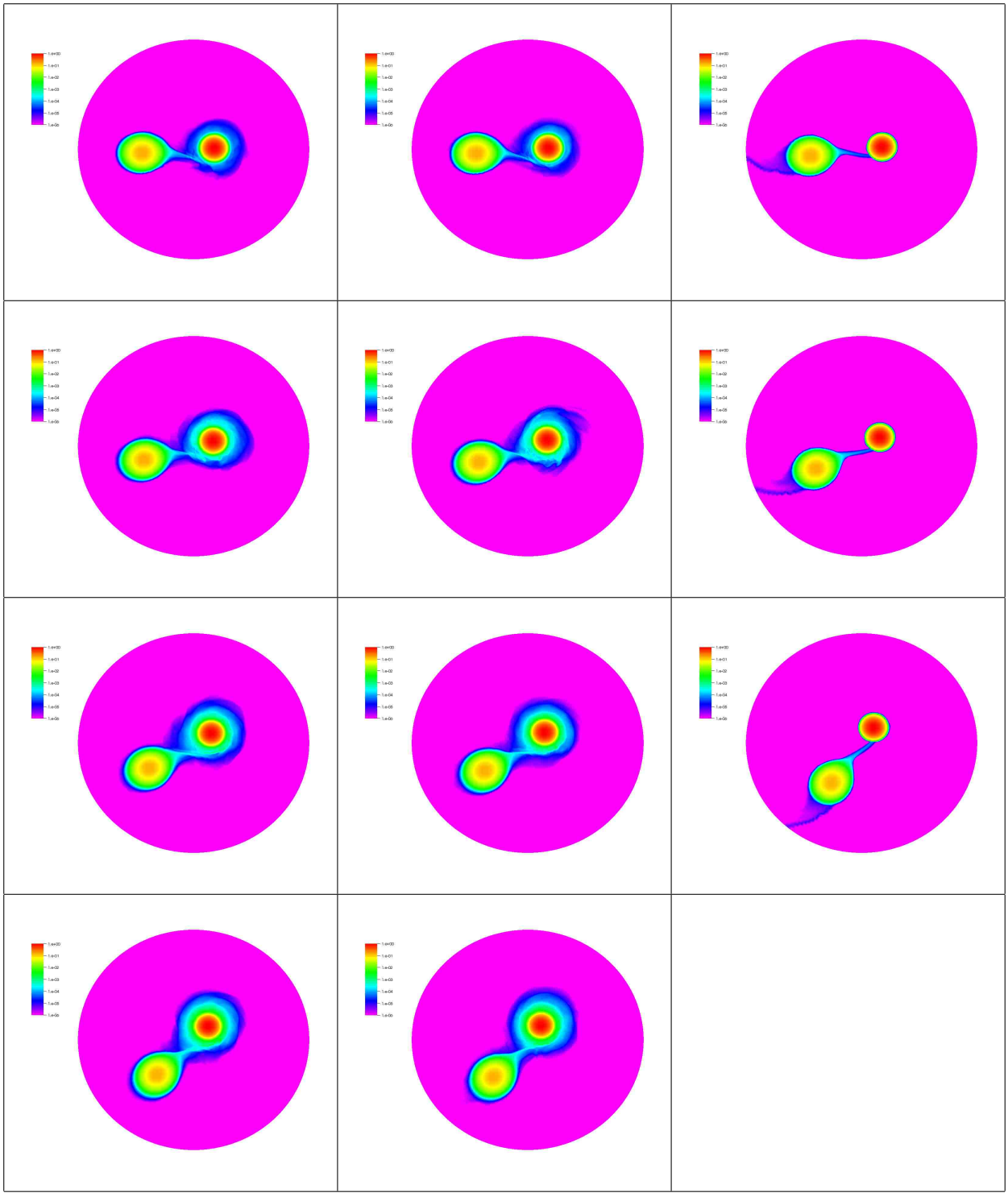

Fig. 8.4.— High density plots of a slice through the equatorial plane for the $q = 0.4$ runs. From left to right we show the $q = 0.4a$, $q = 0.4b$, and $q = 0.4c$ runs at (from top to bottom) $t = 5$, 10, 15, and 20 orbits. The color density scale runs from 10^{-6} to 1 in code units.

fraction of unbound matter on the grid. Much like the $q = 0.7$ runs, this fraction is very tiny, but noticeably larger for the $q = 0.7a$ run.

The most striking difference between the $q = 0.4$ and $q = 0.7$ runs is the formation of a torus

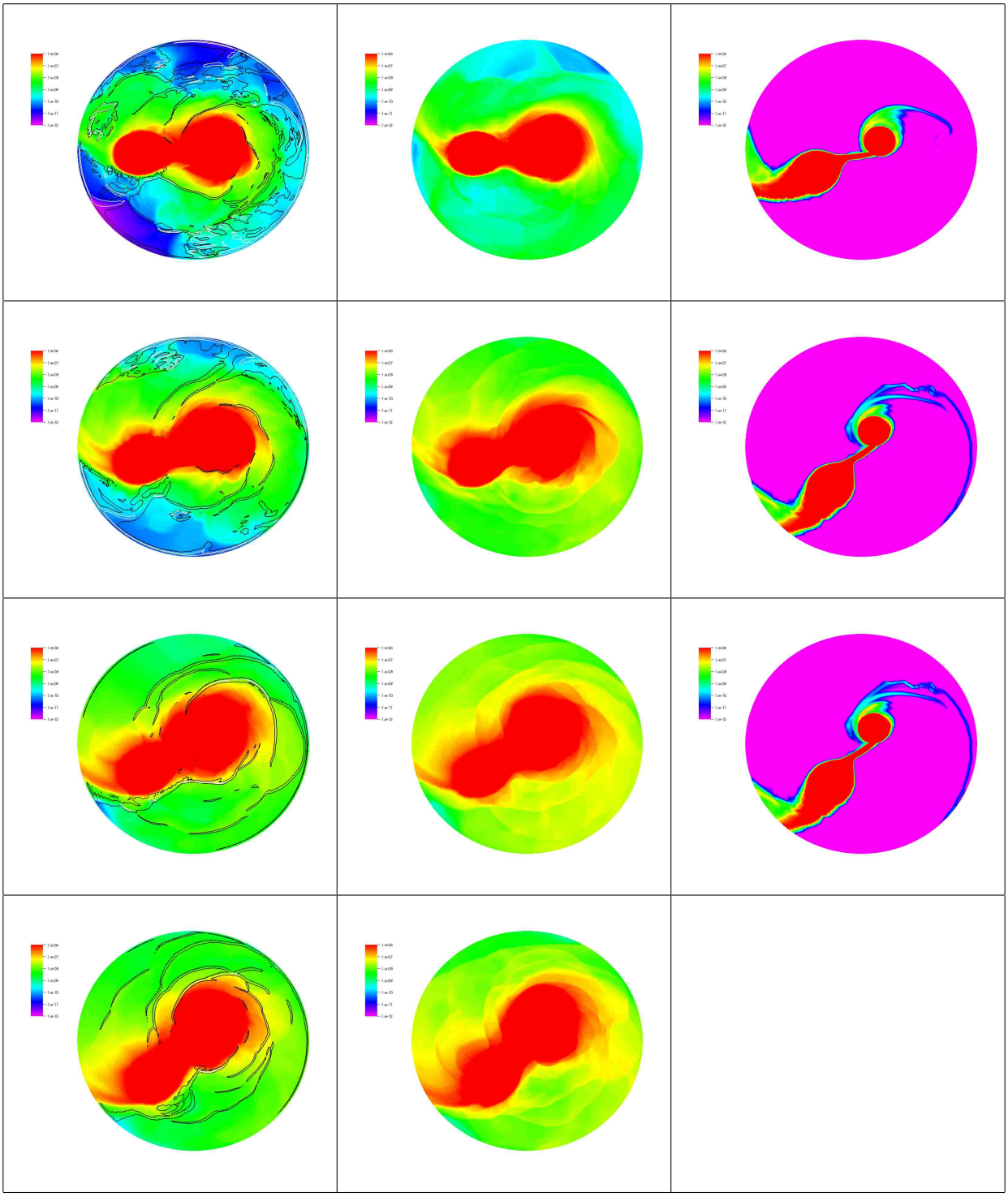

Fig. 8.5.— Low density equatorial slices for $q = 0.4$ runs. We show the $q = 0.4a$, $q = 0.4b$, and $q = 0.4c$ runs (left to right) at $t = 5$, 10, 15, and 20 orbits (top to bottom) . The color density scale runs from 10^{-12} to 10^{-6} in code units. For $q = 0.4a$ we have plotted black and white contours around regions in which the flow is super-Eddington as in Figure 7.6.

like structure around the accretor for the $q = 0.4ab$ runs. A binary of $n = \frac{3}{2}$ polytropes with equal polytropic constants yields direct impact accretion for particles on ballistic trajectories and, in

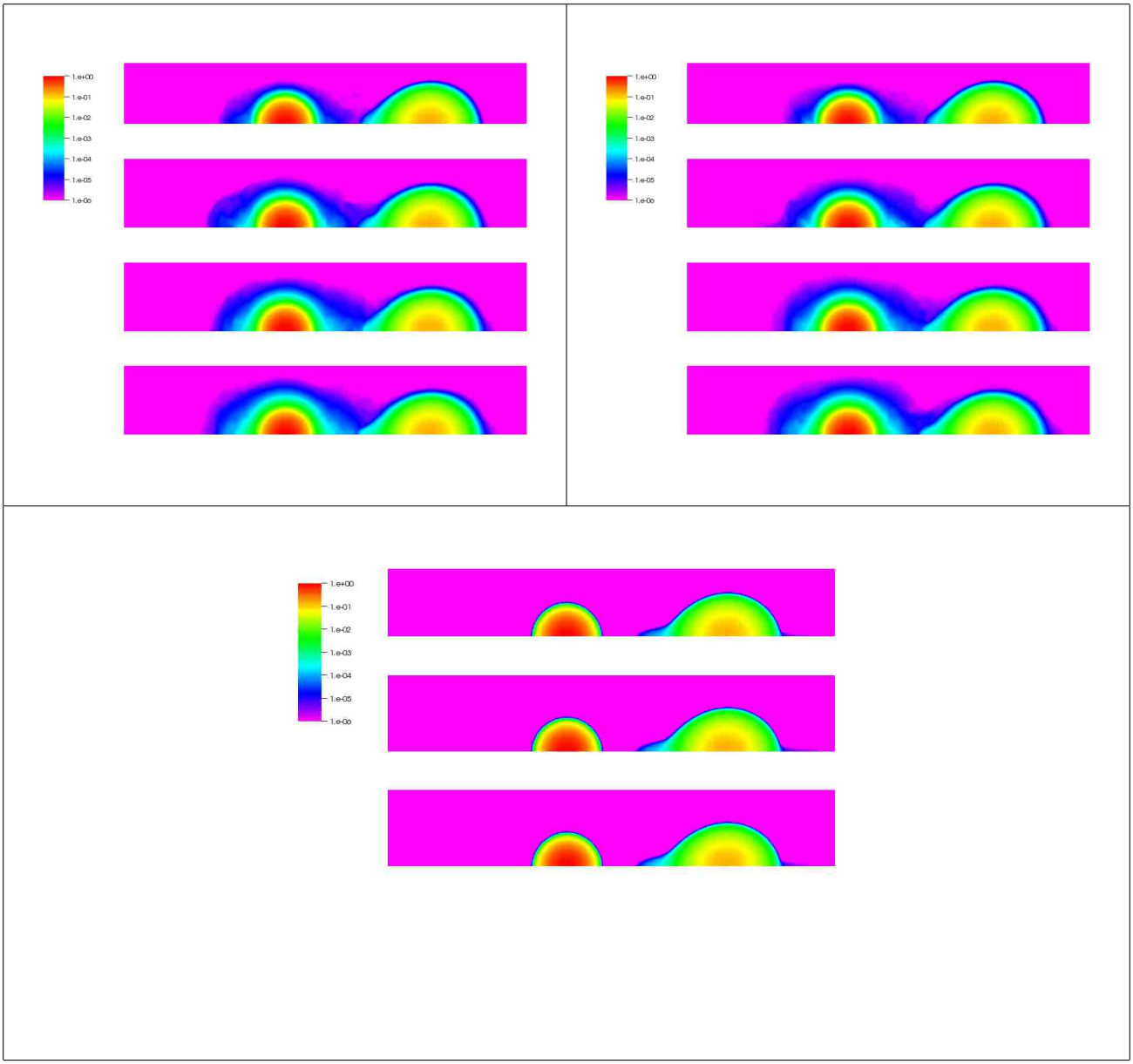

Fig. 8.6.— Density for the $q = 0.4$ runs in the vertical slice perpendicular to the equatorial plane and coinciding with the line running from one star's center of mass to the other's . The top left panel is the $q = 0.4a$ run, the top right panel the $q = 0.4b$ run, and the bottom panel is the $q = 0.4c$ run. From top to bottom, the rows correspond to $t = 5$ orbits, 10 orbits, 15 orbits, and 20 orbits. The color density scale runs from 10^{-6} to 1 in code units. Note that we use symmetry across the equatorial plane in these simulations, so there is only a "top" half of the grid.

fact, all three $q = 0.4$ runs begin mass transfer with direct impact accretion. The $q = 0.4ab$ runs account for shock heating and thus the accreted matter is heated. Rather than mostly settling down onto the accretor as in the $q = 0.4c$ run, it remains in an extended atmosphere, stretching from the surface of the accretor to nearly the edge of the accretor's Roche lobe. This extended atmosphere exerts a pressure on the in-falling material and, just after the 4^{th} orbit of the $q = 0.4ab$ runs, the accretion stream detaches from the surface of the accretor. A torus like

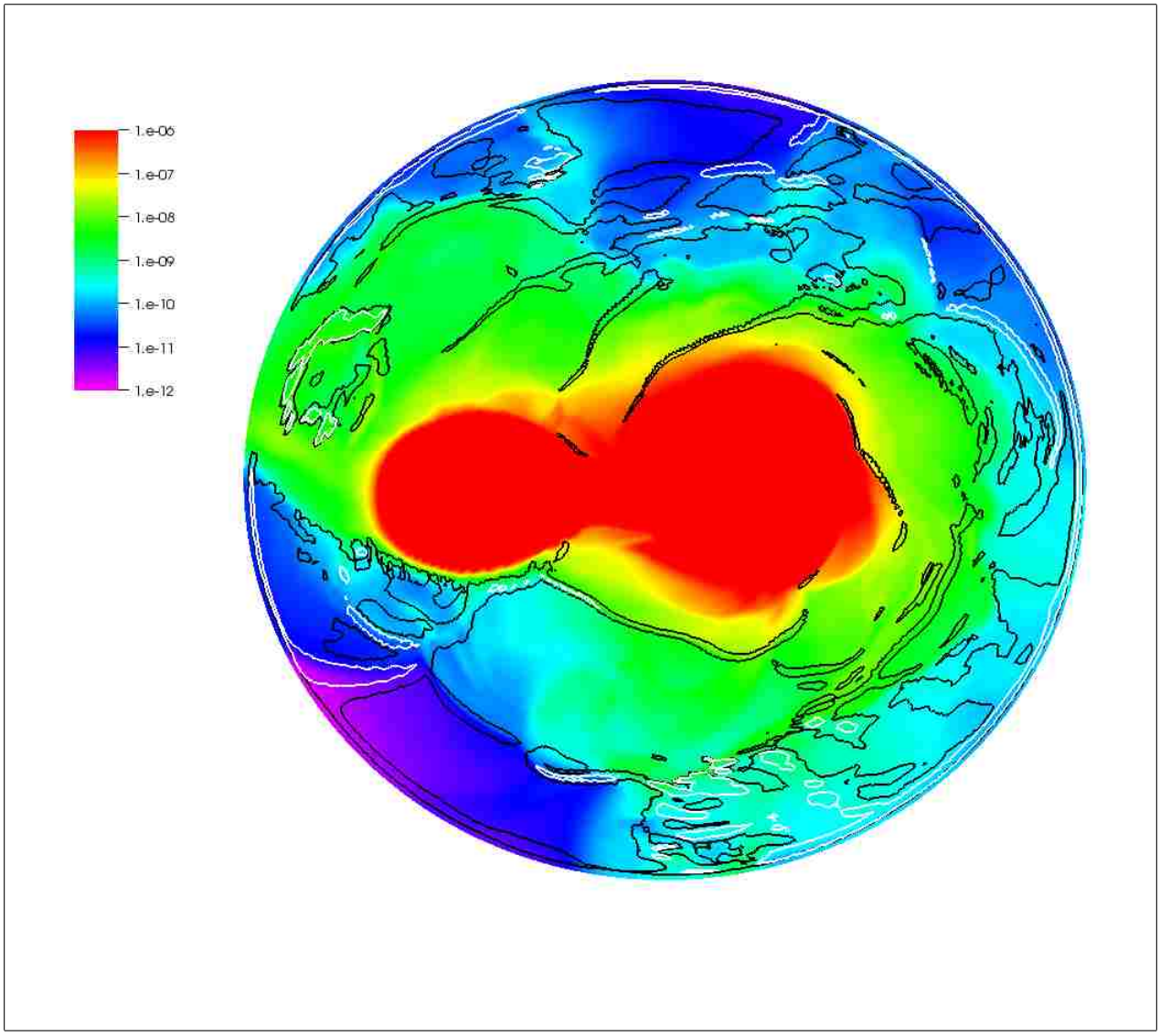

Fig. 8.7.— A close up of the $q = 0.4a$ low density plot at 10 orbits. This figure is seen in the second row from the top of Figure 8.5 in the left column.

structure forms around the equator of the accretor, consisting of mostly donor material. In Figure 8.10 we show the specific entropy profile for the $q = 0.4a$ run in the equatorial plane at four times in the evolution. When the accretion stream impacts the surface directly, it is able to insert its lower entropy material onto the surface of the accretor, underneath any shocked material in an extended atmosphere. Once the accretion stream detaches, it piles its lower entropy material onto the higher entropy shocked torus material. This low entropy material sinks to the surface of the accretor and accumulates there. Looking below the accretor and just to the right, in the upper left panel of Figure 8.11, we see the telltale shape of a Kelvin-Helmholtz instability. There are also knots in the mass density profile of the torus, as seen in the right hand panels of Figure 8.11. This behavior is not unlike what Guillochon et al. (2010) found in a simulation of a similar binary.

For diagnostic purposes we have defined the torus to include any supersonic regions within the accretor's Roche lobe. The accretion torus is not symmetric with respect to the accretor's

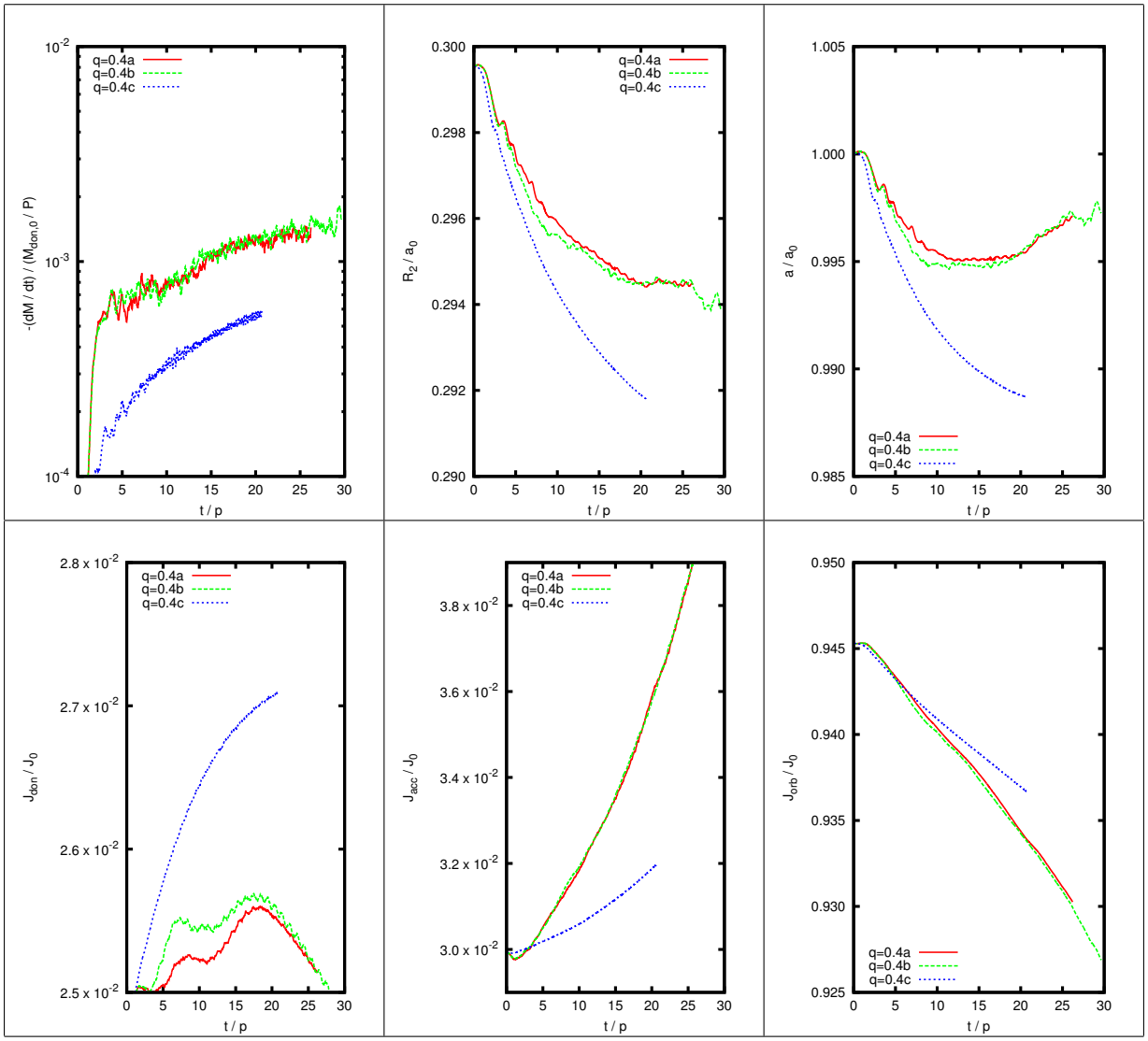

Fig. 8.8.— Mass transfer rate, Roche lobe radius, orbital separation, and angular momenta of the $q = 0.4a$ (red curve), $q = 0.4b$ (green curve), and $q = 0.4c$ (blue curve) runs. *Top Left:* The orbit averaged rate of mass transfer from the donor, normalized to donor masses per orbital period. *Top Middle:* The orbit averaged effective Roche lobe radius of the donor, in units of the initial orbital separation. *Top Right:* The orbit averaged orbital separation normalized to its initial value; *Bottom Left:* The orbit averaged spin angular momentum of the donor, in units of initial total angular momentum. *Bottom Middle:* The orbit averaged spin angular momentum of the accretor, in units of initial total angular momentum. *Bottom Right:* The orbital angular momentum, in units of initial total angular momentum.

center of mass. In the middle and bottom panels of Figure 8.12 we plot the mass of the accretion torus (top panel) and the quantities

$$M_{\rm tor}\,(x_{\rm tor} - x_{\rm acc})\,, \tag{8-2}$$

$$M_{\rm tor}\,(y_{\rm tor} - y_{\rm acc})\,, \tag{8-3}$$

where $M_{\rm tor}$ is the mass of the torus, $(x_{\rm tor}, y_{\rm tor})$ are the center of mass coordinates of the torus,

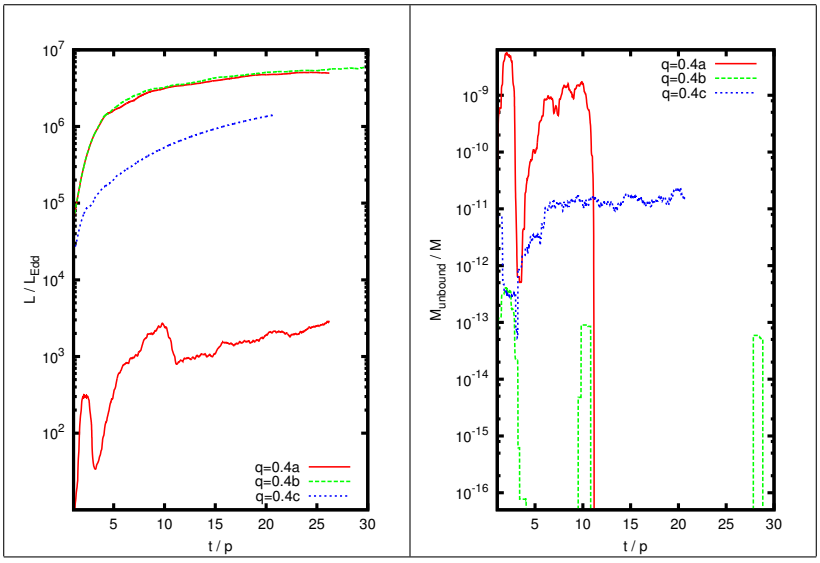

Fig. 8.9.— Accretion luminosity, radiative luminosity, and above zero-binding energy mass fraction for the $q = 0.4a$ (red curve), $q = 0.4b$ (green curve), and $q = 0.4c$ (blue curve) runs. *Left:* The top three curves are the orbit averaged accretion luminosities, in units of Eddington luminosity, for the $q = 0.4a$ (red curve), $q = 0.4b$ (green curve), and $q = 0.4c$ (blue curve) runs. The bottom curve is the radiative luminosity for the $q = 0.4a$ run. *Right:* The orbit averaged fraction of mass on the grid with a gravitational binding energy above zero for the $q = 0.4a$ (red curve), $q = 0.4b$ (green curve), and $q = 0.4c$ (blue curve) runs.

and $x_{\rm acc}$ and $y_{\rm acc}$ are the respective x and y locations of the accretor's center of mass. The torus asymmetry seems to pass through three modes during each of the $q = 0.4ab$ runs. Each run pass through the modes at different times. The first mode is the packet of sinusoidal waves that grows and then diminishes in amplitude, ending at approximately $t = 10$ and $t = 12.5$ orbits for the $q = 0.4a$ and $q = 0.4b$ runs, respectively. The period of lower amplitude irregular oscillations that follows is the second mode. The third mode begins at about $t = 14$ and $t = 17$ orbits for the $q = 0.4a$ and $q = 0.4b$ runs, respectively, when the irregular oscillations grow in amplitude. The $q = 0.4a$ run enters each mode earlier, the amplitude of its oscillations are smaller, and the difference in the modes is not as pronounced. In Figure 8.13, we plot the short time power spectra of the middle panel in Figure 8.12 using a Gaussian window with a variance of one orbit. In the first mode, the center of mass of the torus orbits the accretor with a frequency of approximately 3.8 and 4.4 times the orbital period for the $q = 0.4a$ and $q = 0.4b$ runs, respectively. In the second mode, the center of mass of the torus orbits the accretor with low amplitude and with two frequencies. The lower frequency, at about 3.4 times the orbital frequency, is nearly shared by each run, while the higher frequency, at 4.3 and 4.7 times the orbital frequency for the $q = 0.4a$ and $q = 0.4b$ runs, respectively, is not. The shared frequency in the second mode grows, forming the dominant frequency of the third mode just to the left and right of 3.75 times the orbital period for the $q = 0.4a$ and $q = 0.4b$ runs, respectively. The $q = 0.4b$ run has an additional significant epicyclic frequency at 5 times the orbital period. These torus oscillations appear to be the most significant difference between runs simulated with radiation transport ($q = 0.4a$) and without it ($q = 0.4b$).

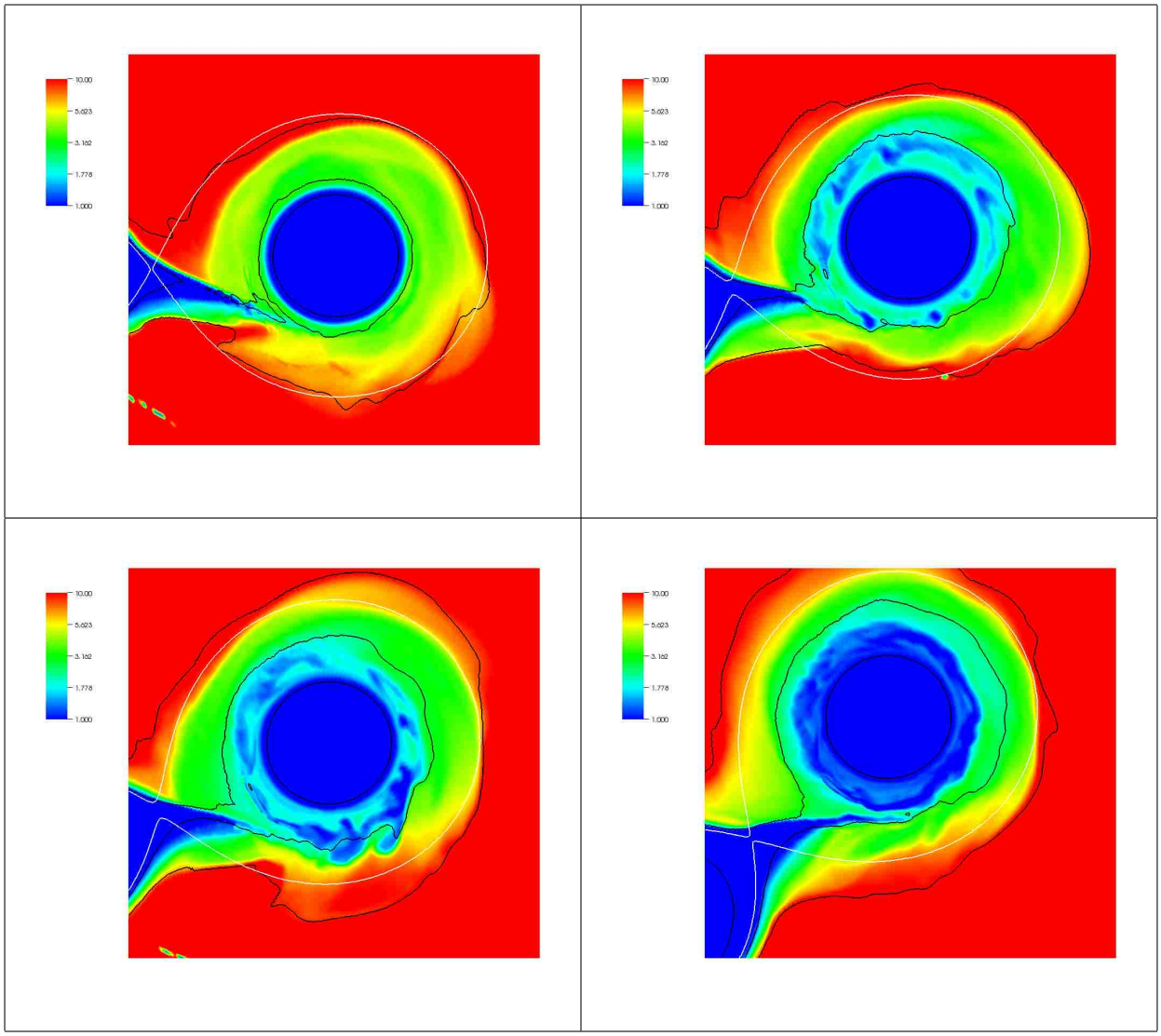

Fig. 8.10.— Specific entropy profile in the equatorial plane for the $q = 0.4a$ runs at four times in evolution. From left to right and top to bottom, we show profiles at $t = 5$, 10, 12, and 19 orbits. The view is a close up of the accretor. The logarithmic entropy scale runs from 1 to 10 in code units, and the logarithmic density scale from 10^{-4} to 10^{-1} in code units. The black contour lines in each plot are contours of density. From the center of the accretor outward, these contour lines correspond to 10^{-2}, 10^{-4}, and 10^{-6}. The single white contour delineates the Roche lobe. Note that the lower left panel in this Figure is the same as the upper left panel in Figure 8.11.

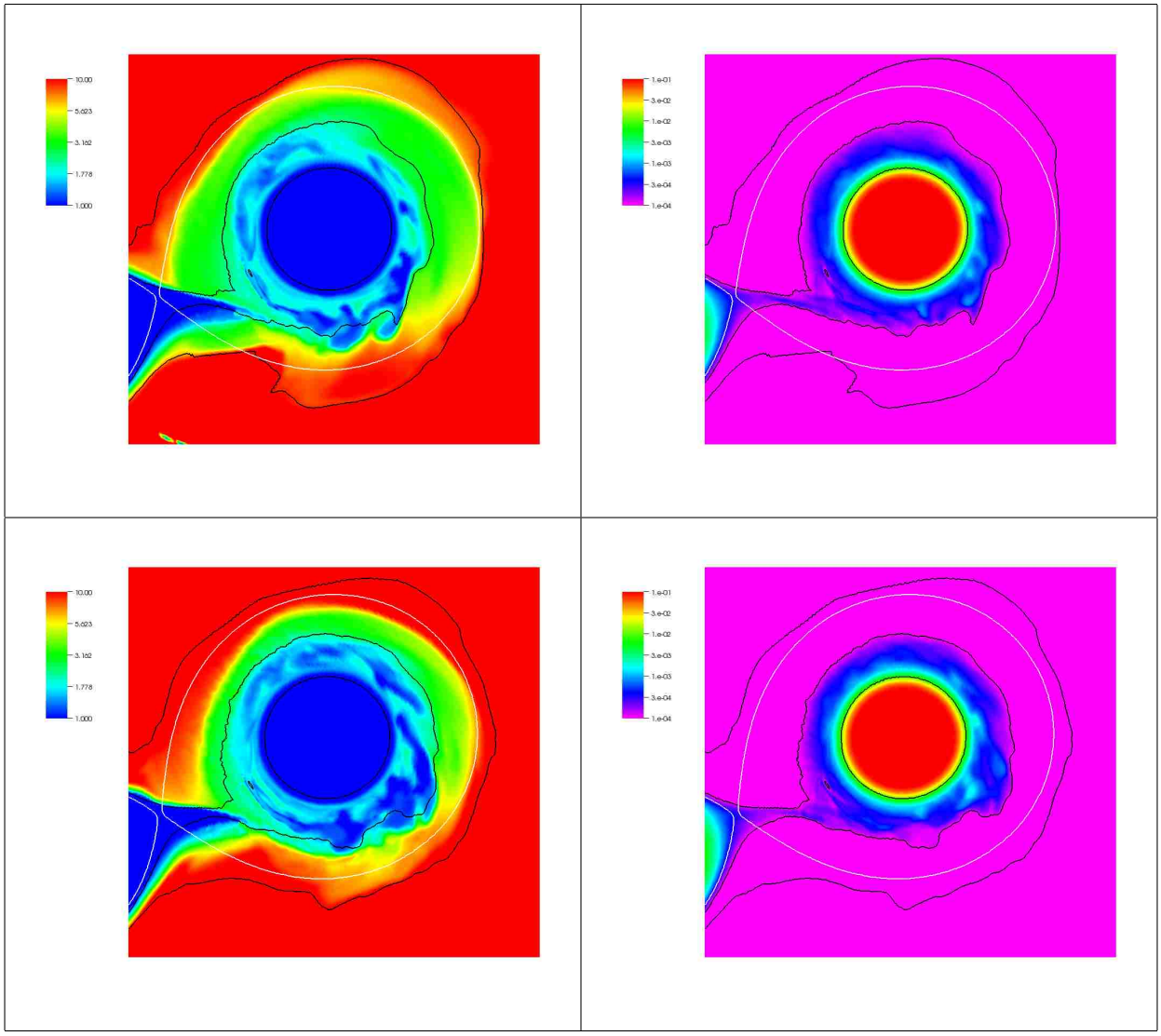

Fig. 8.11.— Specific gas entropy and mass density plots revealing Kelvin-Helmholtz instability in $q = 0.4a$ and $q = 0.4b$ runs. Depicted is an equatorial slice of the specific gas entropy (left column) and mass density (right column) for the $q = 0.4a$ (top row) and $q = 0.4b$ (bottom row) runs at $t = 12$ orbits. The view is a close up of the accretor. The logarithmic entropy scale runs from 1 to 10 in code units, and the logarithmic density scale from 10^{-4} to 10^{-1} in code units. The black contour lines in each plot are contours of density. From the center of the accretor outward, these contour lines correspond to 10^{-2}, 10^{-4}, and 10^{-6} in code units. The single white contour delineates the Roche lobe. Note that the lower left panel in this Figure is the same as the lower left left panel in Figure 8.10

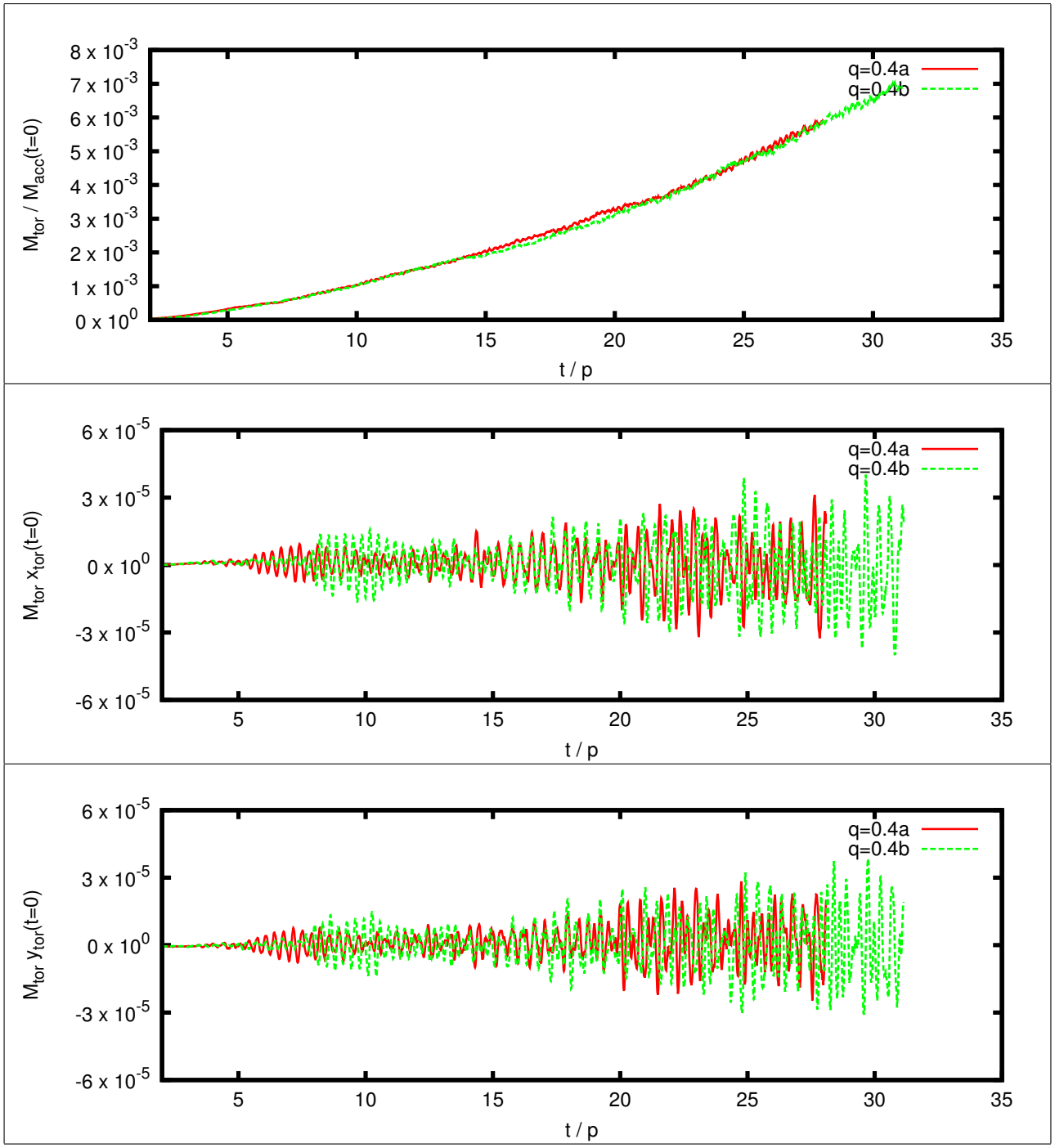

Fig. 8.12.— Accretion tori for $q = 0.4a$ (red curve) and $q = 0.4b$ (green curve) runs. *Top*: The mass of the accretion torus, normalized to the initial mass of the accretor. *Middle:* The quantity $M_{\rm tor}\,(x_{\rm tor} - x_{\rm acc})$. *Bottom* The quantity $M_{\rm tor}\,(y_{\rm tor} - y_{\rm acc})$.

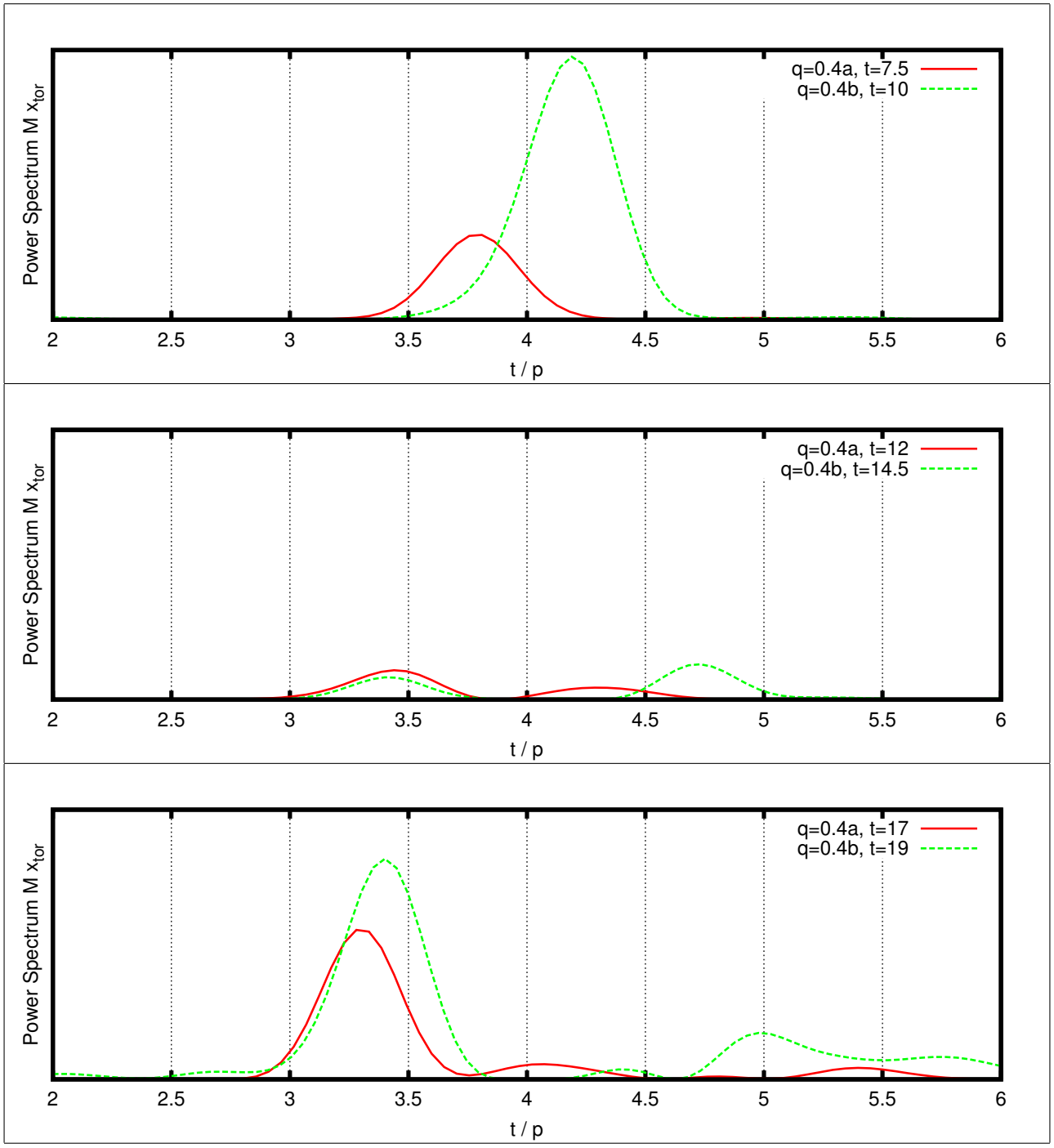

Fig. 8.13.— Accretion tori short time power spectra for $q = 0.4a$ (red curve) and $q = 0.4b$ (green curve) runs. We plot the short time power spectrum of $M_{\rm tor}\,(x_{\rm tor} - x_{\rm acc})$ at (top) 7.5 and 10 orbits, (middle) 12 and 14.5 orbits, (bottom) 17 and 19 orbits for the $q = 0.4a$ and $q = 0.4b$ runs, respectively. The discrete time short term Fourier transform (discrete time STFT) was computed using a Gaussian window with a variance of 1 orbit. The y range is the same scale in each plot. The x axis is the frequency, in the inertial frame, in units of orbital frequency.

9. Conclusions

In this dissertation we have presented a method for the study of super-Eddington accretion flows in interacting DWDs undergoing the initial phase of mass transfer. This method includes several improvements over our previous Eulerian code, among which are: (1) the FLD approximation to the radiative transport equation (§5.3 and §5.4), (2) shock heating by means of a dual energy formalism (§4.1 and §5.1), (3) the incorporation of gravitational and rotational potential terms into the K-T scheme (§5.2), (4) the advection of inertial frame angular momentum instead of lab frame angular momentum, and (5) the use of a higher order reconstruction scheme, eliminating unnecessary numerical viscosity. As discussed in §7.2 and as demonstrated in §6.7, §7, and §8, our new code conserves total energy better than SPH codes and our previous code and conserves total angular momentum as well as SPH codes and better than our previous code.

In §7 we have shown results from two runs modeling a DWD of mass ratio $q = 0.7$ using our new code, one with the radiation feature enabled ($q = 0.7a$), and one with it disabled ($q = 0.7b$). The differences between the two models are minor. The radiation energy in the $q = 0.7a$ run is swept up with the accretion stream, trapped by the optically thick common envelope. Although some mass is lost off the boundary of the computational grid, very little of the mass on the grid ever exceeds zero gravitational binding energy for either run. The common envelope in the $q = 0.7a$ run, able to cool by radiation transport, has a lower specific internal gas energy than the common envelope of the $q = 0.4b$ binary and the rate of mass loss from the donor and accretor into the common envelope is lower for the $q = 0.4a$ run.

We also simulated a DWD of mass ratio $q = 0.4$ (§8). Like the $q = 0.7$ runs, we ran one version with radiation ($q = 0.4a$) and one without it ($q = 0.4b$). Additionally, we evolved a $q = 0.4c$ run that uses a polytropic equation of state in place of a gas energy equation. The evolution of all three runs begins with direct impact onto the accretor, but in the case of the $q = 0.4ab$ runs, the accretion stream detaches from the accretor just after the 4^{th} orbit. The shock heated material in the accretion torus pushes the accretion stream away from the accretor. As discussed in §8.3, the stream instead feeds into the edge of the torus. This torus is not present in the $q = 0.4c$ run because there is no shock heating and the accreted material, remaining cold, is absorbed by the accretor. The torus center of mass does not coincide with the accretor's center of mass. The motion of the torus center of mass goes through three modes of oscillation during the run. The $q = 0.4a$ run goes through these modes quicker and with lower amplitude than the $q = 0.4b$ run.

In both the $q = 0.4$ and $q = 0.7$ runs an optically thick common envelope grows to fill the grid. The geometry of this envelope is crucial. If it is roughly spherical, radiation produced by accretion passes through the entire envelope before leaving the system. If the geometry departs from spherical, radiation can escape more easily. In a disc configuration, for example, radiation produced by accretion along the inner edge of the disc can escape through the upper and lower surfaces of the disc before reaching any of the outer disc. To model the common envelope, the accretion stream, the DWD components, and any accretion structure that forms outside of the accretor, within the limits of present day and near future computers, will require AMR techniques.

The implementation of radiation transport into astrophysical fluid models is nothing new. To our knowledge, however, results of a three-dimensional self-consistent simulation of a DWD at the onset of mass transfer have never been presented. Guillochon et al. (2010) simulated a DWD using an SPH code and used the results to set the boundary conditions for a model of the accretor and accretion stream in the FLASH code. The FLASH code implements FLD radiation

transport, however, the SPH code used to simulate the entire binary did not. The simulations described in §7 and §8 model the entire DWD with radiation hydrodynamics, and we submit that these models are the first of their kind. Although the accuracy of the FLD method is limited outside of the diffusion approximation, it is suitable as a first exploration of super-Eddington accretion in DWDs.

References

Abt, H. A. 1983, Annual Review of Astronomy and Astrophysics, 21, 343

Bazán, G., et al. 2003, in Astronomical Society of the Pacific Conference Series, Vol. 293, 3D Stellar Evolution, ed. S. Turcotte, S. C. Keller, & R. M. Cavallo

Benz, W., Cameron, A. G. W., Press, W. H., & Bowers, R. L. 1990, Astrophysical Journal, 348, 647

Binney, J., & Tremaine, S. 1987, Galactic Dynamics (Princeton, NJ: Princeton University Press)

Bryan, G. L., Norman, M. L., Stone, J. M., Cen, R., & Ostriker, J. P. 1995, Computer Physics Communications, 89, 149

Call, J. M., Tohline, J. E., & Lehner, L. 2010, Classical and Quantum Gravity, 27, 175002

Castor, J. I. 2004, Radiation Hydrodynamics (Cambridge, UK: Cambridge University Press)

Chandrasekhar, S. 1939, An introduction to the study of stellar structure, ed. Chandrasekhar, S. (Chicago, IL: The University of Chicago press)

Clayton, G. C., Geballe, T. R., Herwig, F., Fryer, C., & Asplund, M. 2007, Astrophysical Journal, 662, 1220

Cohl, H. S., & Tohline, J. E. 1999, Astrophysical Journal, 527, 86

Colella, P., & Woodward, P. R. 1984, Journal of Computational Physics, 54, 174

Courant, R., Friedrichs, K., & Lewy, H. 1967, IBM Journal of Research and Development, 11, 215

Dan, M., Rosswog, S., & Brggen, M. 2009, Journal of Physics: Conference Series, 172, 012034

Di Stefano, R. 2010, Astrophysical Journal, 712, 728

D'Souza, M. C. R., Motl, P. M., Tohline, J. E., & Frank, J. 2006, Astrophysical Journal, 643, 381

Ensman, L. 1994, Astrophysical Journal, 424, 275

Even, W., & Tohline, J. E. 2009, Astrophysical Journal Supplement, 184, 248

Even, W. P. 2010, PhD thesis, Louisiana State University and Agricultural & Mechanical College

Farmer, A. J., & Phinney, E. S. 2002, in Bulletin of the American Astronomical Society, Vol. 34, American Astronomical Society Meeting Abstracts, 1225–+

Faulkner, J., Flannery, B. P., & Warner, B. 1972, Astrophysical Journal Letters, 175, L79+

Frank, J., King, A., & Raine, D. J. 2002, Accretion Power in Astrophysics: Third Edition, ed. Frank, J., King, A., & Raine, D. J. (Cambridge, UK: Cambridge University Press)

Friedrichs, K. O. 1954, Communications in Pure and Applied Mathematics, 7, 354

Fryxell, B., et al. 2000, Astrophysical Journal Supplement, 131, 273

Gokhale, V., Peng, X. M., & Frank, J. 2007, Astrophysical Journal, 655, 1010

González, M., Audit, E., & Huynh, P. 2007, Astronomy and Astrophysics, 464, 429

Guerrero, J., García-Berro, E., & Isern, J. 2004, Astronomy and Astrophysics, 413, 257

Guillochon, J., Dan, M., Ramirez-Ruiz, E., & Rosswog, S. 2010, The Astrophysical Journal Letters, 709, L64

Hachisu, I. 1986, Astrophysical Journal Supplement, 62, 461

Han, Z., Podsiadlowski, P., Maxted, P. F. L., Marsh, T. R., & Ivanova, N. 2002, Monthly Notices of the Royal Astronomical Society, 336, 449

Han, Z., & Webbink, R. F. 1999, Astronomy and Astrophysics, 349, L17

Hayes, J. C., Norman, M. L., Fiedler, R. A., Bordner, J. O., Li, P. S., Clark, S. E., ud-Doula, A., & Mac Low, M. 2006, Astrophysical Journal Supplement, 165, 188

Hestenes, M. R. 1952, Research Journal of the National Bureau of Standards, 49, 409

Hils, D., Bender, P. L., & Webbink, R. F. 1990, Astrophysical Journal, 360, 75

Hubeny, I., & Burrows, A. 2007, Astrophysical Journal, 659, 1458

Iben, Jr., I. 1988, Astrophysical Journal, 324, 355

Iben, Jr., I., & Tutukov, A. V. 1984, Astrophysical Journal Supplement, 54, 335

Illenseer, T. F., & Duschl, W. J. 2009, Computer Physics Communications, 180, 2283

Kleinman, S. J., et al. 2004, Astrophysical Journal, 607, 426

Kopal, Z. 1959, Close binary systems (The International Astrophysics Series, London: Chapman and Hall)

Krumholz, M. R., Klein, R. I., McKee, C. F., & Bolstad, J. 2007, Astrophysical Journal, 667, 626

Kurganov, A., & Petrova, G. 2001, Numerische Mathematik, 88, 683

Kurganov, A., & Tadmor, E. 2000, Journal of Computational Physics, 160, 241

Lax, P. D. 1954, Communications in Pure and Applied Mathematics, 7, 159

Levermore, C. D., & Pomraning, G. C. 1981, Astrophysical Journal, 248, 321

Liebling, S. L. 2002, Physical Review D, 66, 041703

Livio, M., & Riess, A. G. 2003, Astrophysical Journal Letters, 594, L93

Livne, E., Burrows, A., Walder, R., Lichtenstadt, I., & Thompson, T. A. 2004, Astrophysical Journal, 609, 277

Marcello, D. C., & Tohline, J. E. 2011, submitted for publication in The Astrophysical Journal Supplement

Marsh, T. R., Dhillon, V. S., & Duck, S. R. 1995, Monthly Notices of the Royal Astronomical Society, 275, 828

Marsh, T. R., Nelemans, G., & Steeghs, D. 2004, Monthly Notices of the Royal Astronomical Society, 350, 113

Marshak, R. E. 1958, Physics of Fluids, 1, 24

McCook, G. P., & Sion, E. M. 1999, Astrophysical Journal Supplement, 121, 1

Mihalas, D., & Mihalas, B. W. 1984, Foundations of Radiation Hydrodynamics (New York, Oxford University Press)

Mochkovitch, R., & Livio, M. 1990, Astronomy and Astrophysics, 236, 378

Morales-Rueda, L., Marsh, T. R., Maxted, P. F. L., Nelemans, G., Karl, C., Napiwotzki, R., & Moran, C. K. J. 2005, Monthly Notices of the Royal Astronomical Society, 359, 648

Motl, P. M. 2001, PhD thesis, Louisiana State University and Agricultural & Mechanical College

Motl, P. M., Frank, J., Tohline, J. E., & DSouza, M. C. R. 2007, Astrophysical Journal, 670, 1314

Motl, P. M., Tohline, J. E., & Frank, J. 2002, Astrophysical Journal Supplement, 138, 121

Mullally, F., Badenes, C., Thompson, S. E., & Lupton, R. 2009, Astrophysical Journal Letters, 707, L51

Napiwotzki, R. 2009, Journal of Physics Conference Series, 172, 012004

Nayakshin, S., Cha, S.-H., & Hobbs, A. 2009, Monthly Notices of the Royal Astronomical Society, 397, 1314

Nelemans, G., Portegies Zwart, S. F., Verbunt, F., & Yungelson, L. R. 2001a, Astronomy and Astrophysics, 368, 939

Nelemans, G., Yungelson, L. R., & Portegies Zwart, S. F. 2001b, Astronomy and Astrophysics, 375, 890

Nelemans, G., Yungelson, L. R., Portegies Zwart, S. F., & Verbunt, F. 2001c, Astronomy and Astrophysics, 365, 491

Nelemans, G., et al. 2005, Astronomy and Astrophysics, 440, 1087

Nessyahu, H., & Tadmor, E. 1990, Journal of Computational Physics, 87, 408

New, K. C. B., & Tohline, J. E. 1997, Astrophysical Journal, 490, 311

Nomoto, K., & Iben, Jr., I. 1985, Astrophysical Journal, 297, 531

Ott, C. D., Burrows, A., Dessart, L., & Livne, E. 2008, Astrophysical Journal, 685, 1069

Paczyński, B. 1967, Acta Astronomica, 17, 287

Padmanabhan, P. 2000, Theoretical Astrophysics Volume I: Astrophysical Processes (Cambridge, MA: Cambridge University Press)

Parsons, S. G., Marsh, T. R., Gänsicke, B. T., Drake, A. J., & Koester, D. 2011, The Astrophysical Journal Letters, 735, L30

Poelarends, A. J. T., Herwig, F., Langer, N., & Heger, A. 2008, Astrophysical Journal, 675, 614

Pomraning, G. C. 1979, Journal of Quantitative Spectroscopy and Radiative Transfer, 21, 249

Postnov, K. A., & Yungelson, L. R. 2006, Living Reviews in Relativity, 9, 6

Potter, A. T. 2009, Certificate of Postgraduate Study, Cambridge University (Great Britain)

Rasio, F. A., & Shapiro, S. L. 1994, Astrophysical Journal, 432, 242

—. 1995, Astrophysical Journal, 438, 887

Saio, H., & Jeffery, C. S. 2000, Monthly Notices of the Royal Astronomical Society, 313, 671

Saio, H., & Nomoto, K. 1985, Astronomy and Astrophysics, 150, L21

Segretain, L., Chabrier, G., & Mochkovitch, R. 1997, Astrophysical Journal, 481, 355

Shu, C., & Osher, S. 1988, Journal of Computational Physics, 77, 439

Shu, F. H. 1992, Physics of Astrophysics, Vol. II (University Science Books)

Sod, G. A. 1978, Journal of Computational Physics, 27, 1

Stone, J. M., & Norman, M. L. 1992, Astrophysical Journal Supplement, 80, 753

Su, B., & Olson, G. L. 1996, Journal of Quantitative Spectroscopy and Radiative Transfer, 56, 337

Tasker, E. J., Brunino, R., Mitchell, N. L., Michielsen, D., Hopton, S., Pearce, F. R., Bryan, G. L., & Theuns, T. 2008, Monthly Notices of the Royal Astronomical Society, 390, 1267

Tohline, J. E. 2002, Annual Review of Astronomy and Astrophysics, 40, 349

Tokovinin, A. A. 1997, A&AS, 124, 75

van Leer, B. 1977, Journal of Computational Physics, 23, 263

Webbink, R. F. 1984, Astrophysical Journal, 277, 355

Wolf, S., Henning, T., & Stecklum, B. 1999, Astronomy and Astrophysics, 349, 839

Yoon, S. C., Podsiadlowski, P., & Rosswog, S. 2007, Monthly Notices of the Royal Astronomical Society, 380, 933

Appendix A: Opacities

The three opacities in our equation set, χ, κ_P, and κ_E, represent the frequency integrated opacity weighted by the frequency dependent radiative flux, $\mathbf{F}_\nu$, the frequency dependent Planck function, B_ν, and the frequency dependent radiative energy density, $E_{R,\nu}$, respectively. Their definitions are given by equations (3-15), (3-14), and (3-43), respectively. Physically, κ_P and κ_E should contain absorption terms only, while χ includes absorption as well as scattering. If the opacity is frequency dependent we have to make assumptions about the spectrum in order to integrate the opacity over frequency. In the diffusion limit we may assume a blackbody spectrum. When the radiation is free-streaming, however, this assumption does not generally hold. Additionally, when Thompson scattering and free-free absorption terms are both present in χ, we cannot obtain an analytic expression even in the diffusion limit. Due to these limitations, we adopt a simplistic expression for the opacities. For the $q = 0.7a$ run, we have set

$$\chi := \sigma_T \rho + a_{\text{ff,s}} \rho^2 T^{-3.5}, \tag{9-1}$$

and

$$\kappa_E := \kappa_P := a_{\text{ff,a}} \rho^2 T^{-3.5}, \tag{9-2}$$

where

$$\sigma_T := 8.4 \times 10^{12} \left(l_{\text{code}}^2 / m_{\text{code}} \right), \tag{9-3}$$

$$a_{\text{ff,s}} := 2.12 \times 10^{11} \left(l_{\text{code}}^5 K_{\text{code}}^{3.5} / m_{\text{code}}^2 \right), \tag{9-4}$$

and

$$a_{\text{ff,s}} := 6.50 \times 10^{12} \left(l_{\text{code}}^5 K_{\text{code}}^{3.5} / m_{\text{code}}^2 \right). \tag{9-5}$$

In practice, for the $q = 0.7a$ run, we find that the first term of equation (9-1) (the scattering term) is generally several orders of magnitude higher than the second term. We therefore adopt a simpler relation for the $q = 0.4$ runs, $\kappa_E = \kappa_P = \chi = \sigma_T$.

Appendix B: Three Different Gas Energy Schemes

We refer to the gas energy scheme of equation (5-37) as the E* scheme. An alternative scheme for the total gas energy is

$$\begin{aligned}\frac{d}{dt}E_{G,jkl} + \mathcal{D}\left\{\left(\mathcal{E}_{\mathrm{G}} + p\right)\mathbf{u}\right\}_{jkl} &= \mathcal{V}\left\{\mathcal{E}_{\mathrm{G}}\right\}_{jkl} - \frac{s_{R,jkl}}{2\Delta}\left(\Phi_{\mathrm{eff},j+1kl} - \Phi_{\mathrm{eff},j-1kl}\right) \\ &- \frac{l_{z,jkl} - \rho_{jkl}R_j^2\Omega}{2R_j\Delta}\left(\Phi_{\mathrm{eff},jk+1l} - \Phi_{\mathrm{eff},jk-1l}\right) - \frac{s_{z,jkl}}{2\Delta}\left(\Phi_{\mathrm{eff},jkl+1} - \Phi_{\mathrm{eff},jkl-1}\right). \quad (9\text{-}6)\end{aligned}$$

Equation (9-6) is obtained by applying equation (5-24) to the total gas energy and adding first-order discrete derivatives to the RHS to account for the gravitational term. As shown above in §6.7, application of equation (9-6) to stellar models results in an ever increasing total system energy. Over many dynamical timescales, the polytrope will dissipate.

Another way to handle the gas energy is to not evolve E_G or τ at all. Instead we obtain the pressure using the polytropic relation of equation (2-6) and setting $\gamma := 1 + \frac{1}{n}$. As shown in §6.7, the resulting model does *not* appear to lose energy indefinitely.

Appendix C: Center of Mass Correction

The center of mass correction applied to some of the simulations in §6.7 is formulated according to

$$\mathbf{a}_{\rm COM} := -\omega^2 \left(\mathbf{X}_{\rm COM} - \mathbf{X}_{0,\rm COM}\right) - 2\omega \frac{d}{dt}\mathbf{X}_{\rm COM}, \tag{9-7}$$

where $\mathbf{a}_{\rm COM}$ is the spatially constant acceleration used to correct for center of mass motion, $\mathbf{X}_{\rm COM}$ is the current center of mass of the system, $\mathbf{X}_{0,\rm COM}$ is the center of mass at $t = 0$, and ω is a suitably chosen constant. In the polytrope simulations discussed in §6.7, $\omega := 1$, which is close to the inverse of the dynamical timescale. Equation (9-7) is the equation for a critically damped harmonic oscillator. We chose this as our correction because we would like to counteract any displacements from the original center of mass without overshooting. At each time step, the center of mass of the system is computed. The velocity of the center of mass $\frac{d}{dt}\mathbf{X}_{\rm COM}$ is determined using $\mathbf{X}_{\rm COM}$ from the current and previous time step. The term

$$\rho_{jkl}\left(a_{{\rm COM},x}\cos\phi_k - a_{{\rm COM},y}\sin\phi_k\right) \tag{9-8}$$

is added to the RHS of radial momentum equation (5-51). The term

$$\rho_{jkl} R_j \left(a_{{\rm COM},x}\sin\phi_k + a_{{\rm COM},y}\cos\phi_k\right) \tag{9-9}$$

is added to the RHS of the angular momentum equation (5-52). The total gas energy equation (5-54) is modified by adding

$$\rho_{jkl}\mathbf{u}_{jkl} \cdot \mathbf{a}_{\rm COM} \tag{9-10}$$

to its RHS.

Note we do not use this correction in the $q = 0.7$ runs (§7). It is used, however, for the $q = 0.4$ runs (§8).

Appendix D: Letter of Permission

Figure D.1 shows the copyright agreement from the American Astronomical Society (AAS). The agreement allows the author to reproduce parts of their article wherever they wish. All or substantial parts of §4 and its subsections, §5 and its subsections, §6, §6.2, §6.3, §6.6, §6.7, and §7 and its subsections are reproduced from Marcello & Tohline (2011).

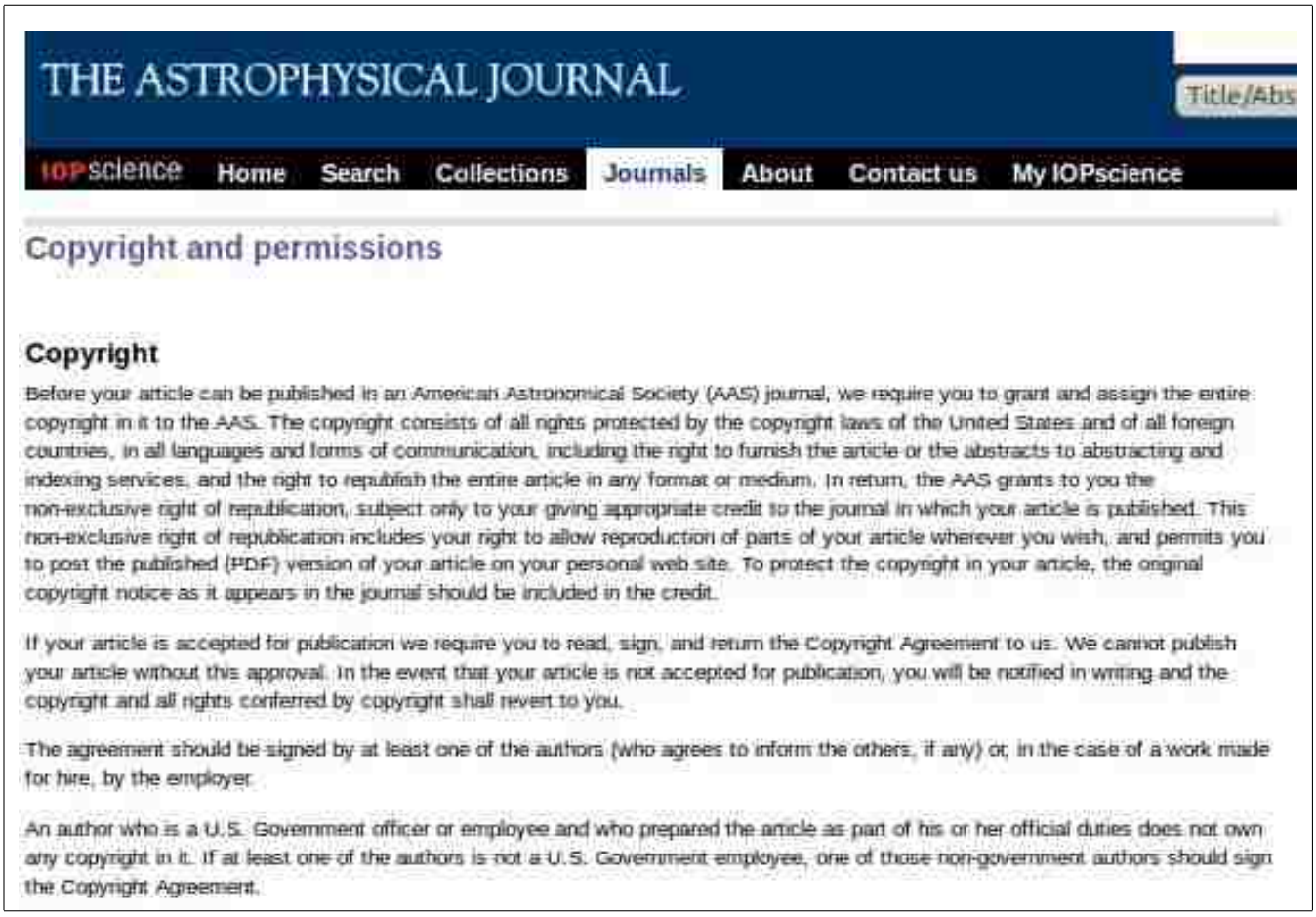

Fig. D.1.— The copyright agreement pertaining to the use of parts of Marcello & Tohline (2011). This agreement may be found at 'http://iopscience.iop.org/0004-637X/page/Copyright and permissions'

Vita

Dominic Carlo Marcello was born in Baton Rouge, Louisiana, to Gail Wood and Victor Marcello, in the year 1977. He completed his Bachelor of Science in physics at Louisiana State University and Agricultural and Mechanical College in May of 2000. He was an observer during 2003 and 2004 at the United States Naval Observatory Flagstaff Station, Flagstaff, Arizona. He lives with his wife Sarah in New Orleans, Louisiana.